Non-perturbative determination of Karsch Coefficients in 2 Colour QCD

Seamus Cotter
B.Sc.

NUI MAYNOOTH
Ollscoil na hÉireann Má Nuad

Thesis presented for the degree of

Doctor of Philosophy

to the

National University of Ireland Maynooth
Department of Mathematical Physics

October 2015

Department Head

Professor Daniel M. Heffernan

Research advisor

Dr. Jon Ivar Skullerud

Contents

Summary

Lattice QCD can be used to study the QCD phase diagram at finite temperature and zero density. Non-zero density is implemented on the lattice using the chemical potential however this gives a possibility of a complex probability which means the statistical machinery normally used breaks down. Switching the gauge group from three colour to two colour avoids this problem.

Simulating two colour QCD allows for investigation into the thermodynamic phase transitions of a theory which is similar to three colour QCD. Confinement and asymptotic freedom are observed, however the definitions for hadrons differ. To study the thermodynamics we use the derivative method which requires the determination of the Karsch coefficients. Previous studies determined these coefficients perturbatively however this led to negative values for pressure. Non-perturbative studies have proved difficult due to the computational cost and accuracy required.

We attempt to determine these coefficients non-perturbatively and review possible improvements in setup and calculation. We finish with thermodynamic results for the pressure, energy density and trace anomaly.

1 Lattice QCD

1.1 Overview

In this chapter I will first give a general overview to quantum field theory and quantum chromodynamics (QCD). After putting the theory in context I will then discuss the structures necessary to define lattice QCD, and some of the alternative formulations and the various possible improvements. I will finish the chapter with a brief discussion on the numerical techniques used and the consequences or restrictions they have on calculations.

First we start with a few historical highlights leading up to development of the standard model:

1800s This century sees work on thermodynamical problems lead to a general framework of macroscopic and microscopic quantities. Towards the end of the century, structures from statistical mechanics such as the Maxwell-Boltzmann distribution are used to explain thermodynamics.

1805 Young carries out his double slit experiment which demonstrates light's wave behaviour.

1860s Maxwell's laws of electromagnetism unify electricity and magnetism. It is later shown to be one of the first theories with what is now known as a gauge symmetry.

1890s An example of electromagnetic radiation, X-rays, and the first elementary particle, the electron, are discovered.

1900 Planck states the quantum hypothesis which states that radiation can be seen in terms of discrete packets or quanta.

1905 Einstein develops special relativity unifying space and time, and explains the photoelectric effect of light emission and absorption in terms of quanta.

1911 Rutherford's gold foil experiment leads to a rethink of the atomic model.

1915 General relativity is defined by Einstein which combines gravity and special relativity.

1920s Development of quantum mechanics including the definition of Schrödinger's equation, Pauli's exclusion principle and Heisenberg's uncertainty principle. Dirac unifies special relativity and quantum mechanics which leads to the prediction of antiparticles.

1930s A quantum field theory for weak interactions is defined by Fermi.

1940s Tomonaga, Schwinger and Feynman independently work on what is later known as Renormalisation. QED is born and the path integral method is formulated.

1950s Yang-Mills theory generalises the abelian gauge theory of QED to a more rich non-abelian gauge theory which allows for a description of strong interactions.

1960s A quark model is formulated which would describe hadron physics. Gell-Mann, Zweig, Bjorken and Feynman's work lead to experiments that show that neutrons and protons are made of quarks.

1962 A mechanism which causes the spontaneous symmetry breaking of the gauge symmetry is proposed by Englert and Brout, and slightly later by Higgs, which explains the non-zero masses of gauge bosons.

1967 Salam and Weinberg define the electroweak force which unifies the electromagnetic and weak interactions. Building on work by Glashow they predict the W and Z bosons.

1968 Deep inelastic scattering experiments at SLAC lead to parton model.

1970s The early part of the decade saw the definition of asymptotic freedom separately by t'Hooft, David Politzer, David Gross and Franz Wilzek.

1973 The Standard Model is completed[1].

1974 The charm quark is discovered at Brookhaven and SLAC. Confinement described analytically, by Kenneth Wilson using Lattice QCD [1].

1977 The bottom quark is discovered at Fermilab. Confinement described numerically on the lattice by Michael Creutz [2].

1983 The predicted W and Z bosons are discovered.

1995 The top quark is discovered at Fermilab.

2012 The Higgs boson is discovered at CERN.

1.2 Framework

Feynman's path integral method gave a probabilistic definition of the path travelled by a particle in terms of the the Lagrangian density $\mathcal{L}$. The action is defined as

[1] Minor adjustments are later made to explain experimental results such as a small mass for the neutrino which was originally thought to be massless

$S = \int dtL$ or for a field operator, $S = \int dtd^3x\mathcal{L}$. From this, the principle of least action gives $\delta S = 0$ for the classical solution. The path integral method allows us to write all expectation values in terms of the exponential of the action. In a simple quantum mechanical example, the transition amplitude of the system which defines the evolution of the system can be written in natural units, ie $\hbar = c = 1$, as an integral over all possible paths giving:

$$\left\langle x' \left| e^{-iHt} \right| x \right\rangle = \int [\mathcal{D}x]\, e^{-iS}, \tag{1.1}$$

This can be generalised to a description of more complicated objects such as scalar and vector fields. Quantum field theories are generic quantum mechanical frameworks in which particles are seen as excitations of the underlying fields. Combining this with special relativity gave the first self contained theory in quantum electrodynamics (QED) which describes how light and matter interact and can be thought of as a modern concise description of Maxwell's electromagnetism. In the gauge field framework forces between particles are said to be mediated by a boson associated with that force. In the case of QED the force carrier is the photon, and matter can absorb and emit photons. The QED Lagrangian is given by:

$$\mathcal{L}_{\text{QED}} = -\frac{1}{4}F_{\mu\nu}F^{\mu\nu} + \bar{\psi}\left(i\gamma^\mu D_\mu - m\right)\psi, \tag{1.2}$$

where $F_{\mu\nu} = \partial_\mu A_\nu - \partial_\nu A_\mu$ is the field strength tensor, $D_\mu = \partial_\mu + ieA_\mu$ is the gauge covariant derivative, ψ is a Dirac spinor, A_μ is the gauge potential and e is the charge associated with the field, in this case the electron. This equation is designed to satisfy the gauge symmetry, which is that under the transformation $\psi \to e^{i\alpha(x)}\psi$, $\bar{\psi} \to e^{-i\alpha(x)}\bar{\psi}$, $A_\mu \to A_\mu + \frac{1}{e}\partial_\mu \alpha\,(x)$, the Lagrangian defined above is invariant. QED would later, because of its structure and its ability to accurately predict quantities, go on to serve as a basis for Yang-mills theory, QCD and other theories.

QED is built on an abelian structure, which means that operations between members of the group commute, $a * b = b * a$. In later theories such as Yang-Mills theory, this is generalised to a non-abelian gauge group. This means that A_μ no longer belongs to the algebra of the unitary matrix group $\mathrm{U}\,(1)$, instead it belongs to the algebra of the special unitary matrix group $\mathrm{SU}\,(N)$, denoted by $\mathfrak{su}(n)$. While QED describes electromagnetic interactions, QCD describes the strong interactions

of quarks which come in six different flavours or varieties: up, down, strange, charm, top and bottom. Whereas in QED the photon is the force carrier of electric charge, in QCD it is the gluon which transmits the colour charge. The strong force between quarks is described using the "colour" label in analogy with the primary colours, hence chromo from the Greek. The analogy is that three colour charges, or a colour and its negative, balance each other out giving a colour neutral state, white in the case of baryons (red, green and blue) and black in the case of mesons (red, anti-red for example). The QCD Lagrangian is given by:

$$\mathcal{L}_{\mathrm{QCD}} = -\frac{1}{4} G^a_{\mu\nu} G^{\mu\nu}_a + \sum_f \bar{\psi}_f \left(i\gamma^\mu D_\mu - m_f \right) \psi_f, \tag{1.3}$$

where $G^a_{\mu\nu} = \partial_\mu A^a_\nu - \partial_\mu A^a_\nu + g f^{abc} A^b_\mu A^c_\nu$ is the field strength tensor, $D_\mu = \partial_\mu + igT^a A^a_\mu$ is the gauge covariant derivative, T^a is a generator of the group and g is the strong coupling constant. The structure of QED is clearly present except there are now the additional group generators of SU (N). Non-abelian theories give rise to self-coupling coming from the additional group term in the field strength tensor. This also results in confinement which can be studied by looking at the behaviour of the quark-antiquark potential on the lattice. For strong coupling limit in pure Yang-Mills theory on the lattice, this is seen as a linearly rising potential. When dynamical quarks are included and there is enough energy to create a new quark-antiquark pair, string breaking occurs and this is observed as a leveling off in the potential. The new quark-antiquark pairs are a lower energy state of the system.

Mesons come as quark antiquark pairs, while baryons are triplets of quarks. The quarks can change colour by absorption or emission of the colour force carrier, the gluon. There are eight varieties of gluons which are represented by the eight generators of SU (3). Confinement causes quarks to remain in colour neutral bound states. However only at small distances and large energies does this property cease to be dominant; this is known as asymptotic freedom. It is believed that as a consequence of this, at high temperature T or high density ρ there is a deconfined phase which I will look at in chapter 2. The structure of QCD does not change with fewer or more flavours N_f, however the masses of particles do vary with the number of flavours present. Increasing the number of flavours also increases the variety of stable state particles that can be constructed. Changing the number of colours N_C directly impacts the types of stable state hadrons formed and the number of force carrying gluons. There is a relation between the number of flavours and colours which gives rise to confinement and asymptotic freedom. This is encapsulated in the β function given by equation (1.4) in the next section.

Perturbative expansions have been used successfully for calculations in QED as the β function for QED which relates the scale to the gauge coupling has a small numerical factor, $\beta \sim \frac{g^2}{4\pi}$. For QCD the β function differs and this method breaks down at low energies and large distances as the coupling grows beyond $g^2 \sim 1$. At finite quark mass and intermediate values of density and temperature, there is a need for non-perturbative techniques to study confinement, chiral symmetry breaking, quantum anomalies and CP violations . A natural solution is to try and use modern computers to solve these complex problems by computing the path integral numerically. By moving from an infinite to a finite number of degrees of freedom, the goal would be to retain the characteristic behaviour of the system while being able to run simulations on a finite classical computer. At the forefront of this is what is known as lattice QCD.

In lattice QCD we use finite lattices as a means of calculation and as a regulator to remove infinities. It is a non-perturbative approach to QCD through regularised, Euclidean functional integrals. The regularisation is based on a discretisation of the action which preserves gauge invariance at all stages. In reality there are limitations due to computer time and it is currently difficult to simulate at non-zero chemical potential μ, an issue known as the sign problem which I will discuss in chapter 2. If we consider the continuum QCD action, it contains finite matrices, numerical constants, continuous integrals and derivatives in terms of complex numbers and Grassmann numbers. The goal is to have a discrete theory on a finite lattice with a small but non-zero lattice spacing, which can approximate the full theory with a reasonable level of accuracy.

1.3 Quantum fields on a lattice

To take advantage of numerical techniques, namely those of statistical mechanics, lattice QCD is constructed on a finite Euclidean grid with three spatial dimensions (x, y, z) and one temporal direction (t). The real universe exists in Minkowski space, so we must first use the Wick rotation to move from Minkowski space to Euclidean space which means that our temporal direction is now imaginary time. Although proven to be mathematically sound by analytic continuation, provided there are no singularities in the way, this dramatically restricts our ability to look at real time objects like correlators or n-particle scattering amplitudes in Minkowski space, so it does come at a price.

Given a spatial extent N_s and a temporal extent N_t and a spatial lattice spacing $a_s = a_x = a_y = a_z$ and temporal lattice spacing a_t, we can describe the four dimensional lattice by volume $V = N_s^3 a_s^3$ and temperature $T = \frac{1}{N_t a_t}$, where N_s and N_t take integer values. In the following discussion, I will talk about constructions in terms of an isotropic lattice of lattice spacing $a = a_s = a_t$. Later I will briefly discuss the possible benefits of using an anisotropic lattice, $a_s \neq a_t$. We can think of our lattice system as a finite system of points or "sites" with connections or "links" between them. As the distance between sites is discrete, any translation between them will also be discrete, so for example: $x \to x + na$, where n is an integer. Any rotation about a site is through 90° so the continuous rotations and translations of the Poincaré group become discrete. The $O(4)$ symmetry group is reduced to the hypercubic symmetry group.

One immediate consequence of the discreteness of the lattice, is the ambiguity of the shortest path between two points. While in reality the shortest path between two points is a straight line, on the lattice this is only the case when the starting point and the final point lie along a Cartesian direction. Otherwise there exists a choice of zigzag paths which may have equivalent length. As the lattice theory is defined with a small but non-zero lattice spacing, describing the continuous world properly means it must equal the full theory in the limit as the lattice spacing a goes to zero which is known as the continuum limit. A physical observable defined on the lattice depends on the gauge coupling g and the cutoff which is the lattice spacing a. As the cutoff is removed, the physical observable should not change, so there is a relationship between the coupling g and the lattice spacing a. This is known as the β function and is given by:

$$\beta(g) = a\frac{\partial g}{\partial a} = \beta_0 g^3 + \beta_1 g^5 + ..., \tag{1.4}$$

where $\beta_0 = \frac{1}{16\pi^2}\left(\frac{11N_c}{3} - \frac{2N_f}{3}\right)$ and $\beta_1 = \left(\frac{1}{16\pi^2}\right)^2\left(\frac{34N_c^2}{3} - \frac{10N_cN_f}{3} - \frac{N_f\left(N_c^2-1\right)}{N_c}\right)$.

Although the β function depends on the renormalisation process used, these first two coefficients are universal. When β_0 is positive, which occurs when $N_f \leq \frac{11N_c}{2}$, it dominates the equation which leads to the continuum limit meaning that the gauge coupling vanishes as the lattice spacing goes to zero which is a property of asymptotic freedom. Changing the number of flavours or colours will result in a QCD like theory with similar limiting properties as long as this relationship is respected. Different renormalisation schemes generally respect this and so in certain limits results from different models can be compared. Most importantly it gives a method of moving

from the simulated finite grid back to continuum physics. In this limit the full $O(4)$ rotational symmetry is recovered [2].

If we now consider a bosonic matter field as being defined on the lattice by the scalar field $\phi(x)$, we can think of it as existing at the lattice sites x_i. If we introduce gauge fields, these are more naturally associated with the links. By convention the fields $\phi(x)$ are defined to have periodic boundary conditions, so $\phi(x_i + Na) = \phi(x_i)$, where N is the number of points in that direction. Periodicity in the temporal direction is necessary to allow for finite temperature calculations. Periodicity in the spatial directions, although not entirely necessary, ensures translational symmetry.

With periodic boundary conditions the volume of space simulated behaves as if it is part of a larger volume. The points on the boundary act as if they were in the centre of the lattice and like the points in the interior, they also interact with their neighbours. The downside of this is that it also allows for the possibility of correlation artifacts. The overall effect would be that if there exists a large enough object (whose correlation length in a particular dimension is larger than the particular dimension's lattice size Na), it would interact with itself as it loops around. This so-called finite volume effect is a constraint on the volume size, a minimum size which can be determined from comparing similar observables on different volumes. Any sizable change measured for observables would be an indication of a dependence on the volume.

Next we define the momentum field $\varphi(p)$ by performing a Fourier transform on the field $\phi(x)$.

$$\varphi(p) = a\sum_{x=1}^{Na} e^{-ipx}\phi(x)\,. \tag{1.5}$$

The momentum p is now in units of $\frac{2\pi}{Na}$ and $\varphi(p)$ is periodic with period $\frac{2\pi}{a}$. The momenta are then contained in the first Brillouin zone $-\frac{\pi}{a} \leq p \leq \frac{\pi}{a}$. This in effect is the introduction of an ultraviolet momentum cutoff $\Lambda = \frac{\pi}{a}$. This natural built-in cutoff is how the lattice acts as a regulator.

1.4 Calculus on the lattice

To calculate any observable on the lattice requires the definition of a discrete version of both the standard integral and the covariant derivative. The integral over

the lattice volume when discretised becomes a sum with a pre-factor of the lattice spacing. This can easily be shown by use of the Trapezoid rule. Consider a function $f(x)$ where $0 \leq x \leq n$. We give it periodic boundary conditions like on the lattice, so $f(0) = f(n)$ and if we set $dx = a$, the integral becomes the sum:

$$\begin{aligned}\int_0^n f(x)\,\mathrm{dx} = af(0) + a\frac{f(1)-f(0)}{2} \\ + af(1) + a\frac{f(2)-f(1)}{2} \\ + ... \\ + af(n-1) + a\frac{f(n)-f(n-1)}{2}.\end{aligned} \tag{1.6}$$

All the central fraction terms cancel leaving $\left[-a\frac{f(0)}{2}\right]$ and $\left[a\frac{f(n)}{2}\right]$ which cancels because of periodicity, leaving a sum of terms $\sum f(x)$ multiplied by the lattice spacing a. This argument can be extended to higher dimensions, picking up an extra factor of a for each extra dimension.

$$\int d^4x \longrightarrow a^4 \sum. \tag{1.7}$$

The discretisation of the derivative is somewhat more complicated. Consider an ordinary derivative of the field $\phi(x)$ on the lattice, we can see that there is no unique discretisation of the derivative. Using only first order terms, the most obvious definitions for the derivative are: forward ∂^f, central ∂^c, or backwards derivative ∂^b, given by

$$\begin{aligned}\partial^f_\mu \phi(x) &= \frac{1}{a}\left[\phi(x+a\hat{\mu}) - \phi(x)\right], \\ \partial^c_\mu \phi(x) &= \frac{1}{2a}\left[\phi(x+a\hat{\mu}) - \phi(x-a\hat{\mu})\right], \\ \partial^b_\mu \phi(x) &= \frac{1}{a}\left[\phi(x) - \phi(x-a\hat{\mu})\right],\end{aligned} \tag{1.8}$$

where the derivatives are in direction μ. It is possible to define higher order terms, but the point is that there is an ambiguity in the discretisation of the derivative, non-symmetric or symmetric. In the continuum limit these all approach the definition for the derivative. As we want to retain gauge invariance on the lattice, we define

a covariant derivative in line with real QCD, $D_\mu = \partial_\mu + iqA_\mu$. To ensure this remains gauge invariant for objects which depend on a point $\phi(x)$ and a point an infinitesimal distance away, $\phi(x+dx)$, we must define the parallel transporter. This is an operator defined for vector transformations which maintains the properties of the original system with respect to the co-ordinate basis during transformation. On the lattice we can define the covariant derivative as

$$D_\mu \phi(x) = \frac{1}{a}\left[U(x, x+\hat{\mu})\,\phi(x+\hat{\mu}) - \phi(x)\right], \tag{1.9}$$

where $U(x, x+\hat{\mu}) = U_{x,\mu} = \exp\left[-iqA_\mu(x)\,a\right]$. This can then be easily extended to other charges and a greater number of dimensions by replacing $qA(x)$ with $gt^a A^a$ where g is the associated charge and t^a are the generators of the group. This link variable is the natural object to work with on the lattice, so a lattice gauge field can be thought of as a set of SU (N) matrices $U_\mu(x)$ where $\mu = 0, 1, 2, 3$. We are now able to consider the operator constructed from the parametrised path ordered integral running from $s = 0$ at $x = y$ to $s = 1$ at $x = z$

$$U_{\mathcal{P}}(z, y) = \mathcal{P}\left\{\exp\left[ig\int_0^1 ds \frac{dx^\mu}{ds} A_\mu^a(x(s))\,t^a\right]\right\}, \tag{1.10}$$

known as a Wilson line, where $\mathcal{P}$ denotes path ordering. Note: $U_{\mathcal{P}}(z, y) = U_{\mathcal{P}}^\dagger(y, z)$. Using this construction we can define the only two objects which are inherently gauge invariant constructed out of the sites and links, a Wilson line which is given by $\phi^\dagger(z)\,U_{\mathcal{P}}(z, y)\,\phi(y)$ and a Wilson loop which can be defined as $\mathrm{Tr}\left[U_{\mathcal{P}}(x, x)\right]$ where the trace of $U_{\mathcal{P}}(x, x)$ is taken around a closed loop. By constructing our lattice theory out of these gauge invariant objects, the theory will be gauge invariant.

1.5 Symmetries

Symmetries play a key role in the construction of theories in physics and the predictions which come from those theories. Geometric symmetries dependent on dimensions, topology and discreteness or continuity often play a central role. Gauge symmetry, isospin symmetry and chiral symmetries all influence model constructions. Bounds on masses based on symmetries prove useful for both experiment and theory. With regards to the lattice, the discreteness in terms of volume V and lat-

tice spacing a_s is taken into account when comparing points that are an equivalent distant apart for example. Gauge symmetry is respected and is described by:

$$\psi \to V(x)\psi \qquad \bar{\psi} \to V^{\dagger}(x)\bar{\psi} \qquad U_{\mu} \to V(x)U_{\mu}V^{\dagger}(x+\mu), \tag{1.11}$$

where $V(x)$ is in the same representation as U.

Flavour symmetries

The masses of the quarks, and their relationship to one another, are also the subject of much interest in terms of what is known as the chiral symmetry, and the effect breaking this symmetry has on the mass spectrum. The Goldstone theorem states that for every broken global generator, there is a corresponding zero mass scalar (or pseudo-scalar) state in the particle system. In the case of massless quarks, the action is invariant under the following transformations:

$$\psi_{L,R} \to e^{i\alpha^a_{L,R}t^a}\psi_{L,R} \qquad \bar{\psi}_{L,R} \to \bar{\psi}_{L,R}e^{-i\alpha^a_{L,R}t^a}, \tag{1.12}$$

where $\psi_{L,R} = \frac{1}{2}(1 \pm \gamma_5)\,\psi$ and $\bar{\psi}_{L,R} = \frac{1}{2}\bar{\psi}\,(1 \mp \gamma_5)$. As the up and down quark masses are almost equivalent $m_u, m_d \simeq 10\text{MeV}$, we get an exact global flavour symmetry if we say they are equal. This can be written in terms of vector symmetry denoted by V as:

$$\mathrm{U}(2)_{\mathrm{V}} = \mathrm{U}(1)_{\mathrm{V}} \otimes \mathrm{SU}(2)_{\mathrm{V}}\,, \tag{1.13}$$

where the first factor corresponds to conservation of quark number, and the second factor is the isospin symmetry. If we set $m_u = m_d = 0$, this is extended to axial symmetry denoted by A giving:

$$\mathrm{U}(2)_{\mathrm{V}} \otimes \mathrm{U}(2)_{\mathrm{A}} = \mathrm{U}(1)_{\mathrm{V}} \otimes \mathrm{U}(1)_{\mathrm{A}} \otimes \mathrm{SU}(2)_{\mathrm{V}} \otimes \mathrm{SU}(2)_{\mathrm{A}}\,. \tag{1.14}$$

In reality $\mathrm{U}(1)_{\mathrm{A}}$ is anomalously broken by quantum effects (axial anomaly), and $\mathrm{SU}(2)_{\mathrm{A}}$ is spontaneously broken by vacuum expectation value of scalar quark condensates. The Goldstone theorem then means the appearance of three massless pseudo-scalar bosons in the zero quark mass limit. If $m_s = 0$ (which is a worse

approximation as $m_s \approx 100\text{MeV}$), then equation (1.14) becomes:

$$\mathrm{U}(3)_{\mathrm{V}} \otimes \mathrm{U}(3)_{\mathrm{A}} = \mathrm{U}(1)_{\mathrm{V}} \otimes \mathrm{U}(1)_{\mathrm{A}} \otimes \mathrm{SU}(3)_{\mathrm{V}} \otimes \mathrm{SU}(3)_{\mathrm{A}}\,. \tag{1.15}$$

Of course in the real world, the quarks are not massless so $\mathrm{SU}(3)_{\mathrm{V}} \otimes \mathrm{SU}(3)_{\mathrm{A}}$ is explicitly broken and the Goldstone bosons acquire a mass and become pseudo-Goldstone bosons. Constructing a computational system which can accurately describe real QCD while allowing for the study of various symmetries is key. Using masses larger than the physical values can decrease the cost of calculation but can mean that an extrapolation to physical quark masses becomes difficult.

Centre symmetry

In pure gauge theory the centre symmetry is useful in determining whether the system is in the confined or deconfined phase. The centre symmetry is defined as the transformation [3]:

$$U_{x,\mu} \to \begin{cases} zU_{x,\mu} & \text{if } x_4 = 0 \text{ and } \mu = 4 \\ U_{x,\mu} & \text{otherwise} \end{cases} \tag{1.16}$$

where z is an element of the centre group $\mathbb{Z}_n$ of the gauge group $\mathrm{SU}(N)$, $\vec{x}$ is the position vector, so x_4 is the temporal part of $\vec{x}$ and μ is the direction in which U is pointing, $U_{x,\mu} = U(x, x + \hat{\mu})$. For pure gauge theory the transformation is respected as z commutes with all the elements. For dynamical quarks it becomes an indicator of the phase transition between confined and deconfined matter as it is no longer a symmetry which I will discuss in chapter 2.

1.6 QCD on the lattice

Gauge invariance on the lattice puts a restriction on the types of objects that can be used to generate an action, namely the Wilson loop and the Wilson line. The quark propagator can be defined on the lattice as the expectation value of a quark and anti-quark separated by some number of gauge links. This separates the action into a fermion part which is integrated out leaving a non-local effect on the gauge fields given by the determinant of M, and a gauge part given in terms of the link variables U. An expectation value in QCD at zero chemical potential can be written

in terms of the gauge and quark fields as

$$\langle O\left(U,q,\bar{q}\right)\rangle = \frac{1}{Z}\int\left[dU\right]\prod_{f}\left[dq_{f}\right]\left[d\bar{q}_{f}\right]O\left(U,q,\bar{q}\right)e^{-S_{g}-S_{q}}, \tag{1.17}$$

where $Z = \int\left[dU\right]\prod_{f}\left[dq_{f}\right]\left[d\bar{q}_{f}\right]e^{-S_{g}-S_{q}}$ and $S_{q} = \sum_{f}\bar{q}_{f}Mq_{f}$, M is the Dirac operator. Because of the peculiar rules of calculus of Grassmann numbers, it is possible to integrate them out analytically before a simulation has even started. Z can then be defined as

$$Z = \int\left[dU\right]e^{-S_{g}}\prod_{f}\det\left(M\right), \tag{1.18}$$

where the determinant term represents the fermionic back reaction on the gauge fields. Expectation values of the fermionic operators can be written in terms of the fermion propagator S, which is the inverse of the fermion matrix M. We are left with a determinant term and an exponential term over the gauge fields and in this form it is something which we can calculate on a computer.

1.7 The Wilson plaquette gauge action

The simplest gauge action is created from plaquettes, which are 1×1 Wilson loops. More complicated loops in higher number of dimensions are also possible and may be used to improve the accuracy of gauge actions. The continuum Yang Mills action in Euclidean space-time is defined as:

$$S_{E}\left[A\right] = -\frac{1}{2g_{0}^{2}}\int d^{4}x\mathrm{Tr}\left(F_{\mu\nu}\left(x\right)F_{\mu\nu}\left(x\right)\right). \tag{1.19}$$

It can be shown that the lattice equivalent is, using plaquettes:

$$S_{E}\left[U\right] = \beta\sum_{x\in\Lambda_{E}}\sum_{\mu,\nu,\mu<\nu}\left(1-\frac{1}{N}\mathrm{ReTr}P_{\mu\nu}\left(x\right)\right). \tag{1.20}$$

The gauge coupling β is defined as $\beta = \frac{2N}{g_{0}^{2}}$, (not to be confused with the β function or $\beta = \frac{1}{k_{B}T}$) where g_{0} is the bare coupling which controls the continuum limit as mentioned earlier. The lattice actions are defined as dimensionless, so there is no direct dependence on the lattice spacing a_{s}.

1.8 Wilson fermion action

The task of representing fermions on a classical computer is much more troublesome. Consider the classical Euclidean action for free fermions in the continuum:

$$S_q\left[\bar{\psi},\psi\right]=\int d^4x\bar{\psi}\left(x\right)\left(\gamma_\mu\partial_\mu+m\right)\psi\left(x\right), \tag{1.21}$$

where $\bar{\psi}$ and ψ are Grassmann variables describing the fermions. If we discretise this we get the naive fermion action:

$$S_{naive}\left[\bar{\psi},\psi\right]=a^4\sum_x\left\{\sum_\mu\bar{\psi}\left(x\right)\gamma_\mu\frac{\psi\left(x+\hat{\mu}\right)-\psi\left(x-\hat{\mu}\right)}{2a}+m_0\bar{\psi}\left(x\right)\psi\left(x\right)\right\}. \tag{1.22}$$

In momentum space [4], we get the propagator

$$\left\langle\bar{\psi}\left(-p\right)\psi\left(p\right)\right\rangle=\left[i\sum_\mu\gamma_\mu\frac{1}{a}\sin\left(p_\mu a\right)+m\right]^{-1}, \tag{1.23}$$

which has the dispersion relation of the form

$$\sinh^2\left(E\left(\vec{p}\right)a\right)=\sum_i\sin^2\left(p_ia\right)+\left(ma\right)^2. \tag{1.24}$$

This approaches the continuum dispersion relation in the continuum limit $a\to0$. At zero quark mass, the poles for the propagator, lie at $\vec{p}=0$ and π giving 2^d modes at the edges of the Brillouin zone. This is known as the fermion doubling problem and in this form we will get both the "real" quark and the contributions from these other doublers. These are not errors, but an effect caused by the discrete representation which in the continuum limit gives the correct answer. This is a serious problem which has been studied by many groups. One study in particular detailed the limits given by the initial algebraic constructions of the lattice theory. It is quoted as the Nielsen-Ninomiya no-go theorem [5]. In essence it means the following:

If the action is local, bi-linear in $\bar{\psi},\psi$, invariant under translation, hermitean, chirally symmetric and contains conserved charges with discrete eigenvalues, then the spectrum contains an equal number of left-handed and right-handed fermions for each quantum number.

What this means is that no matter what solution we come up with for this problem, we will do so at the loss of another property. So the choice of quark action is guided by what properties you are investigating. Chiral symmetry although important can be ignored in some studies. In the case of the Wilson fermion action we sacrifice chiral symmetry by giving the doublers a mass which breaks chiral symmetry explicitly, even for $m_q = 0$. The non-interacting Wilson fermion action can then be written in terms of position as:

$$S_{Wilson} = \sum_x \left\{ \bar{\psi}_x \left(m + \frac{4r}{a} \right) \psi_x + \frac{1}{2a} \sum_\mu \bar{\psi}_x \left[(\gamma_\mu - r) \psi_{x+\hat{\mu}} - (\gamma_\mu + r) \psi_{x-\hat{\mu}} \right] \right\}. \quad (1.25)$$

The Wilson parameter r now controls the existence of doublers on the lattice. By setting r to zero, we return to the naive fermion action. By a change of variables we can rewrite it as

$$S_{Wilson} = \sum_x \left\{ \bar{\Psi}_x \Psi_x + \kappa \sum_\mu \bar{\Psi}_x \left[(\gamma_\mu - r) \Psi_{x+\hat{\mu}} - (\gamma_\mu + r) \Psi_{x-\hat{\mu}} \right] \right\}, \quad (1.26)$$

where $\bar{\psi}_x = \frac{\bar{\Psi}_x}{\sqrt{m+\frac{4r}{a}}}$, $\psi_x = \frac{\Psi_x}{\sqrt{m+\frac{4r}{a}}}$, and $\kappa = \frac{1}{2ma+8r}$ is known as the hopping parameter and describes how quarks "hop" from site to site. This extra r dependent term is effectively a mass for the doublers which means that the physical mass that we are trying to simulate is now determined not only by m but also by this extra term. In the chiral limit we then need to approach $\kappa = \kappa_c$, where the critical value is related to the vanishing pion mass which due to additive mass renormalisation is no longer at $m_0 = 0$. This is one of the reasons why a quark action which respects chiral symmetry is much sought after as this would protect against additive mass renormalisation. The Wilson fermion matrix in terms of the momentum p is then:

$$M[p] = \left\{ m + \frac{1}{a} \sum_\mu \left[i\gamma_\mu \sin(p_\mu a) + r(1 - \cos(p_\mu a)) \right] \right\}, \quad (1.27)$$

which has a zero at $p_\mu = 0$ for each μ where $m = 0$, but $p_\mu = \frac{\pi}{a}$ now doesn't result in a zero, giving $\frac{2r}{a}$ instead. This additional r term solves the doubling problem at the cost of chiral symmetry. The lattice gauge and quark actions are approximates which approach the real gauge and quark action in the continuum limit. That being said some actions are better suited to studying the chiral symmetry than others.

Other types of fermion action:

The no-go theorem gives rise to a large variety of quark actions, which in the continuum limit become equivalent in principle. The range of research briefs, computer resources and accuracy requirements lead to custom built actions designed to look at particular objects. Popular alternatives include:

Staggered (Kogut-Susskind) fermions:

The staggered fermion action [6] counters the fermion doubling problem at source by altering the lattice so that the Brillouin zone is reduced. This is done by doubling the effective lattice spacing which reduces the fermion doubling problem. In essence by distributing the components of the Dirac action over a sublattice. From the naive quark action, it is possible after some work, to spin-diagonalise which gives four identical actions. If we then use only one of them, it reduces the sixteen fermion doublers to only four. The staggered quark action can be written in the form:

$$S_F = -\sum_{x,\mu} \eta_{\mu x} \frac{1}{2} \left[\overline{\chi}_{ax} \left(U_{\mu x} \right)_{ab} \chi_{bx+\hat{\mu}} - \overline{\chi}_{ax+\hat{\mu}} \left(U^{\dagger}_{\mu x} \right)_{ab} \chi_{bx} \right] - \sum_{x} m \overline{\chi}_{ax} \chi_{ax}, \quad (1.28)$$

where a and b are colour indices. In this form we see there are no spin or flavour indices for χ or $\overline{\chi}$. In the continuum limit this action describes four mass degenerate flavours of quarks. The staggered action has a remnant chiral $\mathrm{U}(1)$ symmetry, meaning that approaching the limit of the bare quark mass $m_0 = 0$ corresponds to the limit $m = 0$. The reduction of flavours to staggered flavours is an exact transformation. The staggered action is computationally cheaper than the Wilson fermion and can be further improved by replacing the determinant with the fourth root of their determinant, although the legitimacy of the rooting process is disputed [7].

$$\mathcal{Z}_{Stagg} = \int [dU] \, e^{-S_g[U]} \prod_i \det \left[M_i \left(U \right) \right]^{\frac{1}{4}}, \quad (1.29)$$

In the case of rooting, the continuum limit must be taken before the quark mass limit while the quark flavour symmetry is broken at finite lattice spacing. The sites are now occupied by linear combinations of the fermion fields.

Ginsparg-Wilson fermions:

The Ginsparg-Wilson [8] relation is an exact symmetry of the Dirac operator which becomes equivalent to a chiral symmetry in the continuum limit.

$$\{\gamma_5, D\} = \gamma_5 D + D\gamma_5 = aD\gamma_5 D. \tag{1.30}$$

In the continuum the right hand side vanishes, but on the lattice it does not vanish with the two factors of D restricting chiral violations to short distances which do not contribute to physical matrix elements. This relation leads to two alternative forms, the Domain Wall [9] and Overlap fermions [10]. For Domain Wall fermions, the idea is to add a 5th dimension, creating five-dimensional Wilson fermions with gauge links in four-dimensions which remain independent of the new dimension which is conventionally called s. This substantially reduces the chiral symmetry problem without the doubling problem as experienced at finite lattice spacing for staggered fermions. The cost however is this new dimension and the overhead of interactions with it. For Overlap fermions the starting point is also the addition of a 5th dimension. The idea is to write the overlap of Hamiltonians in this 5th dimension.

$$aD = M\left[1 + \gamma_5 \varepsilon \gamma_5 D_\omega\left(-M\right)\right], \tag{1.31}$$

where $\varepsilon\left(x\right) = \frac{X}{\sqrt{X^2}}$. Although Ginsparg-Wilson fermions are better suited to dealing with chirally sensitive areas of research, they are more expensive to simulate as there are five dimensions rather than four.

Twisted mass fermions:

Twisted mass fermions [2] are effectively a doublet of unimproved Wilson fermions with a mass term which is chirally twisted, hence the name. Because of the formulation the chirally twisted masses actually have an $\mathcal{O}\left(a\right)$ improvement at the largest twist, but can still be shown to be equivalent to QCD in the continuum limit. As a consequence of this twist they break flavour symmetry. The twisted mass Dirac operator for two quark masses is given by:

$$D_{tmQCD} = D_W + m_0 + i\mu_q \gamma_5 \tau^3,$$

where D_W is the massless Wilson-Dirac operator, m_0 is the standard bare quark mass, μ_q is the twisted mass parameter and τ^3 is a Pauli matrix acting in flavour space [11]. For $\mu_q = 0$, there is minimal twisting and we are left with the Wilson action.

1.9 Alternatives and improvements

Another consequence of the continuum limit is that there is no unique definition for operators or the gauge and fermion actions. This allows for many different variations as shown already in the variations of the quark action. Adding higher order terms in principle allows for a reduction in discretisation errors and a possible improvement in the chiral or continuum limits. The improvements to the Wilson gauge action are more complicated combinations of plaquettes and larger Wilson loops which I will cover in the improved actions section on page 19. First I will briefly discuss one popular alternative method, which is switching to an anisotropic lattice.

Anisotropic Lattices:

So far I have discussed lattices with isotropic spacing, $a = a_s = a_t$. Alternatively we could define a lattice where the spatial and temporal lattice spacings differ, which is known as a $3+1$ anisotropic [12] lattice ($a_s \neq a_t$), where we define the anisotropy as $\xi = \frac{a_s}{a_t}$. Strictly speaking an anisotropic lattice is where not all the lattice spacings are identical, and some studies have used one fine spatial, one fine temporal and two coarse spatial lattice spacings, known as a $2+2$. Studying quantities which rely on a high resolution in the temporal direction, such as mass fits or spectral functions, need not only a large enough volume but a large number of points in the temporal direction to allow for an identification of plateaus which requires a decent level of resolution in the temporal direction.

Improving this can be costly on an isotropic lattice but on an anisotropic lattice the improvement can be made in the temporal direction while keeping the spatial lattice spacing relatively coarse to reduce the extra computational cost as much as possible. The use of anisotropic lattices also allows for change of temperature by either varying a_t or N_t which we discuss in the next chapter. When looking at volume or temperature derivatives which arise in equation of state calculations, anisotropic lattices can provide the information necessary by allowing the user to fix the spatial volumes and vary the temperature $T = \frac{1}{N_t a_t}$ or vice-versa.

There is an extra overhead of calculating the anisotropy, which is required to restore Euclidean invariance. Once you turn on interactions, renormalisations occur which means the measured anisotropy ξ may vary from the input anisotropy γ. In fact there may be different anisotropies for the fermion and gauge actions. For the quenched case this is not a problem as the gauge field does not see the fermion field, so the input gauge and quark anisotropies γ_g and γ_q can be tuned separately. For dynamical fermions the measured anisotropies ξ_g and ξ_q are no longer independent. The correct anisotropy ξ is needed to ensure that a massless meson propagates at the correct speed of light. Apart from this retuning, there are now extra terms in the action which means extra computations, but when looking at objects which depend on the temporal lattice spacing, the pros may outweigh the cons.

Improved Actions:

Decreasing the lattice spacing, lowering the quark mass, increasing the volume and increasing statistics are generally seen as ways of improving the quality of results at the cost of an increased number of computations. With finite computational time and the reality of simulating at finite but non-zero lattice spacing, improvements in the action allow for smoother extrapolations and for the removal of low order lattice artefacts. There are a number of changes which can be made to improve the chosen gauge and quark actions. These generally increase the cost of calculation but in principle give a sizable improvement in terms of keeping discretisation errors to a realistic minimum. The philosophy of all these improvements is similar; add terms to the existing gauge or quark action to counteract terms which give errors so as to reduce the errors at finite lattice spacing.

A simple example of this is the addition of some term multiplied by the lattice spacing to the action. This term would then disappear as the lattice spacing goes to zero:

$$S_{lattice} \rightarrow S_{lattice} + (a)\,(term) \xrightarrow{a \rightarrow 0} S_{continuum}. \tag{1.32}$$

For the interacting case this becomes more complicated as the additional term may be divergent in the continuum limit. Using the language of the Renormalisation group, we are looking for irrelevant operators, ie they vanish at the fixed point at $a \rightarrow 0$ [13]. Using this property we can add terms to counteract discretisation effects at finite lattice spacing which can help give a smoother extrapolation to zero lattice spacing. These improved actions agree at tree level with the original unimproved action. As mentioned earlier when discussing the discrete derivative, the addition of higher order terms allows for a better approximation. As always, there is a trade off

between computation time, statistics and the quality of the results which depends on amongst other things, the errors of the chosen action and the lattice spacing. I will briefly go through some of the more popular improvements.

Symanzik improvement:

Symanzik improvement [14] is the systematic removal of lattice artifact terms in the lattice spacing expansion of the lattice actions and operators. Consider the symmetrised derivative:

$$f_c = \frac{f(x+a) - f(x-a)}{2a} = f'(x) + \frac{a^2}{6} f^{(3)}(x) + ... \tag{1.33}$$

When expanded it is clear that this is a series of even powered terms. By adding a counter term to cancel the first even power we can improve f_c to give $f_c^S = f' + \mathcal{O}(a^4)$, where f_c^S is now Symanzik improved. If we apply the same philosophy to lattice QCD actions we can improve the order of errors by adding the correct counter-term. This improvement is not as straightforward as in the example above, but can be calculated perturbatively. An example of this is the two-plaquette Symanzik improved or TSI action which has errors of the order $O(a_s^4, a_t^2, \alpha_s a_s^2)$ as opposed to the standard Wilson gauge action which has errors of $O(a^2)$. It is defined as:

$$\begin{aligned} S_g = \beta \Bigg[\frac{1}{\xi_g^0} \left\{ \frac{5(1+\omega)}{3u_s^4} \Omega_s - \frac{5\omega}{3u_s^8} \Omega_s^{(2t)} - \frac{1}{12u_s^6} \Omega_s^{(R)} \right\} \\ + \xi_g^0 \left\{ \frac{4}{3u_s^2 u_t^2} \Omega_t - \frac{1}{12u_s^4 u_t^2} \Omega_t^{(R)} \right\} \Bigg], \end{aligned} \tag{1.34}$$

where u_s and u_t are the average link value in the spatial and temporal directions respectively, Ω_s and Ω_t are the respective spatial and temporal plaquette terms, $\Omega_s^{(2t)}$is a pair of spatial plaquette terms separated by a single temporal link and $\Omega_s^{(R)}$ and $\Omega_t^{(R)}$ are the respective spatial and temporal 2×1 rectangular Wilson loop terms. The additional separated plaquette term is controlled by ω which can be set to zero to recover the mean field improved tree level Symanzik action. For the fermion action, one example is the Sheikholeslami-Wohlert [15] or clover action, named after the authors and the shape traced out by the additional terms $\hat{F}_{\mu\nu}$ and can be written [16] as:

$$S_{Clover} = S_{Wilson} + c_{SW} i g a^4 \sum_{x,\mu,\nu} \frac{1}{4a} \bar{\psi}(x) \sigma_{\mu\nu} \hat{F}_{\mu\nu}(x) \psi(x), \tag{1.35}$$

where S_{Wilson} is the original Wilson quark action, c_{SW} is the Sheikholeslami-Wohlert

coefficient, $\sigma_{\mu\nu} = \frac{i}{2}[\gamma_\mu, \gamma_\nu]$ and $\hat{F}_{\mu\nu}(x)$ is the discretised version of the field strength tensor given by:

$$\hat{F}_{\mu\nu}(x) = \frac{1}{8iga^2} \sum_{\mu,\nu=\pm} \left(U_{\mu\nu}(x) - U^\dagger_{\mu\nu}(x) \right) \tag{1.36}$$

Mean field prescription:

The gauge field can similarly be expanded [13] in terms of increasing order:

$$U_\mu(x) = e^{iagA_\mu(x)} = 1 + iagA_\mu(x) - \frac{a^2g^2}{2} A^2_\mu(x) + ... \tag{1.37}$$

This give rise to quark-gluon vertices with increasing numbers of gluons, while only the first two terms are not lattice artifacts. The two gluons in the A^2_μ term above can be contracted giving a tadpole diagram. The mean field or tadpole prescription [17] amounts to removing tadpole diagram effects by dividing each link by the average or mean field measurement of the links, $\tilde{U}_\mu(x) = u_o U_\mu(x)$. This removes a certain amount of quantum noise on the more troublesome configurations. The TSI action given above in equation 1.34 is an example of a mean field improved action.

1.10 Numerical Computations

At this stage we have discussed the motivation for defining physics in terms of an action S and the procedure in place to derive lattice actions which have the proper continuum limit. We now have various discretised actions to describe both the gauge and quark sectors with the aim to calculate observables using the computational power of Lattice QCD, but we have yet to look at how this is achieved. We have discussed how calculations can be divided into an exponential describing the gauge field and a determinant of the fermion matrix:

$$Z = \int [dU]\, e^{-S_g} \prod_f \det(M)\,. \tag{1.38}$$

Calculating the determinant takes up the majority of computation time, so up until the mid nineties research groups decided to save considerable computer time by setting this determinant equal to one. This is known as quenching, while simulations

which take the full determinant into account are known as simulations with dynamical fermions. It reduces computation costs drastically, at the cost of glossing over the influence of sea quarks. This method contains uncontrolled errors and for some quantities [18] [19] these errors are estimated to be as high as $10 - 20\%$.

Simulating QCD on a computer raises a number of issues. For a simulation of several sets of configurations with different parameters there is no guarantee that they are simulating the same physics. Ideally these sets would lie along a line of constant physics, which is defined as the curve in the space of the bare parameters along which ratios of physical quantities remain approximately constant.

Mass:

Another factor which could be used to decrease computation time was the quark masses. The inversion of the fermion matrix M has eigenvalues which depend on the mass of the quarks. Quenching and simulating heavier quark masses are ways to balance the cost of simulations to achieve respectable statistics in a reasonable amount of time. By increasing the mass value, the cost of inverting the matrix goes down, and as the cost of inverting the matrix is a large percentage of computer time, this seems a sensible option. An extrapolation to physical quark masses is then needed to give results which should compare with experiment. Although the results are improved when using dynamical fermions, the quark mass extrapolation has turned out to be rather troublesome as it relies on chiral perturbation theory where the range of validity is unclear [13] [2].

A number of different combinations are possible. Degenerate masses speed up simulations, and as the up and down quarks are approximately degenerate they are normally set to the same mass $m_q = m_u = m_d$ which is set to a larger value than the physical value, and then extrapolated to the physical value. The strange quark is somewhat heavier, and recent simulations use the physical value, known as $2 + 1$ flavour to distinguish $2m_q + m_s$. There has also been research using a $2 + 1 + 1$ flavour action [20], that is $2m_q + m_s + m_c$. The top and bottom are much heavier and restrict calculations to either prohibitively large volumes to cater for both the light quarks m_q and the much heavier quarks, or to use an effective Lagrangian, for example non-relativistic QCD (NRQCD). For the purposes of this thesis, we restrict ourselves to two degenerate flavours $m_q = m_u = m_d$.

Monte Carlo:

The art of performing complicated calculations, generating statistics using random numbers and solving multidimensional integrals on a computer has been around since the early 1950s. Since then there has been significant interest in the area as numerical calculations are used across many different fields, from physics, biology and chemistry to engineering, design and the financial sector. A euclidean correlation function can be written in terms of an infinite-dimensional path integral [21]:

$$\langle 0 \left| T \left\{ \phi \left(x_1 \right) ... \phi \left(x_n \right) \right\} \right| 0 \rangle \overset{def}{=} \int \left[d\phi \right] \phi \left(x_1 \right) ... \phi \left(x_n \right) e^{-S_E[\phi]}, \tag{1.39}$$

where we can use the Riemann definition of an integral to divide the continuous integral into a sum of parts with width a which in the limit as a goes to zero approaches the correct answer. This becomes rather expensive for multidimensional integrals, so we switch to using stochastic methods, namely the Monte Carlo method. The Monte Carlo algorithm is a non-deterministic calculation which uses a finite number of points to approximate the full calculation, which it approaches in the infinite limit. As the degrees of freedom increases, the Monte Carlo method becomes more efficient per degree of freedom. For example we move from a large one dimensional integral to a finite sum over N randomly chosen points $x^{[i]}$ with uniform distribution over the domain (α, β), which in the infinite limit approaches the full integral:

$$I \left(N \right) = \frac{\beta - \alpha}{N} \sum_{i=0}^{N-1} f \left(x^{[i]} \right) \underset{N \to \infty}{\longrightarrow} \int_{\alpha}^{\beta} f \left(x^{[i]} \right) dx. \tag{1.40}$$

Of the possible areas in phase space, some influence the integral more than others. Focusing on those is what is known as importance sampling, and allows for biasing towards results which contribute the most to the final answer. Assume there exists a function $g \left(x \right) > 0$ such that $\int_a^b dx g \left(x \right) = 1$ and $h \left(x \right) = \frac{f(x)}{g(x)}$ is close to constant. We can then calculate the integral of $f \left(x \right)$ in terms of the function $h \left(x \right)$ and the probability density $g \left(x \right)$. If we then use importance sampling we generate a sample mean which approaches the same value in the infinite limit.

$$\left\langle f \right\rangle_{\rho} = \lim_{N \to \infty} \frac{1}{N} \sum_{n=1}^{N} f \left(x_n \right), \tag{1.41}$$

where x_n are sampled using

$$dP(x) = \frac{g(x)}{\int_a^b dg(x)}. \tag{1.42}$$

In practice this converges to the solution quicker than the naive Monte Carlo method. This alters the probability density $P(x_i)$ to edge the system towards solutions which have a larger effect on the integral. In short, it uses the action as a probability density to pick points. This however places a constraint on the exponential term in equation 1.39, namely it must be real valued and positive. For the Hamiltonian to be self-adjoint and used as a probability weight, the transfer matrix must satisfy reflection positivity, that is, it must be symmetric, bounded and positive operator acting on a Hilbert space of states with a positive norm [13].

Given a set of initial parameters, we can construct a configuration. We start with either a cold or hot configuration meaning gauge field is set to zero or randomly generated respectively, and then evolve the configuration using an updating process. Local updating involves comparing sites with neighbouring sites and doing this for each site individually which when done once for all sites is a sweep. Global updating involves using information from the entire configuration to generate possible changes. Starting with a configuration of initial conditions and evolving this based on probabilities at each time step creates a chain of probabilities known as a Markov chain. An important factor is that at each position the next possible step only depends on the probabilities of that next step from that position. There is no memory of previous steps or results which allows the system to revisit states.

The molecular dynamics model, introduces an equation of motion making it deterministic and allows for global moves rather than local updating. This depends on the finite step size in the time evolution of the system. Increasing the step size reduces the run-time but also might give errors which are not obvious. The Metropolis algorithm [22] named after one of its authors Nicholas Metropolis is a Monte Carlo algorithm which incorporated the Markov chain which allows for random walk behaviour. In 1987 the hybrid Monte Carlo method (HMC) [23] was developed which is a hybrid of the Metropolis algorithm and molecular dynamics. Random walks can lead to increased configuration generation time as each step may be valid but does not advance towards a thermalised configuration. By using long trajectories it avoids random walks and uses a accept/reject step. HMC in theory has no systematic errors and it is an exact method with no step size dependence. Increasing the step size only lowers the acceptance rate and so the step size becomes an auto-

correlation control. HMC is currently the most popular algorithm setup due to its efficiency while maintaining ergodicity and detailed balance.

Ergodicity means that all of the configuration space is sampled and so the sets generated reflects the physics it is simulating. This means that every configuration can be reached with a finite probability from any other one. Algorithms which are not ergodic might not give a full representation of the physics being studied as they are skewed away from some configurations. For the system to be in equilibrium for a given distribution p_μ a sufficient condition is known as detailed balance if the transition probabilities P satisfy [24] $p_\mu P(\mu \to \nu) = p_\nu P(\nu \to \mu)$, where $P(\mu \to \nu)$ is the probability of going from the state μ to the state ν. This means that although the system is still updated, the overall effect is that it remains the same for a distribution in equilibrium.

Although powerful, practicing lattice QCD is a rather sensitive balancing act. Ideally research would be carried out using an improved action on a large number of sets of uncorrelated configurations with physical masses on large volumes with relatively fine lattices for a range of temperatures and densities. In reality computational resources and a limited time to generate configurations and carry out analysis generally limits any research project. In addition introducing a non-zero density to simulations can cause the Hamiltonian to no longer be a positive quantity which I will discuss in the next chapter.

Using improved actions can be an unnecessary luxury for initial studies where a high level of accuracy is not needed. After comparing methods, closing in on parameters of interest, pinpointing errors and focusing on areas of future interest they may be needed to give accurate results. While improved actions can be costly, they can be useful to reduce specific errors known to cause problems for certain studies, improve signal/noise ratio in temporal direction for example. A reasonable number of uncorrelated configurations can reduce statistical errors. This becomes a trade-off between time taken and level of accuracy. As creation of configuration sets is the most expensive part of the calculation, various groups have made configuration sets freely available online.

Studies at particular temperatures and volumes are also cheaper. For QCD there is a critical temperature denoted by T_c which coincides with transition between the confined and deconfined regions in the phase diagram. As the temperature is inversely proportional to number of time slices N_t, simulating at higher temperature

is cheaper although autocorrelations are higher near T_c. Calculations often require a vacuum subtraction which will require at least one set of "cold" configurations with large N_t. The volume size is dependent on the magnitude of the quark masses as they place a constraint via finite volume effects. All these various alterations which are not all independent, can depend on the particular object of interest being studied. Choices can then be made in terms of which action, whether it is improved, whether it is quenched, the size of the lattice spacing (not directly as it is tuned using β) and whether the action is isotropic or not anisotropic.

2 Thermodynamics on the Lattice

2.1 Overview

In this chapter I will discuss simulating physics on the lattice at high temperature T and finite density (in terms of chemical potential μ_q). In particular I will discuss the sign problem which occurs for non-zero chemical potential and list some of the alternative approaches. I will give the motivation for studying two-colour QCD and some of the thermodynamic quantities which lattice QCD can investigate. I will also look at various order parameters which can be calculated on the lattice which are appropriate for capturing critical behaviour and describing phase transitions in QCD. This ability to study the QCD phase diagram, non-perturbatively and in great detail, is one of the many strengths of lattice QCD.

In the first chapter we defined the gauge and quark actions on the lattice to be able to take advantage of the numerical machinery of statistical mechanics, namely (Hybrid) Monte Carlo simulations. This allows us to calculate macroscopic thermodynamic objects on the lattice in terms of gauge and quark actions S_g and S_q. There are a number of ways to calculate these objects. We use the derivative method which requires the determination of anisotropy coefficients as originally defined by Karsch in 1982 [25], later known as Karsch coefficients. First I will go through a short review of why probing this area of physics is an appropriate topic of research.

2.2 Background

The standard model is used to explain the various states of matter at the subatomic level, with QCD describing the strong force. The hadrons can be studied as functions of temperature T and baryon chemical potential μ_B, which can be written in terms of the quark chemical potential μ_q using $\mu_B = N_c\mu_q$ where N_c is the number of colours in the theory and baryons are made from N_c quarks. At lower values of temperature and density there exist confined colour neutral, stable bound states made of quarks (baryons such as the proton and the neutron) and combinations of quarks and anti-quarks (mesons such as the pion and rho meson). The present knowledge of the

phases of matter is shown in the temperature/density phase diagram in Figure 2.1 below.

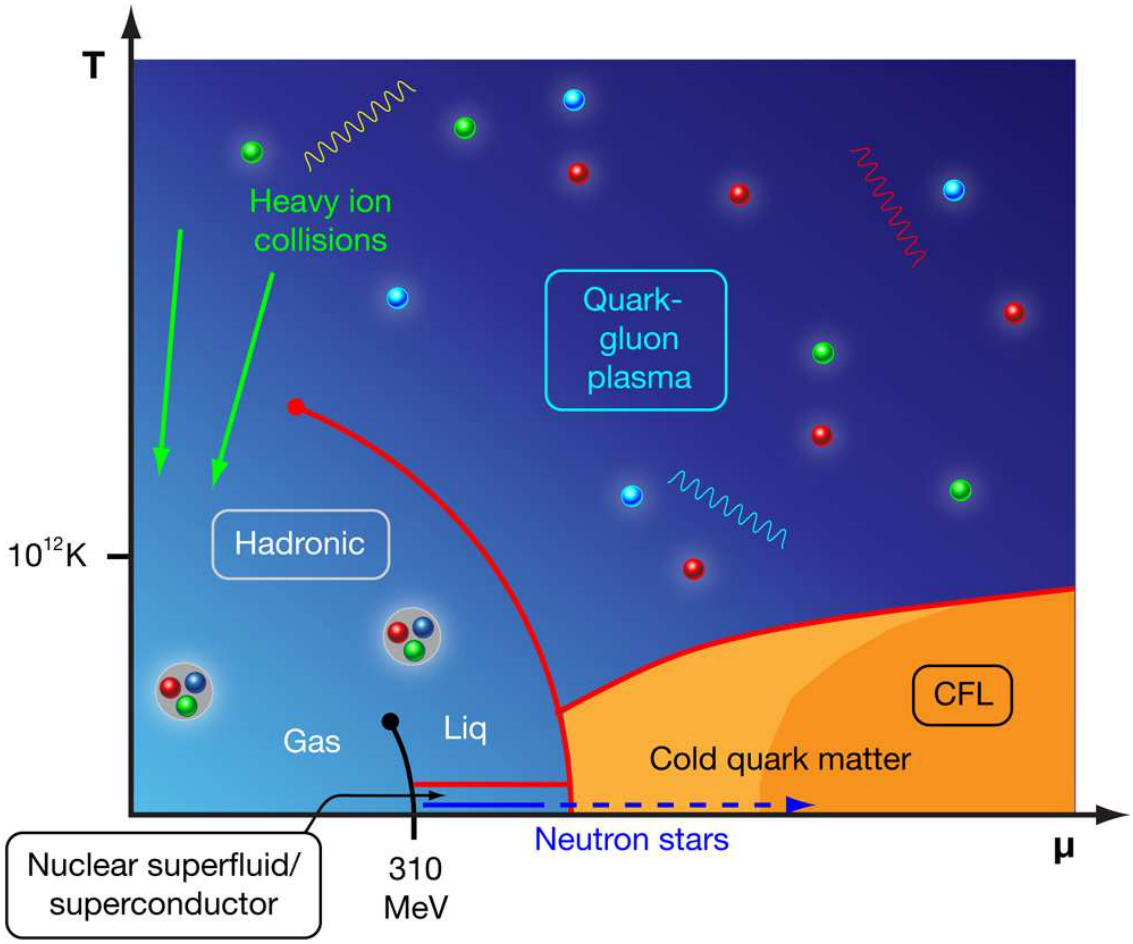

Figure 2.1: Current proposed temperature/density plot [26]. Moving along the temperature axis transforms from the confined hadronic phase to the deconfined quark gluon plasma (QGP). Moving along the chemical potential axis transforms from hadronic to colour superconducting phase to a deconfined phase (orange) to a colour flavour locked phase (CFL)(dark orange).

As the temperature and chemical potential is increased we expect there to be a transition to a deconfined phase, where the (anti-)quarks are no longer bound and they along with the gluons become the dominant degrees of freedom. The nature of the deconfined phase will depend on how hot or dense the system is and a number of exotic phases have been suggested. The exact position and order of the transitions is still in debate. Current studies suggest the hadronic phase (lower left quadrant) gives way to a quark gluon plasma (QGP, centre above and right of the hadronic phase) with increasing temperature for small to medium densities [27] [28] [29] [30].

For $\mu_q = 0$ and increasing temperature, the transition is a crossover and this is expected to be the case out as far as the critical point (shown as the solid red dot). It is expected to be first-order to the right of this, extending to the density axis. At zero or small density and large temperatures the thermal fluctuations are more dominant than the bonds or flux tubes which confine the quarks. In the strong coupling limit without matter fields, it can be shown that the heavy quark potential switches from linear confinement to Coulomb behaviour at high temperatures [29]. Including matter fields gives Yukawa potential behaviour at low temperature and Debye screening at large temperature [31]. This has been studied numerically in great detail for zero chemical potential and a range of temperatures and models.

For low temperatures and increasing density there are a number of suggested exotic phases. As we move along the density axis we enter a nuclear fluid phase at $\mu_q = \mu_0$. At higher μ_q, theory suggests a deconfined phase (orange) and then a colour-flavour-locked phase (CFL, low right of hadronic phase, dark orange). At asymptotically large chemical potential, there is a large Fermi sphere giving rise to an effect similar to Bardeen-Cooper-Schrieffer (BCS) effect seen in QED [29]. Studies using weak coupling expansion are applicable and show a colour-flavour locked region where right-helicity fermions couple with right-helicity fermions and left-helicity fermions couple with left-helicity fermions, meaning that chiral symmetry is not restored.

Of particular interest is the neutron star, which is a star which has collapsed under gravitational forces leaving a dense object of nuclear matter. The neutron star's estimated position in the phase diagram is indicated by the blue arrow at the bottom of the diagram. Some studies [32] predict a series of layers which vary from heavy nuclei near the crust, a combination of neutrons, protons and electrons at an intermediate stage and a core which might consist of quark matter. Various models have suggested the possibility that the core of the neutron star would be a deconfined phase of up and down quarks. There is also the possibility of deconfined strange quarks although they might only occur in larger neutron stars [33]. The difficulty of studying neutron stars arises as speculation on behaviour at the core is based on observations of the surface of the star. To model the densities observed in neutron stars, models or approaches such as perturbation theory, Nambu Jona-Lasinio (NJL), etc are used which may not capture the true behaviour.

Experimental evidence for these phases can be found by smashing heavy ions together and observing the output as accurately as possible in facilities such as the Relativistic Heavy Ion Collider (RHIC) at Brookhaven, New York or the Large Hadron Collider (LHC) at CERN in Geneva. Alternatively we can observe natu-

rally occurring scenarios, on quite literally an astronomical scale. The life cycle of a star realises a number of different scenarios at a broad range of temperatures and densities. While black holes have been studied in relation to gravitational effects, neutron stars are the appropriate area to study high density effects. Here, it is believed that the degrees of freedom will switch from the hadrons to the quarks. To study these phenomena properly we need a first principles, modern approach built on years of statistical mechanics.

The equation of state (EoS) gives inputs to the Tolman Oppenheimer Volkoff (TOV) equation [34] [35] which allows for a description of the neutron star giving estimates for the mass and ratio. First principles perturbative calculations can be done at non-zero chemical potential, but only at prohibitively large values, $\mu_q \sim 10^8$MeV. The interior of a neutron star is expected to correspond to chemical density of the order of a few hundred MeV [29]. In principle, it is an area which should be studied using lattice QCD, but there is a problem. As mentioned earlier, typical lattice QCD simulations use importance sampling to limit the cost of numerical simulations but introducing non-zero chemical potential spoils this.

2.3 Statistical Mechanics

At zero density, the thermal expectation of any observable A can be written as [36]

$$\langle A \rangle = \frac{1}{Z(\beta)} \mathrm{Tr}\left(e^{-\beta H} A\right), \tag{2.1}$$

where $Z(\beta) = \mathrm{Tr}\left(e^{-\beta H}\right) = \int D[\phi]\, e^{-S}$ where ϕ is periodic in the temporal direction and the action S defined as $S = \int_0^\beta dx_4 \int d^3x \mathcal{L}$ where $\mathcal{L}$ is the Lagrangian. The action S containing both the quark and gauge sector is real and bounded from below for chemical potential $\mu_q = 0$, which is the basis for the majority of lattice studies. If we now consider the partition function Z in terms of continuum quark and gauge action allowing for a non-zero chemical potential we get an additional factor:

$$Z = \mathrm{Tr}\left[\mathrm{e}^{(-H-\mu_i Q_i)}\right], \tag{2.2}$$

with

$$Q_i = \int d^3x \bar{\psi}\left(x\right)\gamma_0\psi\left(x\right) = \int d^3x \psi^\dagger\left(x\right)\psi\left(x\right), \tag{2.3}$$

where Q_i is the baryon number for flavour i, where μ_i is the relevant chemical potential for that flavour. At first glance the partition function on the lattice looks the same as for zero chemical potential, as the μ_q dependent term are hidden in S_f

$$Z = \int \left(\mathrm{D}U\mathrm{D}\bar{\psi}\mathrm{D}\psi\right) e^{-\beta S_g[U]} e^{-S_f\left[U,\bar{\psi},\psi\right]} = \int \left(\mathrm{D}U\right) e^{-\beta S_g[U]} \det M\left[U\right], \tag{2.4}$$

where the quark action can be written in terms of the fermion matrix, $S_q = \bar{\psi}M\psi$. After integrating out the fermions, the determinant term contains the effects the quark terms have on the gauge fields including the chemical potential terms. On an isotropic lattice we define the chemical potential in terms of a dimensionless variable $\mu = \mu_q a$. If we look carefully at the effect that non-zero chemical potential has on the action S, we gain a term in the fermion matrix

$$M = \not{D} + m + \mu\gamma_0, \tag{2.5}$$

where $\not{D}$ satisfies γ_5 hermiticity, so $\gamma_5\not{D}\gamma_5 = \not{D}^\dagger$. In general (including SU (2) and SU (3)), we see that

$$\gamma_5\left(\not{D} + m + \mu\gamma_0\right)\gamma_5 = \not{D}^\dagger + m - \mu\gamma_0 = \left(\not{D} + m - \mu^*\gamma_0\right)^\dagger, \tag{2.6}$$

which then means that the determinant is

$$\det\left(\not{D} + m + \mu\gamma_0\right) = \det\left(\not{D}^\dagger + m - \mu\gamma_0\right) = \det[(\not{D} + m - \mu^*\gamma_0)^\dagger]. \tag{2.7}$$

For real non-zero μ, the quark determinant becomes complex, which in turn causes the Boltzmann factor e^{-S} to become complex, and it therefore can no longer be interpreted as a probability. This problem is known as the sign problem and does not only affect lattice QCD. It is also known to occur in a number of models in

condensed matter physics, so any significant breakthrough would impact on several areas of research.

2.4 The Chemical Potential conundrum

When non-zero density was initially simulated on the lattice, the formulation was rather naive and caused divergences [37]. In the Euclidean formulation of thermodynamics, the chemical potential behaves as the fourth (temporal) component of an imaginary, constant vector potential. Interpreting the μ_q dependent term as an alteration to the gauge field rather than a separate term solved this problem. On the lattice this becomes an extra term in the quark action acting on the temporal term.

$$U_\mu \to e^{\mu_q \tau} U_\mu, \qquad U_\mu^\dagger \to e^{-\mu_q \tau} U_\mu^\dagger. \tag{2.8}$$

The sign problem is not an issue for the physical theory, rather a computational one related to the use of importance sampling and the formulation in terms of the determinant. There is a number of possible alternative methods to solve, avoid or limit this problem. Below I will briefly discuss the popular methods.

The most obvious of the alternative methods is to simulate using a complex chemical potential where $\mu_I = bi$, where $b \in \mathbb{R}$, as this then satisfies $-\mu_I^* = \mu_I$. To recover "physical" results analytic continuation is performed which tends to give reasonable results, but only if there are no singularities. As the chemical potential term is now a complex phase, there is a restriction placed on μ_I as it is now periodic in T [38], [39], [40].

The next option is to use the absolute value of the determinant as the probability weight and move the phase back into the probability function part mentioned earlier when we covered importance sampling (see equations (1.41) - (1.42)), but in practice this phase can be rather large and can cause large errors. Re-weighting the determinant this way means you are no longer importance sampling. This means that the space you are sampling may match up poorly with the correct space which can lead to an overlap problem. In theory this works for all μ_q, but in practice for small quark masses especially, it can lead to incorrect results [41], [42], [43].

A less extreme version of this is the density of states method. This amounts to fixing a parameter, which adds an extra integration with respect to this fixed parameter in order to measure an observable [44], [45], [46]. This can be then used in the probability weight, effectively dividing the problem. If we use the plaquette as this fixed parameter, the extra integration becomes parameter independent and this particular method is known as the factorisation method. The point of this is to be able to discern areas where the largest fluctuations occur and avoid them.

Focussing on the chemical potential term also provides a number of possible alternatives. Expansion of the determinant using the canonical formulation, which results in an expression in terms of terms of a μ dependent exponential and a canonical determinant. As μ couples to the temporal link variables, analytically calculating the temporal part of the determinant reduces the μ dependence of link variables. The computational cost is large and only high temperature configuration sets, which have a small number of points in the temporal direction, have been studied so far [47], [48]. It is possible to Taylor expand around $\mu = 0$, which in principle only works for rather small μ and only if there are no singularities [41], [49].

Next is changing the integration measure. Redefining the integration measure to avoid any measure that gives a sign problem using saddle point integration [50] is known as the Lefschetz thimble. It is also possible, under certain conditions at large gauge coupling, to use cluster methods. The volume which the integration measure is over can be subdivided into volumes containing a number of fermions whose behaviour cancels out, for example the fermion bag model [51].

As the sign problem is a feature of Hybrid Monte Carlo, switching to a method which uses complex probabilites can avoid the sign problem. The most promising is Langevin dynamics which allows for stochastic quantisation [52], [53]. This would be a move away from importance sampling and the use of a real valued function as a probability. It would effectively use a complex valued probability function and although results so far look good, this method has a large computational cost and there are questions about convergence to the wrong results.

Alternatively, it is possible to simulate with two flavours with opposing chemical potentials [54], that is, introduce an isospin chemical potential $\mu_{iso} = \mu_u = -\mu_d$, which will satisfy equation [2.7]. Isospin is not conserved in the real world due to weak interactions but this method does allow for some studies of finite chemical potential behaviour [55] [56].

The other possibility is to avoid the sign problem completely by simulating a QCD-like theory. For example, the gauge group can be changed from SU (3) to SU (2) which is the method we used in this study. This reduces the theory to two colours and with the further restriction of simulating an even number of flavours, the determinant is positive definite for non-zero chemical potential μ and there is no sign problem [57], [58], [59]. This relies on the fact that SU (2) is a pseudo-real group and is proven in detail in [60].

From experimental data, it has been accepted that the strong nuclear force is mediated by the gluons, and comes in three "colours". It is described using the gauge group SU (3). Studying aspects of QCD by modifying the theory can also give important results about the structure and topology of the Standard model while also surveying the computational cost of each part. For example, simulating Yang-Mills theory is much cheaper due to the lack of quarks, and the absence of quarks can give an indication of what behaviour is caused by them.

Lattice QCD allows for simulation of a subset of real QCD, depending on which masses are of interest. It also allows for studies of "toy" models such as the Ising model or σ model in various numbers of dimensions d. These provide easier testing grounds, although they don't replicate the richness of QCD. Changing the group or fermion representation so as to get qualitative agreement with experiment and avoid the sign problem, allows for a full study of the $T - \mu_q$ phase diagram, albeit in a theory that differs from real QCD. Some candidate groups like G (2), [61], [62] and SU (2) exhibit the same characteristic traits such as confinement and asymptotic freedom. This allows for research in a neighbouring area, two colour physics, without restrictions coming from the density. This may give valuable information regarding unforeseen issues which the inclusion of a chemical potential term might cause along with providing a first principles check for many alternative models and approaches. While perturbation theory studies are not suitable for intermediate values of temperature and density at reasonable values of the gauge coupling, they can be useful as a guide of possible behaviour in limiting scenarios.

2.5 $\mathrm{QC_2D}$

Two colour QCD or $\mathrm{QC_2D}$ is a similar theory to real QCD except that the gauge group is now SU (2) instead of SU (3), which allows for calculations at non-zero chemical potential μ_q using the regular numerical machinery of Hybrid Monte Carlo.

Naturally this means the theory does not have the same properties as full QCD. Confinement and asymptotic freedom are present but having two colours affects the baryon definition. The meson structure remains quark-antiquark, but the baryons become quark-quark bound states or diquarks, with antiquark-antiquark antiparticle states. At zero chemical potential, the Pauli-Gürsey symmetry implies the baryons/diquarks are degenerate with the mesons as well as the antibaryons [58]. When chemical potential is turned on they are distinguishable. In the chiral limit for two flavours, spontaneous symmetry breaking leads to five massless Nambu-Goldstone bosons. These are the three pions, the diquark and the antidiquark.

This raises another unique possibility of study, namely the diquarks. In modeling the formation of hadrons in real QCD, the diquarks might be an intermediate step leading to a diquark-quark bound state for baryons. While in real QCD they are not seen as particles as they are not colour neutral states, in QC_2D they are colour singlets, so it is perfectly acceptable to label them as diquark particles in this theory and they can be studied in terms of the formation of the diquark condensate for increasing chemical potential.

For real QCD a superconducting phase (CFL phase) is predicted [29]. In this section of the $T - \mu_q$ phase diagram, the force confining the quarks is no longer completely dominant. When the quarks are light compared to the chemical potential, it is thought that a Bardeen-Cooper-Schrieffer (BCS) effect will cause a breaking of global (axial SU (3) and baryon U (1) symmetries) and local colour symmetries resulting in colour-flavour-locking. In QC_2D, as the diquarks condense at increasing chemical potential, there exists a superfluid phase [63] in place of the superconducting phase seen in real QCD, due to the colour neutral diquarks.

The study of a range of values of quark chemical potential μ_q should give us more information about the possible states of matter. In QC_2D, there are a few theorised states of matter. As the chemical potential μ_q is increased, we reach the onset of non-zero baryon density at $\mu_o \approx \frac{m_\pi}{2}$, coming from the expectation that $\mu_o \approx \frac{1}{N_{colour}} m_{nucleon}$. Beyond this point is a dilute Bose gas formed from diquark bound states which form at the onset chemical potential, i.e. $\mu_B > \mu_{B_0} = M_\pi$ and diquark condensate $\langle qq \rangle \neq 0$. This exists up to μ_Q where a "quarkyonic" phase may occur[64], where the quarks are degenerate but confined and chirally symmetric. This phase lasts up until μ_D, which is the beginning of the deconfined phase.

The variety of suggested phases gives an opportunity for a non-perturbative study to determine the position and order of these phases as a function of temperature and

chemical potential. In our project a diquark source j is added to regularise infra-red (IR) fluctuations in the superfluid phase. Although QC_2D is QCD-like, it allows for qualitative predictions of physical behaviour with increasing density.

2.6 Thermodynamic Quantities

As we now have an established link between lattice field theory and statistical mechanics we can look at thermodynamic quantities that are calculated on the lattice. We already have a method in place to write the path integral of the partition function Z on the lattice in terms of the action $S = S_q + S_g$ which consists of the quark and gauge actions, where the $\mathrm{SU}(N)$ dependence is included in these actions, so the following discussion describes N colour lattice QCD with degenerate quarks at the thermodynamic limit, $V \to \infty$. We will now look at the energy density ε and pressure p in terms of the action S.

As we plan on studying a system with non-zero chemical potential, using the grand canonical ensemble is appropriate. From thermodynamics, we can define the grand potential:

$$\Omega = -T \ln Z = E - TVs - \mu_q N_q = -pV, \tag{2.9}$$

where μ_q is the chemical potential, and the entropy density s and quark number density n_q are defined as:

$$s = \frac{1}{V}\left(\frac{\partial\left(T \ln Z\right)}{\partial T}\right)\bigg|_{V,\mu_q}, \qquad n_q = \frac{N_q}{V} = \frac{T}{V}\,\frac{\partial \ln Z}{\partial \mu_q}\bigg|_{T,V}. \tag{2.10}$$

We can rewrite functions of Z in terms of the action by using $-T\ln Z = S = S_g + S_q$, where S_q now contains exponential terms of chemical potential as explained in (2.4). Using equations (2.9) and (2.10), the energy density can be derived by:

$$\begin{aligned}\varepsilon = \frac{E}{V} &= \frac{T}{V}\left(\frac{\partial\left(T \ln Z\right)}{\partial T}\right)\bigg|_{V,\mu_q} - \frac{T}{V}\ln Z + \mu_q n_q \\ &= -\frac{T^2}{V}\left(\frac{\partial S}{\partial T}\right)\bigg|_{V,\mu_q} + \mu_q n_q,\end{aligned} \tag{2.11}$$

where S is the combined gauge and quark action. For the pressure:

$$p = T \left(\frac{\partial \ln Z}{\partial V} \right) \Bigg|_{T,\mu_q} = -T \left(\frac{\partial S}{\partial V} \right) \Bigg|_{T,\mu_q} . \tag{2.12}$$

The chemical potential is defined on an anisotropic lattice as $\mu = \mu_q a_t = \frac{\mu_q a_s}{\xi}$. Although we will use isotropic lattices as sample points, the derivatives with respect to volume and temperature are handled by anisotropic lattices in the Karsch coefficient determination. Later in this chapter I will reformulate the macroscopic derivative $f(V, T, \mu_q)$ in terms of the microscopic derivatives $f(a_s, \xi, \mu)$ which gives access to lattice parameters.

Many calculations of physical observables on the lattice include ultraviolet divergences. The effect of these divergences is eliminated by evaluating the observable at the temperature in question and performing a vacuum subtraction, which on the lattice amounts to subtracting the same observable evaluated on the coldest lattice simulated which is closest to $T = 0$ at $\mu_q = 0$.

The derivatives in equations (2.11) and (2.12) immediately raise a problem for finite simulations on a lattice: a discrete derivative with respect to volume or temperature requires multiple configuration samples for a spread of temperatures and volumes while holding other parameters fixed. The introduction of anisotropic lattices allows for these necessary comparisons.

The temperature on the lattice is defined by $T = \frac{1}{N_t a_t}$, where for isotropic lattices $a_s = a_t = a$, so to decrease the temperature on an isotropic lattice means either increasing the lattice spacing while holding N_t constant (fixed-N_t approach), or increasing the number of points in the temporal direction N_t while holding the lattice spacing constant (fixed-scale approach). The choice between fixed scale and fixed-N_t mostly depends on the temperature of interest, and the particular object of interest.

The fixed scale method only needs one set of vacuum configurations as the dependence is on the lattice spacing. As well as a reduced computational cost, it guarantees that we are working along a line of constant physics. The disadvantage is that a careful choice of lattice spacing must be made to begin with, otherwise it may limit the range of temperatures or the usefulness of the data generated over just a handful of points. This also results in a discrete set of temperatures. This affects

high temperature configuration sets due to the small number of points involved in the temporal direction, giving rise to lattice artifacts.

For fixed-N_t, each choice of lattice spacing which corresponds to each temperature simulated requires a set of vacuum configurations, so there is an immediate additional computational cost. There is also a danger that the physics generated on one set won't match in with the next set, as it is harder to guarantee that they exist on the same or equivalent line of physics. At low temperature the effects of lattice artifacts may be seen as the lattice spacing grows larger. To calculate the energy density and pressure on the lattice requires a method to handle the derivative terms. This is done using one of the following methods.

The Derivative method:

The thermodynamic equations are given in terms of derivatives and early attempts tried to solve these equations by approximating the derivative terms perturbatively. When the derivatives are carried through the particular action of choice, they become derivatives of input parameters with respect to the action dependencies. For example, for the unimproved anisotropic Wilson gauge action:

$$S_G = -\frac{\beta}{N_C}\left[\frac{1}{\gamma_g}\sum_{x,i<j}\mathrm{ReTr}U_{ij}\left(x\right) + \gamma_g\sum_{x,i}\mathrm{ReTr}U_{i0}\left(x\right)\right], \tag{2.13}$$

where $U_{ij}\left(x\right)$ are the spatial plaquettes and $U_{i0}\left(x\right)$ are the temporal plaquettes, and γ_g is the gauge anisotropy. The derivative with respect to the volume returns:

$$\begin{aligned}\frac{\partial S_G}{\partial V} = -\frac{\beta}{N_C}\Bigg[&\left\{\frac{1}{\beta}\frac{\partial\beta}{\partial V} - \frac{1}{\gamma_g}\frac{\partial\gamma_g}{\partial V}\right\}\frac{1}{\gamma_g}\sum_{x,i<j}\mathrm{ReTr}U_{ij}\left(x\right)\\ &+\left\{\frac{1}{\beta}\frac{\partial\beta}{\partial V} + \frac{1}{\gamma_g}\frac{\partial\gamma_g}{\partial V}\right\}\gamma_g\sum_{x,i}\mathrm{ReTr}U_{i0}\left(x\right)\Bigg].\end{aligned} \tag{2.14}$$

In practice it makes more sense to write these derivatives in terms of the lattice spacing which we will do at the end of this section. In the early calculations, these terms were determined perturbatively by Karsch [25], after which these derivatives became known as the Karsch coefficients. One immediate problem with the early calculations was that they resulted in a negative pressure and a non-vanishing pressure gap [65] at the deconfining transition in SU (3) gauge theory. As this transition is first order the phases coexist, which means the pressures in the different phases

are the same near the transition line. The energy density on the other hand is different due to latent heat. The perturbative determination had failed to accurately capture their behaviour and at that stage a non-perturbative calculation would be too costly, and so the search for a more reasonable approach led to the popular use of the integral method which I will discuss in section 2.6.

The Karsch coefficients may also be calculated non-perturbatively by studying the parameter behaviour on a number of configuration sets in the vicinity of the central set of interest. The derivatives with respect to the lattice spacing are also needed, which is calculated anyway as part of the Karsch coefficient determination. So for a new study of brand new configurations with a new set of parameters the computational cost of the derivative method already includes the beta function calculation. Tuning anisotropy parameters gives much of the required information.

In the fixed scale regime, as mentioned above, the input parameters don't vary and the volume and temperature are altered by changing N_s and N_t. The Karsch coefficients become constants which once determined can be used to renormalise the energy density and pressure for several volumes. This means that once a central set of parameters is chosen and the Karsch coefficients have been found to satisfactory precision, we can then view the sets on which the thermodynamic quantities are measured as an independent problem although generated at the same settings of the input parameters as those of the central set. Increasing statistics at a later date by generating more configurations can then focus on where the emerging areas of interest occur.

Instead of using macroscopic quantities, we now switch to the microscopic counterparts using $T = \frac{1}{N_t a_t}$, $V = N_s^3 a_s^3$ and $\mu = \frac{\mu_q a_s}{\xi}$. We then switch the temporal lattice spacing a_t for the anisotropy $\xi = \frac{a_s}{a_t}$ to distinguish between anisotropic and isotropic lattices, and which we will measure on the lattice. We use the following relations:

$$a_s = \frac{V^{\frac{1}{3}}}{N_s} \Rightarrow \left.\frac{\partial a_s}{\partial V}\right|_{T,\mu_q} = \frac{a_s}{3V}, \tag{2.15}$$

$$a_t = \frac{1}{N_t T} \Rightarrow \left.\frac{\partial a_t}{\partial T}\right|_{V,\mu_q} = -\frac{a_t}{T} \tag{2.16}$$

$$\xi = \frac{a_s}{a_t} \Rightarrow \left.\frac{\partial \xi}{\partial a_s}\right|_{a_t,\mu} = \frac{1}{a_t}, \quad \left.\frac{\partial \xi}{\partial a_t}\right|_{a_s,\mu} = -\frac{\xi}{a_t}, \tag{2.17}$$

$$\mu = \frac{\mu_q a_s}{\xi} \Rightarrow \left.\frac{\partial \mu}{\partial \xi}\right|_{a_s,\mu_q} = -\frac{\mu}{\xi}, \quad \left.\frac{\partial \mu}{\partial a_s}\right|_{\xi,\mu_q} = \frac{\mu}{a_s}, \tag{2.18}$$

and make repeated use of the following equation:

$$\left.\frac{\partial f}{\partial a}\right|_{b,c} = \left.\frac{\partial f}{\partial u}\right|_{v,w} \left.\frac{\partial u}{\partial a}\right|_{b,c} + \left.\frac{\partial f}{\partial v}\right|_{u,w} \left.\frac{\partial v}{\partial a}\right|_{b,c} + \left.\frac{\partial f}{\partial w}\right|_{u,v} \left.\frac{\partial w}{\partial a}\right|_{b,c}. \tag{2.19}$$

For the volume derivative this gives us

$$\left.\frac{\partial}{\partial V}\right|_{T,\mu_q} = \left.\frac{\partial}{\partial \xi}\right|_{a_s,\mu} \left.\frac{\partial \xi}{\partial V}\right|_{T,\mu_q} + \left.\frac{\partial}{\partial a_s}\right|_{\xi,\mu} \left.\frac{\partial a_s}{\partial V}\right|_{T,\mu_q} + \left.\frac{\partial}{\partial \mu}\right|_{\xi,a_s} \left.\frac{\partial \mu}{\partial V}\right|_{T,\mu_q}, \tag{2.20}$$

$$\left.\frac{\partial \xi}{\partial V}\right|_{T,\mu_q} = \left.\frac{\partial \xi}{\partial a_s}\right|_{a_t,\mu} \left.\frac{\partial a_s}{\partial V}\right|_{T,\mu_q} + \left.\frac{\partial \xi}{\partial a_t}\right|_{a_s,\mu} \cancelto{0}{\left.\frac{\partial a_t}{\partial V}\right|_{T,\mu_q}}, \tag{2.21}$$

$$\left.\frac{\partial \mu}{\partial V}\right|_{T,\mu_q} = \left.\frac{\partial \mu}{\partial a_s}\right|_{\xi,\mu_q} \left.\frac{\partial a_s}{\partial V}\right|_{T,\mu_q} + \left.\frac{\partial \mu}{\partial \xi}\right|_{a_s,\mu_q} \left.\frac{\partial \xi}{\partial V}\right|_{T,\mu_q} \tag{2.22}$$

$$= \frac{\mu}{a_s}\frac{a_s}{3V} - \frac{\mu}{\xi}\frac{1}{a_t}\frac{a_s}{3V} = 0. \tag{2.23}$$

The two terms in equation (2.23) cancel giving the volume derivative:

$$\left.\frac{\partial}{\partial V}\right|_{T,\mu_q} = \frac{1}{3V}\left(\xi \left.\frac{\partial}{\partial \xi}\right|_{a_s,\mu} + a_s \left.\frac{\partial}{\partial a_s}\right|_{\xi,\mu}\right) \tag{2.24}$$

For the temperature derivative we get:

$$\left.\frac{\partial}{\partial T}\right|_{V,\mu_q} = \left.\frac{\partial}{\partial \xi}\right|_{a_s,\mu} \left.\frac{\partial \xi}{\partial T}\right|_{V,\mu_q} + \left.\frac{\partial}{\partial \mu}\right|_{a_s,\xi} \left.\frac{\partial \mu}{\partial T}\right|_{V,\mu_q}, \tag{2.25}$$

$$\left.\frac{\partial \xi}{\partial T}\right|_{V,\mu_q} = \left.\frac{\partial \xi}{\partial a_t}\right|_{a_s,\mu} \left.\frac{\partial a_t}{\partial T}\right|_{V,\mu_q} + \left.\frac{\partial \xi}{\partial a_s}\right|_{a_t,\mu} \cancelto{0}{\left.\frac{\partial a_s}{\partial T}\right|_{V,\mu_q}}, \tag{2.26}$$

$$\left.\frac{\partial \mu}{\partial T}\right|_{V,\mu_q} = \left.\frac{\partial \mu}{\partial \xi}\right|_{a_s,\mu_q} \left.\frac{\partial \xi}{\partial T}\right|_{V,\mu_q}, \tag{2.27}$$

which gives

$$\left.\frac{\partial}{\partial T}\right|_{V,\mu_q} = \frac{\xi}{T}\left.\frac{\partial}{\partial \xi}\right|_{a_s.\mu} - \frac{\mu}{T}\left.\frac{\partial}{\partial \mu}\right|_{a_s,\xi}. \tag{2.28}$$

The quark density term gives:

$$\left.\frac{\partial}{\partial \mu_q}\right|_{V,T} = \left.\frac{\partial}{\partial \mu}\right|_{a_s,\xi} \left.\frac{\partial \mu}{\partial \mu_q}\right|_{V,T}, \tag{2.29}$$

$$\left.\frac{\partial \mu}{\partial \mu_q}\right|_{V,T} = \left.\frac{\partial \mu}{\partial \mu_q}\right|_{a_s,T} \left.\frac{\partial \mu_q}{\partial \mu_q}\right|_{V,T}, \tag{2.30}$$

giving

$$\left.\frac{\partial}{\partial \mu_q}\right|_{V,T} = \frac{\mu}{\mu_q} \left.\frac{\partial}{\partial \mu}\right|_{a_s,\xi}. \tag{2.31}$$

$$n_q = -\frac{T}{V} \left.\frac{\partial S}{\partial \mu_q}\right|_{V,T} = -\frac{T}{V}\frac{\mu}{\mu_q} \left.\frac{\partial S}{\partial \mu}\right|_{a_s,\xi} \tag{2.32}$$

Equations (2.28) and (2.32) are used to rewrite the energy density in terms of derivatives of the gauge and fermion action:

$$\varepsilon = \frac{T^2}{V} \left(\frac{\partial (\ln Z)}{\partial T}\right)\Bigg|_{V,\mu_q} + \mu_q n_q = -\frac{T}{V} \left(\xi \left.\frac{\partial S_g}{\partial \xi}\right|_{a_s.\mu} + \xi \left.\frac{\partial S_q}{\partial \xi}\right|_{a_s.\mu}\right). \tag{2.33}$$

Using equation (2.24), the pressure can be written in terms of derivatives of the gauge and fermion action:

$$\begin{aligned} p &= T \left(\frac{\partial (\ln Z)}{\partial V}\right)\Bigg|_{T,\mu_q} \\ &= -\frac{T}{3V} \left(\xi \left.\frac{\partial S_g}{\partial \xi}\right|_{a_s,\mu} + \xi \left.\frac{\partial S_q}{\partial \xi}\right|_{a_s,\mu} + a_s \left.\frac{\partial S_g}{\partial a_s}\right|_{\xi,\mu} + a_s \left.\frac{\partial S_q}{\partial a_s}\right|_{\xi,\mu}\right), \end{aligned} \tag{2.34}$$

We now have the energy density and pressure in a form which we can numerically determine. Selecting a central set of parameters, we can surround this with sets which vary the anisotropy and lattice spacing and measure the derivatives. These are then used on all sets which lie along the same line of physics as the central set.

In conformal field theory and scale invariant theories, the trace of the energy-momentum tensor is zero. This trace condition is generally broken by quantum

corrections and is known as the trace anomaly. It is defined as:

$$\mathrm{Tr}\,(T^{\mu\nu}) = \varepsilon - 3p = \frac{T}{V}\left(a_s \left.\frac{\partial S_g}{\partial a_s}\right|_{\xi,\mu} + a_s \left.\frac{\partial S_q}{\partial a_s}\right|_{\xi,\mu} \right). \tag{2.35}$$

This allows us to also study the trace anomaly for a dynamical system. For a relativistic Bose gas the trace of the momentum energy tensor T gives zero. But with massive quarks $\mathrm{Tr}\,(T) = \sum T_{\nu\nu} = \epsilon - 3p \neq 0$. It is also very useful on the lattice as it contains information about the energy density and pressure, yet has no derivatives with respect to the anisotropy, relying only on the β function, $a_s \frac{\partial S}{\partial a_s}$. This enables it to be used in the following alternative approach to the derivative method.

The Integral method:

This was initially developed for a pure gauge system, where the parameter space is one dimensional. For two or more dimensions, the integral is no longer unique. By combining the definitions for the energy density and pressure and using a few thermodynamic identities we can avoid having to determine the Karsch coefficients, although we would still need the β function which requires a numerical determination. There are two versions of the method, the plain integral method (fixed N_t) and the temperature integral method or T-integral method (fixed scale).

If we combine the definitions for the energy density and pressure [66] we get a formula for the trace anomaly

$$I = \epsilon - 3p = -\frac{T}{V}\frac{\partial \ln \mathcal{Z}}{\partial \ln a}. \tag{2.36}$$

The pressure can be determined in the thermodynamic limit using

$$\ln Z = -\frac{pV}{T} \tag{2.37}$$

which allows us to write I as

$$I = \frac{T}{V}\frac{d\left(p\frac{V}{T}\right)}{d\ln a}, \tag{2.38}$$

and from this we can integrate to get

$$p\left(a\right)a^{4}-p\left(a_{0}\right)a_{0}^{4}=-\int_{\ln a_{0}}^{\ln a}\triangle I\left(a'\right)\left(a'\right)^{4}d\ln a', \tag{2.39}$$

where $\triangle I = I\left(T\right) - I\left(0\right)$ and a_0 is the larger lattice spacing which corresponds to the lower temperature. We can then get the energy density by combining the integration measure I and the pressure using $\epsilon = I + 3p$.

Incorporating the fixed scale approach gives the T-integral method, which may introduce lattice artifacts at higher temperatures. It is better suited to lower temperature studies including the critical temperature T_c. For this the pressure is derived from the trace anomaly using

$$\frac{p}{T^{4}}=\int_{T_{0}}^{T}dT\frac{\epsilon-3p}{T^{5}}, \tag{2.40}$$

which is derived from the thermodynamic relation

$$T\frac{\partial}{\partial T}\left(\frac{p}{T^{4}}\right)=\frac{\epsilon-3p}{T^{4}}, \tag{2.41}$$

which is valid for vanishing chemical potential [67].

For non-vanishing chemical potential, the pressure can be calculated by integrating any thermodynamic quantity over an appropriate contour. From the definition of the grand potential (2.9), we can write the pressure in terms of $p = -\frac{T}{V}\ln Z$. If we integrate over one of the other derivatives of the grand partition function given in (2.10), we can get the pressure. In our paper [68], we integrate the quark number density over the chemical potential:

$$p=\int_{\mu_{0}}^{\mu}n_{q}d\mu, \tag{2.42}$$

choosing μ_0 such that $p\left(\mu_0\right) \approx 0$. We will compare this result with the derivative method result in chapter 5. The integral method and derivative method are known to not agree due to differing cut-off dependences [69]. The derivative method as well as being an alternative, also allows for a consistency check with the integral method. In the continuum limit they are expected to converge.

2.7 Phase transitions

One area which lattice QCD actively probes is that of the phase transition. There are a number of these including the confined-deconfined phase transition and the theorised restoration of chiral symmetry. There are others in various models depending on gauge group [70]. Besides finding the phase transition we want to know what order the phase transition is and which order parameters signal the onset of a transition. The dependence on the mass, density and temperature remain a main focus of lattice studies. Below is the standard Columbia plot (left) [71] and a projected three dimensional plot in μ (right) [72].

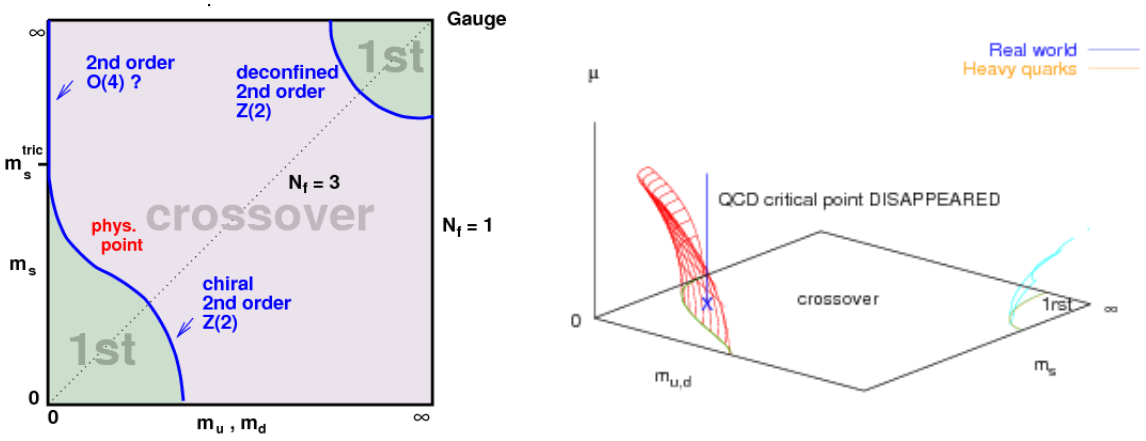

Figure 2.2: Columbia plot and a projection of possible behaviour for non-zero chemical potential.

First we discuss the Columbia plot which is at zero chemical potential. The strange quark mass is along the vertical axis, and the common light quark mass $m_q = m_u = m_d$ is along the horizontal axis. For three massless quarks (bottom left), theory suggests that as we increase temperature, there is a first order transition between the hadronic and quark gluon plasma. For two massless quarks, and infinite strange quark mass (top left), we expect the transition to be second order and reside in the $O(4)$ universality class. Starting now from the bottom left corner and moving along the diagonal we expect the first-order phase to give way to a crossover which is seen to occur in simulations. Current data suggest real QCD lies in the crossover region. If we then continue to the top right corner for large quark masses, we get a fully quenched theory and it returns to a first-order transition.

If we then increase chemical potential μ, we get the second plot which is a projection of the expected behaviour of the first-order/crossover transition from the Columbia plot. The nature of this curvature and the sensitivity to the number of quarks and

their respective masses is an area which lattice QCD should be able to map in the near future. In the case of two colour physics, a mapping of the phase diagram for a range of temperatures and densities could be very helpful.

For a phase transition there is a singularity in $Z(T, \mu, m, H)$, although on the lattice there is a finite volume V, which does not give singularities, so no phase transitions. Singularities are only seen in the infinite volume limit. Looking at the behaviour of an order parameter over a range of parameters allows us to close in on the position of the phase transition in question, for example:

- The Chiral condensate:

At high temperature, there exists a chiral symmetry restoring phase transition, at zero u and d masses. The chiral condensate is defined [73] by:

$$\left\langle \bar{\psi}\psi_f \right\rangle = \frac{T}{V}\frac{\partial \ln \mathcal{Z}}{\partial m_f}, \tag{2.43}$$

and in the massless quark limit $m_q = 0$, $(N_f \geq 2)$ equals zero when chiral symmetry is present, which occurs at large temperatures. At low temperature chiral symmetry is broken giving a non-zero value for the chiral condensate. The onset in chiral symmetry breaking is seen as a sharp rise in the chiral susceptibility which is defined [66] as:

$$\chi_{ij}^{chiral} = \frac{T}{V}\frac{\partial^2 \ln \mathcal{Z}}{\partial m_i \partial m_j} \tag{2.44}$$

At the deconfinement transition there is a jump in the chiral susceptibility while for the chiral transition in SU (3), there is a peak in the quark number susceptibility which is given [66] by:

$$\chi_{ij}^{quark} = \langle N_i N_j / V \rangle = \frac{T}{V}\frac{\partial^2 \ln \mathcal{Z}}{\partial \mu_i \partial \mu_j}. \tag{2.45}$$

- The Polyakov loop:

SU (N) gauge theories have a global Z (N) invariance coming from the group centre. The Polyakov loop $\langle L \rangle$ is built with from the product of time-like gauge-link matrices:

$$L = \sum_{\vec{x}} \mathrm{Tr} \left(\prod_{\tau=1}^{N_\tau} U_4 (\vec{x}, \tau) \right). \tag{2.46}$$

It is related to the measurement of the change in free energy in an ensemble after adding a static quark [66]:

$$L\left(a,T\right)=\exp\left[-F_{L}\left(a,T\right)/T\right] \tag{2.47}$$

There is an exact symmetry for $m_q = \infty$ (pure gauge). $\langle L \rangle$ is non-zero in the deconfined phase but at finite mass L no longer vanishes, but becomes proportional to the exponential of minus the smallest hadron mass M, $L \sim \exp\left(-M/T\right)$. This object relies on the centre symmetry as defined in chapter 1. At high temperature, there is a deconfining phase transition in the infinite quark mass limit $m_q = \infty$, $(N_f = 0)$. At finite quark mass both the chiral condensate and polyakov loop are indicators rather than order parameters.

3 Determination of Karsch Coefficients

3.1 Overview

This chapter contains the main project of this thesis, namely to calculate the Karsch coefficients. These allow for the correct renormalisation of the energy density which I will discuss in chapter 5. This work was part of a larger study on two colour QCD and the early results were published in [68]. As well as the energy density, the Karsch coefficients allow for calculation of the trace anomaly which relies on the β function, and the pressure, although in the paper mentioned we used the integral method. Having covered what the Karsch coefficients are in the previous chapter, I will here focus on how they are calculated, discuss possible sources of error and look at the results coming from the measurements of the lattice spacing a_s, the quark and gauge anisotropies ξ_q and ξ_g, and the mass ratio M. First I will detail the project outline:

Given several sets of isotropic and anisotropic Wilson fermion configurations generated at zero temperature and density, of varying input parameters β, hopping parameter κ, gauge anisotropy γ_g and quark anisotropy γ_q, measure the spatial lattice spacing a_s, the pion/rho meson mass ratio M, and the renormalised gauge and quark anisotropies ξ_g and ξ_q, and use these to determine the Karsch coefficients. These coefficients will then be used to calculate the renormalised energy density, pressure and trace anomaly for a range of values of μ on three different volumes/temperatures and extrapolated to the zero diquark charge limit.

3.2 Method Outline

To achieve all this we need to do the following:

- Calculate the lattice spacing a_s. For this we will use the static quark potential, which is discussed on page 53.

- Extend existing meson fitting framework to study the meson dispersion relation giving the pion/rho meson mass ratio $M = \frac{m_\pi}{m_\rho}$ and the measured quark anisotropy ξ_q. This is discussed on page 60.
- Use the sideways potential to give the measured gauge anisotropy ξ_g. This is discussed on page 57.
- Use all the results coming from each measurement to give the final answer for the Karsch coefficients with error bars. This is discussed on page 65.

The action in terms of bare parameters is

$$S = S_q(\kappa, \gamma_q) + S_g(\beta, \gamma_g) + S_j = S_q(\kappa_s, \kappa_t) + S_g(\beta_s, \beta_t) + S_j, \tag{3.1}$$

where S_j is the diquark action defined later in equation 3.9. We define the gauge and quark coupling anisotropy parameters γ_g and γ_q such that $\beta_s = \frac{\beta}{\gamma_g}$, $\beta_t = \gamma_g\beta$, $\kappa_t = \gamma_q\kappa$, $\kappa_s = \kappa$, where s denotes spatial and t denotes temporal. We will make use of both notations. The bare parameters β, κ, and the input quark and gauge anisotropies γ_q and γ_g are assumed to be functions of the lattice spacing a_s, the pion/rho meson mass ratio M, and the renormalised anisotropy combinations ξ_+ and ξ_-, where $\xi_+ = \frac{1}{2}(\xi_g + \xi_q)$ and $\xi_- = \frac{1}{2}(\xi_g - \xi_q)$ are defined to ensure we are working along a constant line of physics. The physical anisotropy is then ξ_+, while ξ_- is defined to balance the definition of ξ_+ in the four-dimensional fit, which means that the other derivatives are taken at fixed $\xi_- = 0$. All configurations used for determination are simulated at zero diquark source charge, and the ensembles used in chapter 4 are extrapolated to the zero diquark charge limit, meaning that the diquark action S_j can be ignored for the purposes of the determination.

Inverting the parameter dependences allows us to Taylor expand around the central set where we assume a linear approximation is adequate, which I will examine in a later section. The parameters for the other sets should be chosen such that together they give points either side of the central set. They should also be close enough to the central set as to limit non-linear effects but far enough to give a finite difference. This will allow for the variation of a measured quantity to be given in terms of input parameters which we can write as a set of first order Taylor expansions:

$$\frac{a - a_0}{a_0} = a_1 \frac{\Delta\beta}{\beta_0} + b_1 \Delta\gamma_g + c_1 \Delta\gamma_q + d_1 \frac{\Delta\kappa}{\kappa}, \tag{3.2}$$

$$\xi_+ - \xi_+^0 = a_2 \frac{\Delta\beta}{\beta_0} + b_2 \Delta\gamma_g + c_2 \Delta\gamma_q + d_2 \frac{\Delta\kappa}{\kappa}, \tag{3.3}$$

$$\frac{M - M_0}{M_0} = a_3 \frac{\Delta\beta}{\beta_0} + b_3 \Delta\gamma_g + c_3 \Delta\gamma_q + d_3 \frac{\Delta\kappa}{\kappa}, \tag{3.4}$$

$$\xi_- - \xi_-^0 = a_4 \frac{\Delta\beta}{\beta_0} + b_4 \Delta\gamma_g + c_4 \Delta\gamma_q + d_4 \frac{\Delta\kappa}{\kappa}, \tag{3.5}$$

where $\Delta\beta = \beta - \beta_0$, $\Delta\gamma_g = \gamma_g - \gamma_g^0$, $\Delta\gamma_q = \gamma_q - \gamma_q^0$, $\Delta\kappa = \kappa - \kappa_0$, and the zero subscript denotes the central set. These are all input parameters, so are known before any measurement or determination takes place. In the case of equations (3.2) and (3.4) we divide across by the lattice spacing and mass ratio respectively to ensure the Karsch coefficients are dimensionless and in the same format as in the thermodynamic equations. The differences in β and κ are normalised by the central values to make analysis of parameter selection clearer.

The determination can be done using two different methods. In the first method the input parameters are seen as a linear function of the output parameters and requires additional fits to generate proper statistics as the standard deviations of the input parameters are not known. This was used by Levkova, Manke and Mawhinney [74] in a study using two-flavour staggered fermions in SU (3) and they examined finite temperature thermodynamics using anisotropic lattices in the fixed parameter scheme. They determine the Karsch coefficients by measuring the meson mass fits, the dispersion relation and the static potential. An observation they make based on these fits, is that there are larger errors on the Karsch coefficients with derivatives with respect to the lattice spacing a_s, than the errors with respect to the anisotropy although they admit this could be down to parameter choice.

In the second method the output parameters are seen as linear functions of the input parameters and requires an inversion to get the Karsch coefficients. These methods were shown to be equivalent within errors in a study by the TrinLat group [75] [76] [77]. This is the method that will be used here.

Every set has a measurement value while the differences depend on parameter selection. The larger the difference the more influence a particular set has on the determination. Combining the renormalised quark and gauge anisotropies gives ξ_+ and ξ_-, and by calculating the mass ratio M and the lattice spacing a_s allows us to solve for the fit coefficients $a_1, ..., a_4, b_1, ..., d_4$, which are defined as the derivatives

of the observables with respect to the input parameters given by the 4×4 matrix shown below, which is then inverted to get the matrix in terms of Karsch coefficients.

$$\begin{pmatrix} a_1 & b_1 & c_1 & d_1 \\ a_2 & b_2 & c_2 & d_2 \\ a_3 & b_3 & c_3 & d_3 \\ a_4 & b_4 & c_4 & d_4 \end{pmatrix}^{-1} = \begin{pmatrix} \frac{\beta}{a_0}\frac{\partial a}{\partial \beta} & \frac{1}{a_0}\frac{\partial a}{\partial \gamma_g} & \frac{1}{a_0}\frac{\partial a}{\partial \gamma_q} & \frac{\kappa}{a_0}\frac{\partial a}{\partial \kappa} \\ \beta\frac{\partial \xi_+}{\partial \beta} & \frac{\partial \xi_+}{\partial \gamma_g} & \frac{\partial \xi_+}{\partial \gamma_q} & \kappa\frac{\partial \xi_+}{\partial \kappa} \\ \frac{\beta}{M_0}\frac{\partial M}{\partial \beta} & \frac{1}{M_0}\frac{\partial M}{\partial \gamma_g} & \frac{1}{M_0}\frac{\partial M}{\partial \gamma_q} & \frac{\kappa}{M_0}\frac{\partial M}{\partial \kappa} \\ \beta\frac{\partial \xi_-}{\partial \beta} & \frac{\partial \xi_-}{\partial \gamma_g} & \frac{\partial \xi_-}{\partial \gamma_q} & \kappa\frac{\partial \xi_-}{\partial \kappa} \end{pmatrix}^{-1}$$

$$= \begin{pmatrix} \frac{a_0}{\beta}\frac{\partial \beta}{\partial a} & \frac{1}{\beta}\frac{\partial \beta}{\partial \xi_+} & \frac{M_0}{\beta}\frac{\partial \beta}{\partial M} & \frac{1}{\beta}\frac{\partial \beta}{\partial \xi_-} \\ a_0\frac{\partial \gamma_g}{\partial a} & \frac{\partial \gamma_g}{\partial \xi_+} & M_0\frac{\partial \gamma_g}{\partial M} & \frac{\partial \gamma_g}{\partial \xi_-} \\ a_0\frac{\partial \gamma_q}{\partial a} & \frac{\partial \gamma_q}{\partial \xi_+} & M_0\frac{\partial \gamma_q}{\partial M} & \frac{\partial \gamma_q}{\partial \xi_-} \\ \frac{a_0}{\kappa}\frac{\partial \kappa}{\partial a} & \frac{1}{\kappa}\frac{\partial \kappa}{\partial \xi_+} & \frac{M_0}{\kappa}\frac{\partial \kappa}{\partial M} & \frac{1}{\kappa}\frac{\partial \kappa}{\partial \xi_-} \end{pmatrix}. \tag{3.6}$$

Repeating this process with the data files gained using the bootstrap method gives a set of matrices which will be used to give their respective error values. This inversion, although straightforward, raises a number of issues regarding propagation of errors. Controlling the final errors requires a high level of accuracy in the initial measurements as small errors may have a large effect upon inversion. The value of a particular Karsch coefficient and associated errors depend on all the fit coefficients of the input matrix, and are only as accurate as the worst defined measurement.

3.3 Initial Setup

In this project the anisotropic and isotropic sets of configurations are generated in two-colour QCD using two-flavour unimproved Wilson fermion and gauge actions. For the isotropic sets, the action S is the given by:

$$S = -\frac{\beta}{N_C}\left[\sum_{x,i<j} \mathrm{ReTr} U_{ij}(x)\right] + \sum_{i=1,2} \bar{\psi}_i M \psi_i + S_J, \tag{3.7}$$

where N_C is the number of colours, two in this case. The fermion matrix given by:

$$M_{xy} = \delta_{xy} - \kappa \sum_{\nu} \left[(1-\gamma_\nu)\, e^{\mu \delta_{\nu,0}} U_\nu(x)\, \delta_{y,x+\hat{\nu}} + (1+\gamma_\nu)\, e^{-\mu \delta_{\nu,0}} U_\nu^\dagger(y)\, \delta_{y,x-\hat{\nu}}\right], \tag{3.8}$$

and the diquark action is defined as:

$$S_j = \kappa j \sum_x \left[\psi_2^{tr}(x) C\gamma_5\tau_2\psi_1(x) - \bar{\psi}_1(x) C\gamma_5\tau_2\bar{\psi}_2^{tr}(x) \right]. \tag{3.9}$$

The addition of diquark sources to the thermodynamic configurations allows for a controlled study of diquark condensation, lifts the eigenmodes of the Dirac operator and regularises infrared fluctuations in the superfluid phase. For the configurations used in this chapter, the diquark source is set to zero. The contribution of the diquark source to the derivative of S vanishes in the $j \to 0$ limit. In this thesis, the only direct consequence of them is that when calculating the final values of the observables, energy density, pressure etc, is that an extrapolation to $j = 0$ is necessary. As far as the determination of the Karsch coefficients is concerned they can be ignored. The anisotropic sets are only used for the determination and the anisotropic gauge action is defined by:

$$S_G = -\frac{\beta}{N_C}\left[\frac{1}{\gamma_g} \sum_{x,i<j} \mathrm{ReTr} U_{ij}(x) + \gamma_g \sum_{x,i} \mathrm{ReTr} U_{i0}(x) \right], \tag{3.10}$$

where γ_g is the input gauge anisotropy, and the quark action is given by:

$$\begin{aligned} S_Q = &\sum_{x,\alpha} \left[\bar{\psi}^\alpha(x)\psi^\alpha(x) + \gamma_q\kappa\bar{\psi}^\alpha(x)(D_0\psi)^\alpha(x) \right] \\ &+ \kappa \sum_{x,\alpha,i} \bar{\psi}^\alpha(x)(D_i\psi)^\alpha(x) + S_J, \end{aligned} \tag{3.11}$$

where γ_q is the input quark anisotropy and

$$(D_i\psi)^\alpha(x) = (\gamma_i - 1)U_i(x)\psi^\alpha(x+\hat{\imath}) - (\gamma_i + 1)U_i^\dagger(x-\hat{\imath})\psi^\alpha(x-\hat{\imath}), \tag{3.12}$$

$$(D_0\psi)^\alpha(x) = (\gamma_0 - 1)U_0(x)e^\mu\psi^\alpha\left(x+\hat{0}\right) - (\gamma_0 + 1)U_0^\dagger\left(x-\hat{0}\right)e^{-\mu}\psi^\alpha\left(x-\hat{0}\right). \tag{3.13}$$

are the spatial and temporal Dirac operators. The introduction of the chemical potential occurs as an exponential term in the temporal operator as explained previously but the chemical potential is set to zero for the determination configurations so is only included here for completeness.

After discussing lattice actions and possible improvements in the first chapter, an obvious question is why are we using an unimproved Wilson gauge and quark action?

As this study of thermodynamics in QC_2D is the first in the area, starting with a simple action makes sense as it allows for a lower computational cost. It also allows for comparison with the group's previous work in QC_2D, [78][59][64]. Improvements between generations of configurations can be made in the form of reducing the lattice spacing, and by looking at larger volumes.

Wilson actions are preferred to staggered actions, as the behaviour of staggered actions at non-zero chemical potential is not known. There are also rooting issues as there are only two flavours in this study, not four as is the standard definition for staggered actions. Finally improving the action means dealing with extra terms which requires additional programming and added computational overheads, not only in terms of determining the value of the additional coefficients which control the improvement but also extra ensembles needed to determine their influence with regards to the Karsch coefficients as was briefly mentioned in chapter 3.

Set	β_s	β_t	κ_s	κ_t	γ_g	γ_q	$\Delta\beta$	$\Delta\gamma_g$	$\Delta\kappa$	$\Delta\gamma_q$
0	1.90	1.90	0.1680	0.1680	1.0	1.0	–	–	–	–
1	2.37	1.52	0.1680	0.1680	0.8	1.0	−0.002	−0.199	0	0
2	1.27	2.83	0.1680	0.1680	1.5	1.0	0.0025	0.498	0	0
3	1.90	1.90	0.1800	0.1570	1.0	0.87	0	0	0.012	−0.127
4	1.90	1.90	0.1470	0.1920	1.0	1.3	0	0	−0.021	0.306
5	1.80	1.80	0.1740	0.1740	1.0	1.0	−0.1	0	0.006	0
6	1.90	1.90	0.1685	0.1685	1.0	1.0	0	0	0.0005	0
7	2.00	2.00	0.1620	0.1620	1.0	1.0	0.1	0	−0.006	0
8	2.00	2.00	0.1630	0.1630	1.0	1.0	0.1	0	−0.005	0
9	1.90	1.90	0.1680	0.1340	1.0	0.80	0	0	0	−0.202

Table 3.1: Parameters of the determination sets beginning with the central set. Also given are the delta values used in equations (3.2) – (3.5) which give the relative difference to the central set.

The parameters of determination configuration sets are given in table (3.1) starting with the central set, the main anisotropic sets, the isotropic sets and the remaining anisotropic set 9 which was a later addition as initial measurements suggested it was isotropic and that the data were unreliable but improved fits suggest that it is indeed anisotropic.

Another issue is the use of unphysical anisotropic sets for the determination of Karsch coefficients. Using anisotropic lattices to directly model physical objects requires tuning to ensure correct physics. If the resulting measured quark and gauge anisotropies ξ_q and ξ_g differ, there will be a breaking of rotational symmetry which will give improper physics. Using unphysical or improper anisotropic sets for determination is legitimate as long as we are not measuring quantities which will be affected by this property.

Uncertainties for all fits which include the measurements and determination are provided by the bootstrap method. That is, given a sample set of size N, bootstrap sets are then generated by randomly selecting data from this sample, replacing each time until a new sample of size N is generated. We take as standard one hundred samples per set regardless of how many configurations are present. These are later used along with the central values to determine the Karsch coefficients. Using the same bootstrap samples for all quantities ensures correlations between different quantities are properly handled.

3.4 The Static Quark Potential

Scale setting has always played an important part in lattice calculations as there is no point having results on the lattice and having no way of comparing them with their real world experimental counterparts. There are now plenty of popular methods to do this. They all have a similar aim, determine some observable on the lattice to high precision and compare this with its real world counterpart which we already know from experiment. They then use this calculation as a benchmark to set all other physical or theoretical observables. Obviously choosing an observable which is well behaved and reasonable to calculate on the lattice would be a good idea. Also the experimental value should be known to a high degree of accuracy, examples of this are f_K and Υ splitting. Among the most common quantities being used are the string tension σ or the Sommer scale r_0 from the static quark potential and the Wilson scale w_0. These are not experimentally observable but can be indirectly related to experiment and should all agree for the same lattice observable in the continuum limit.

In this project we used the string tension from the static quark potential and then improved upon it by using the Sommer scale. The Wilson loop gauge action takes β as an input but does not contain the lattice spacing a_s. If we construct a closed rectangular path $C(R,T)$ with spatial extent R and temporal extent T, we can then extract the potential by using the Wilson loop $W(R,T)$ which we defined earlier

as the trace over path-ordered products of link variables $U_\mu(n)$ over the the path $C(R,T)$. This corresponds to the world line of a quark-antiquark pair at rest a distance R apart, over a time T. The potential betweem two static quarks at a fixed spatial distance R and large temporal separation t is related to the Wilson loop by [13]:

$$V(R) = \lim_{T\to\infty} -\frac{1}{T}\log\langle W(R,T)\rangle \tag{3.14}$$

This allows us to extract the potential from the Wilson loops. We model it with the Cornell potential [79]

$$V(r) = \sigma r - \frac{\alpha}{r} + C, \tag{3.15}$$

where σ is the string tension and α is the Coulomb parameter. The string tension is taken to be $\sqrt{\sigma} = 440\text{MeV}$, corresponding to its value in real QCD. This is somewhat arbitrary but allows us to compare with real QCD. The gauge links are smeared to improve the signal. The current code examines all possible loops, which gives a considerable number of points to fit, allowing for a reasonable determination. The downside is that as the number and variety of loops are related to the volume, it scales poorly, and other methods such as the Wilson flow [80] have been looked at as a possible long-term replacement for scale setting, as it appears to be an improvement in terms of efficiency and accuracy.

3.4.1 Results

Below we plot the results from the static potential for all ten sets in figure (3.1). We fit parameters σ, α and C from equation (3.15) and use the real QCD value of the string tension to set the scale. C varies from fit to fit but is effectively a meaningless constant. The fit range is shown in blue and we analyse for time $T \geq T_{min}$ where T_{min} is the lower cutoff where excited states no longer interfere, which is given for each plot. The number of sample points has been reduced to remove effects caused by rotational symmetry violations. We do this by implementing a diagonal cut, by which we ignore those loops which extend further than a set distance from the diagonal. We reduce this distance until pairs of points which are clearly caused by rotational symmetry violations are outside the points sampled. The fits for most sets are very well behaved, however the computational cost of determining the lattice spacing is rather high. In this project we used 12^3x24 lattices and it took between 23 and 24 hours per configuration on one core of the department computer lab

workstations with specifications given in section 5.1. Tests on larger configurations have crashed due to memory issues. Streamlining existing code or switching to a more economical method such as the Wilson flow [80] should reduce this cost and allow for accurate measurements on larger volumes.

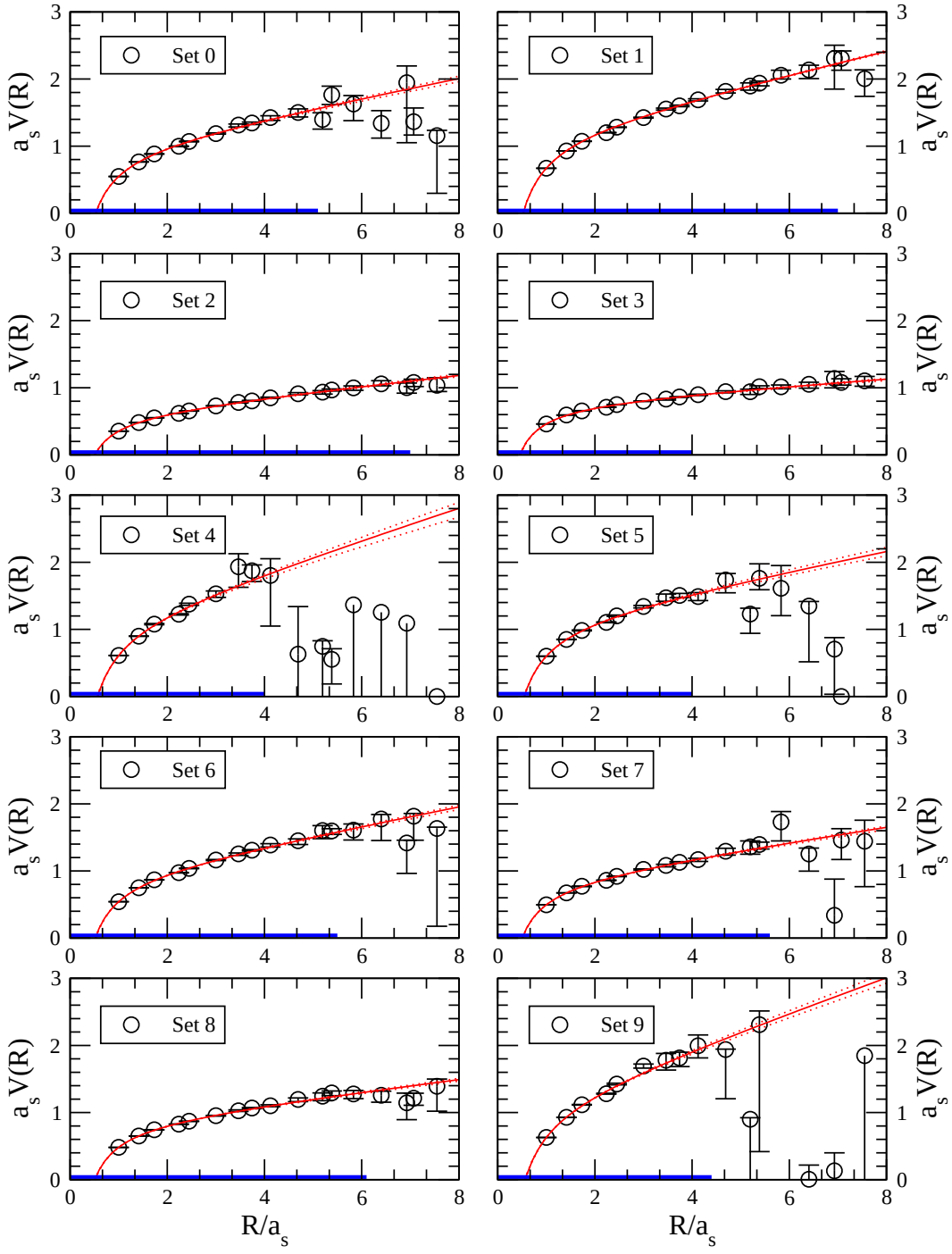

Figure 3.1: Static potential plots for all ten sets. Fit ranges are shown in blue.

One immediate improvement is to use the Sommer scale approach. This idea originates in pure gauge theory where the string tension is defined [81] as $K = \lim_{r\to\infty} F(r)$.

Statistical noise and systematic errors renders this unpractical. While the basic fit uses the linear part of the Cornell potential to extract the lattice spacing, using the Sommer scale makes use of both the linear part and the $1/R$ term. We can examine the force at intermediate distance by calculating R such that:

$$R^2 \left.\frac{\mathrm{dF}}{\mathrm{d}R}\right|_{R=r_0} = 1.65, \tag{3.16}$$

which implies [82] that:

$$\frac{r_0}{a_s} = \sqrt{\frac{\alpha + 1.65}{\sigma a_s^2}}. \tag{3.17}$$

We can use this prescription in our analysis at no extra computational cost.

Set	String tension a_s (fm)	Sommer a_s (fm)	χ^2/dof	$\frac{\Delta a_s}{a_s^0}(\sigma)$	$\frac{\Delta a_s}{a_s^0}$(Som)
0	0.179^{+5}_{-6}	0.178^{+3}_{-4}	3.295	-	-
1	0.192^{+3}_{-4}	0.201^{+2}_{-3}	7.791	0.072	0.129
2	0.133^{+3}_{-3}	0.121^{+2}_{-2}	2.836	−0.257	−0.319
3	0.107^{+3}_{-5}	0.099^{+2}_{-4}	3.194	−0.404	−0.445
4	0.229^{+8}_{-13}	0.241^{+5}_{-8}	5.413	0.277	0.354
5	0.179^{+7}_{-7}	0.188^{+5}_{-6}	5.868	0.003	0.056
6	0.177^{+3}_{-4}	0.174^{+3}_{-4}	5.004	−0.012	−0.023
7	0.157^{+3}_{-5}	0.151^{+2}_{-4}	2.946	−0.123	−0.155
8	0.141^{+3}_{-3}	0.135^{+2}_{-3}	3.487	−0.213	−0.240
9	0.241^{+7}_{-7}	0.256^{+4}_{-5}	9.462	0.344	0.435

Table 3.2: Spatial lattice spacings from fits to Cornell potential using string tension and improved Sommer scale with the associated chi squared per degree of freedom. Also given is the relative difference to the central set as used in the linear fits. Most of the sets have a reasonable delta values except for sets 5 and 6.

In table (3.2) we give the results for the static quark potential for both string tension and Sommer schemes. Using a prescription which takes rotational symmetry violations into account [83] should allow a larger sample set. The Sommer scale improvement uses both α and σ to calculate the lattice spacing but as the same fit ranges are used, it has the same chi squared. The results are fairly consistent

between the two schemes. Switching to the Sommer scale improves accuracy at no extra computational cost.

3.5 The Sideways Potential

On the lattice there are actually two potentials, the "regular" and the "sideways" potentials associated with the spatial and temporal directions respectively. If we compare Wilson loops in the spatial-temporal plane with those in the spatial-spatial plane we should be able to get a good measurement of the gauge anisotropy ξ_g of a given configuration[84]. The ratios of Wilson loops are defined as:

$$R_x(x,y) = \log\left(\frac{W_{ss}(x,y+1)}{W_{ss}(x,y)}\right) = Z_{xy}e^{-yV_{xy}} + \text{excited states}, \tag{3.18}$$

$$R_t(x,t) = \log\left(\frac{W_{st}(x,t+1)}{W_{st}(x,t)}\right) = Z_{xt}e^{-tV_{xt}} + \text{excited states}. \tag{3.19}$$

where W_{ss} and W_{st} are loops in the space-space and space-time directions. This becomes valid for large distances in y and t. For an isotropic configuration, the two potentials are equal and should return the expected anisotropy of one. On anisotropic lattices, this allows us to compare the potential measured in the coarse-coarse direction V_{xy} with the coarse-fine direction V_{xt} and equate them in terms of physical distance. As V_{xy} and V_{xt} are in terms of the lattice spacings a_s and a_t, they differ by a factor of ξ_g along with an additive constant coming from self-energy corrections [85]. If we look at the ratio of the difference of the potentials at two distances these corrections cancel and we get a measurement of the gauge anisotropy as:

$$\xi_g = \frac{V_{xt}(R_2) - V_{xt}(R_1)}{V_{xy}(R_2) - V_{xy}(R_1)}, \tag{3.20}$$

where V_{xt}, V_{xt} are potentials obtained from Wilson loops at distances R_1 and R_2.

Results for the sideways potential are shown below in table 3.3 and figure 3.2.

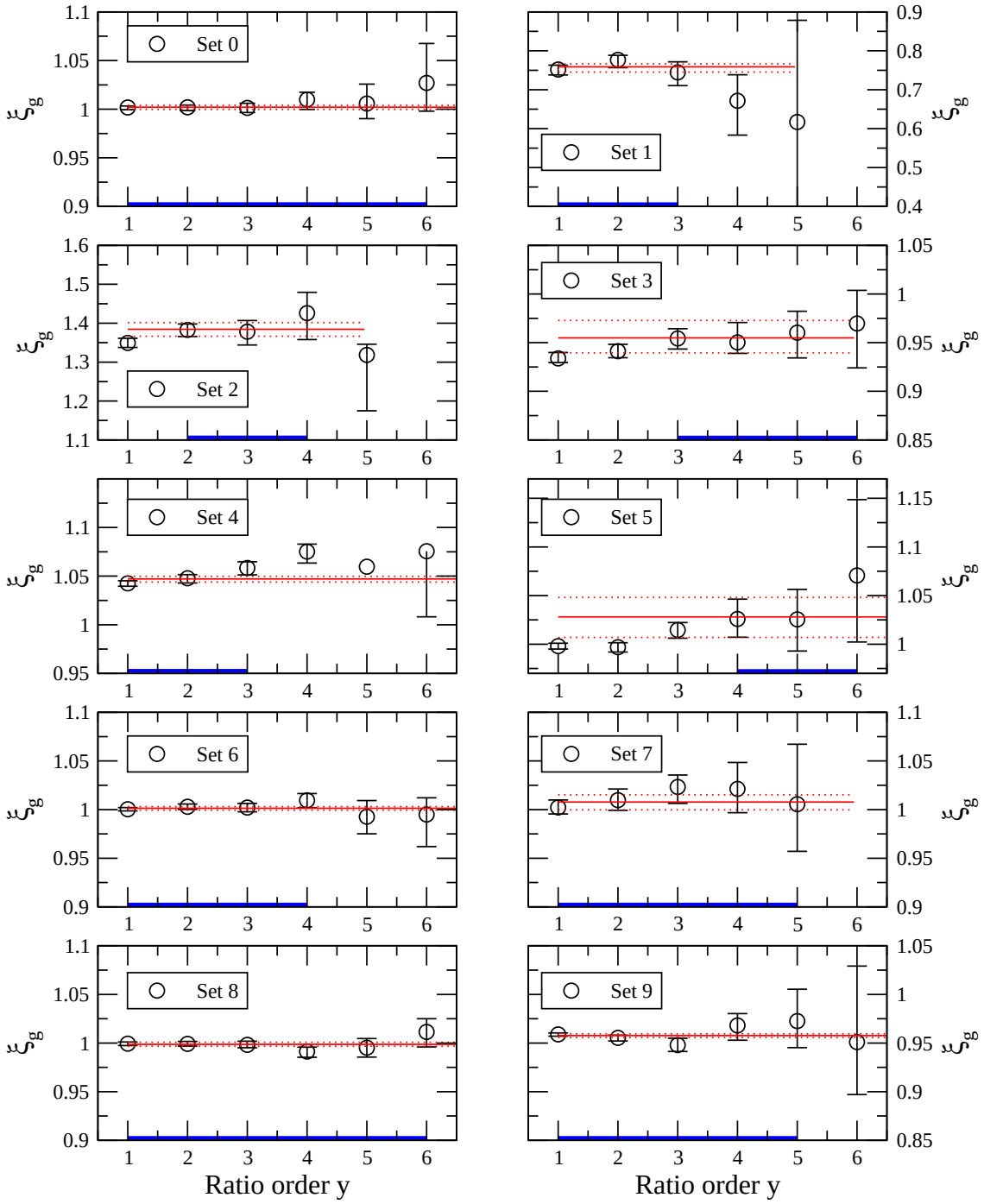

Figure 3.2: Sideways potential results with fit ranges shown in blue. While we fitted ratios at different ranges of R_2 and R_1, those shown are the cleanest at $R_2 = 2$, $R_1 = 1$. On the y axis is the output value of ξ_g while the x axis shows the increasing ratio points for y.

Set	ξ_g	χ^2/dof	$\Delta\xi_+$	$\Delta\xi_-$
0	1.002^{+2}_{-2}	0.242	–	–
1	0.759^{+8}_{-14}	1.023	−0.197	−0.047
2	1.384^{+17}_{-18}	0.257	0.314	0.069
3	0.955^{+18}_{-15}	0.138	−0.102	0.055
4	1.047^{+3}_{-3}	4.593	0.251	−0.206
5	1.028^{+20}_{-21}	0.179	0.023	0.003
6	1.001^{+2}_{-2}	0.635	−0.002	0.001
7	1.008^{+7}_{-8}	0.506	−0.019	0.025
8	0.999^{+2}_{-2}	0.631	−0.013	0.009
9	0.958^{+2}_{-2}	0.988	−0.043	−0.001

Table 3.3: Gauge anisotropy determination. Listed are both $\Delta\xi_+$ and $\Delta\xi_-$ as the gauge anisotropy is combined with the quark anisotropy. Naturally the anisotropic sets dominate the delta values.

The chi-squared values are reasonable but this may be due to the small number of points sampled. In future studies, including irregular shaped loops will give additional sample points at intermediate distances. The isotropic sets are relatively well behaved while the anisotropic sets use even fewer points. The fits are reasonable considering the naive implementation. Smearing should help improve results by dampening errors.

Our calculations uses square and rectangular shaped Wilson loops which allows for an uncomplicated and rather quick calculation of the sideways potential. One possible improvement to this would be to look at more complicated objects. In theory the static quark potential code could be, with some work, altered to calculate this although currently a stand alone and somewhat simpler method is appropriate. The signal to noise ratio is also quite poor which could be improved by using an optimised smearing method. Smearing was used for the static quark potential, however here the implementation is more complex. Instead of smearing just the spatial gauge links, we would now have to smear both the spatial and temporal links by the same physical amount. For the temporal direction this becomes "thermally averaged" time-like links [85], but implementing this was beyond the scope of this project.

3.6 The Meson Dispersion

The meson dispersion calculation is based on an existing program which calculated the meson spectrum [59] and added a function to give them finite momentum using the fast Fourier transform. We can then measure the mass ratio of a pair of mesons, in this case the pion and rho mesons, at zero momentum giving m_0 along with the meson dispersion relation for small momenta giving the quark anisotropy ξ_q. The mass fit relies on the asymptotic behaviour of the meson correlator, in this case for the pion and rho mesons. The effective mass can be calculated using

$$M_{eff}(\tau) = \log\left(\frac{C(\tau)}{C(\tau+1)}\right) \underset{\tau\to\infty}{\longrightarrow} \log\left(\frac{C_0 e^{-m\tau}}{C_0 e^{-m(\tau+1)}}\right) \tag{3.21}$$

where m is the mass of the meson we are trying to fit and $C(\tau)$ is a connected 2-point correlation function which can be written as

$$C(\tau) = \sum_{x,y} \left\langle \bar{\psi}(x,t)\,\Gamma\psi(x,t)\,\bar{\psi}(y,t+\tau)\,\bar{\Gamma}\psi(y,t+\tau)\right\rangle \tag{3.22}$$

where Γ is an meson operator. Instead of averaging over all values of t we use the point source $t = 0$. This decreases the number of inversions needed to calculate the correlators and allows us to add non-zero momenta by carrying out a Fourier transform with discrete momenta values. At large time separations a plateau should be seen in their effective mass plots. The meson correlator's maximum fit range is halved as it is symmetric about $\frac{N_t}{2}$. For the dispersion relation we initially used the continuum definition, which is given by:

$$a_\tau^2 E^2 = a_\tau^2 m_0^2 + \frac{a_s^2 k^2}{\xi_q^2}, \tag{3.23}$$

where $k^2 = k_x^2 + k_y^2 + k_z^2$ is the momentum. After reviewing results and receiving some helpful suggestions from Axel Maas we then repeated the analysis using the lattice meson dispersion, which replaces the continuum momenta with the lattice definition [86]:

$$k_{\text{eff}}^2 = \frac{4}{a_s^2}\left[\sin^2\left(\frac{a_s k_x}{2}\right) + \sin^2\left(\frac{a_s k_y}{2}\right) + \sin^2\left(\frac{a_s k_z}{2}\right)\right]. \tag{3.24}$$

For small volumes or coarse lattice spacing this plateau can be difficult to distinguish,

especially for increasing momenta. All points in the dispersion plots are generated by mass fits across a range of momenta which directly depends on the lattice spacing. Normally a reduction in lattice spacing would be seen as an improvement, but for the dispersion relation an increase in N_t and N_s is more important to improve resolution for the correlator and increase the number of discrete momenta values available as the momenta is related to the volume by $p_n = \frac{2\pi n}{N_s a_s}$.

3.6.1 Results

Fitting the meson dispersion gives the mass ratio M of the pion m_π and rho meson m_ρ, and the quark anisotropy ξ_q. As the mass ratio is a comparison of fits from the pion and rho meson, there is a χ^2 dependence from each mass fit shown below in table (3.4).

set	M	χ^2_π/dof	χ^2_ρ/dof	$\frac{\Delta M}{M_0}$
0	0.794^{+4}_{-7}	0.529	0.116	–
1	0.804^{+3}_{-4}	0.492	0.547	0.012
2	0.630^{+7}_{-7}	0.077	0.529	−0.207
3	0.715^{+19}_{-12}	0.044	6.923	−0.100
4	0.946^{+1}_{-1}	0.028	0.027	0.191
5	0.770^{+5}_{-7}	0.228	0.307	−0.031
6	0.759^{+12}_{-13}	0.374	0.232	−0.044
7	0.819^{+8}_{-7}	0.989	0.452	0.031
8	0.756^{+1}_{-7}	0.122	0.373	−0.049
9	0.931^{+2}_{-1}	1.644	3.144	0.172

Table 3.4: Mass ratio values, the individual chi-squared valued for the pion and rho meson mass fits, and ΔM which gives the relative distance to the central set. Sets 2, 3, 4 and 9 which are all anisotropic, dominate.

While the mass fits are well behaved, the number of points deemed to be in the plateau is rather small. These plateaus are identified by varying fit ranges, comparing χ squared values and by eye. The effective mass is the y-value of these plateaus. Increasing N_t will reduce identification errors as well as fit errors. The fit ranges are shown in figure (3.3) below and the same range is used for both the pion and rho mesons at zero momenta.

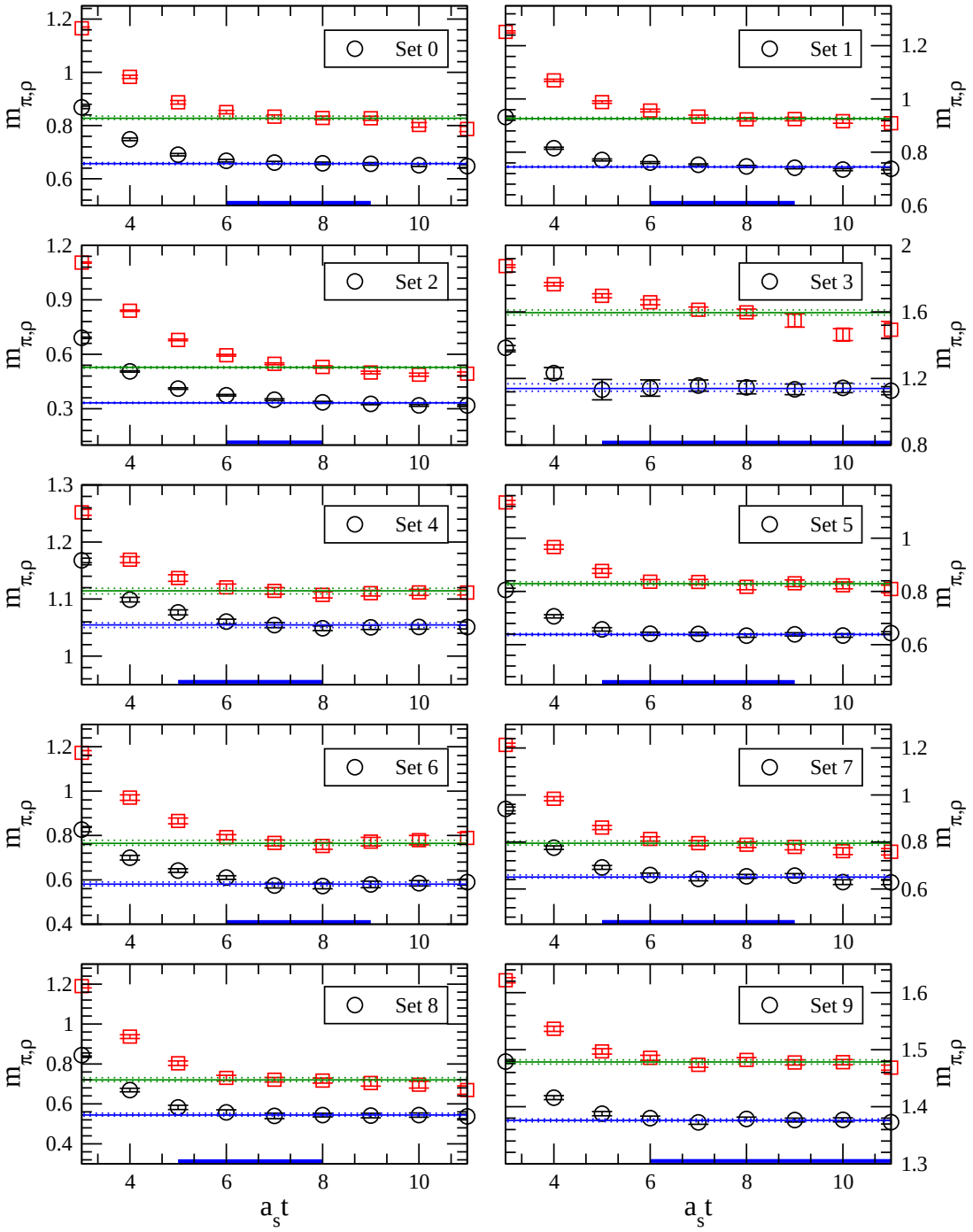

Figure 3.3: Mass fit giving the pion (black) and rho meson (red) values. We use the same fit ranges for both mesons which is given by the solid blue lines.

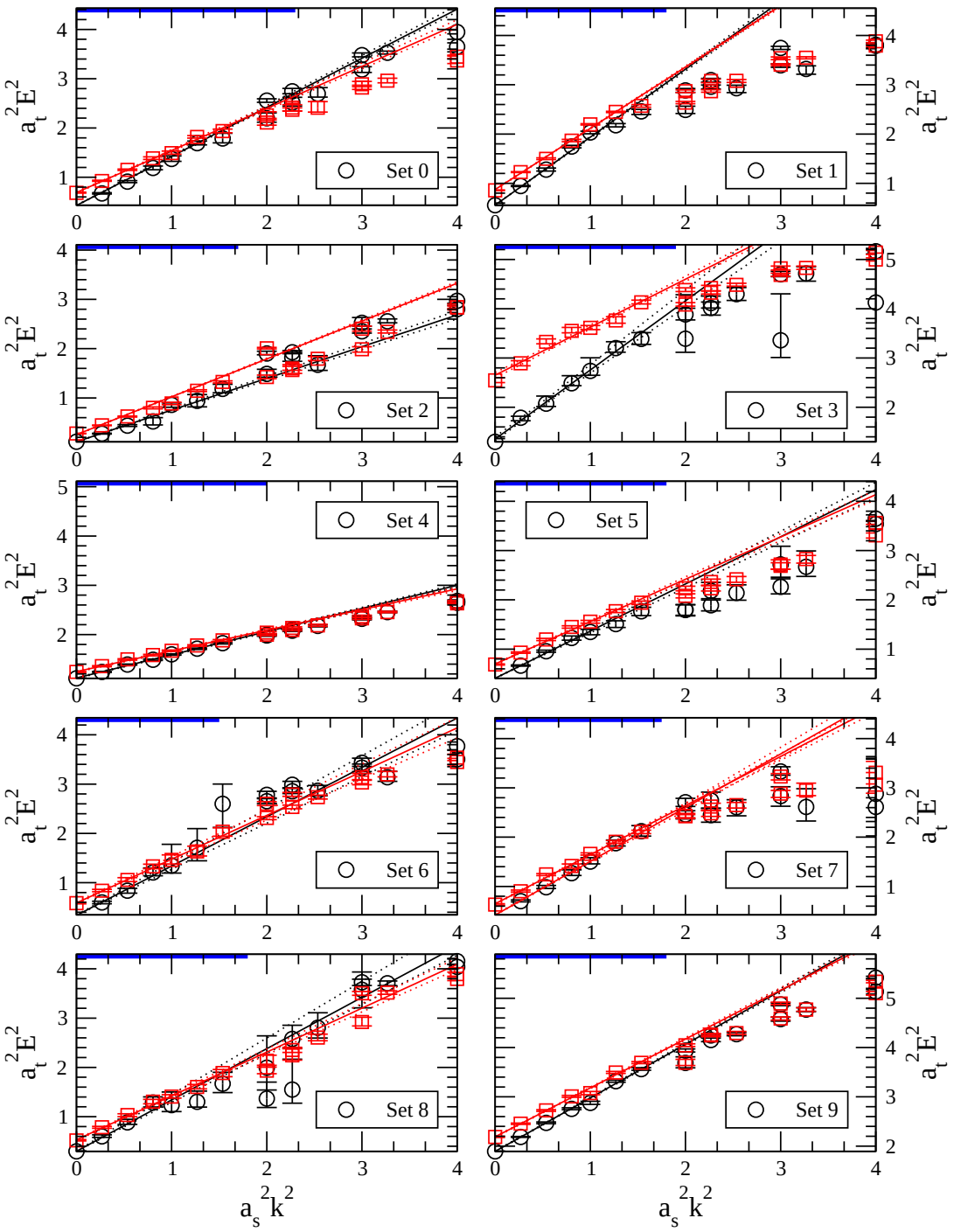

Figure 3.4: Meson dispersion relation for the pion (black) and rho meson (red). Fit range for the pion is given in blue while the rho meson dispersion is only shown for comparison.

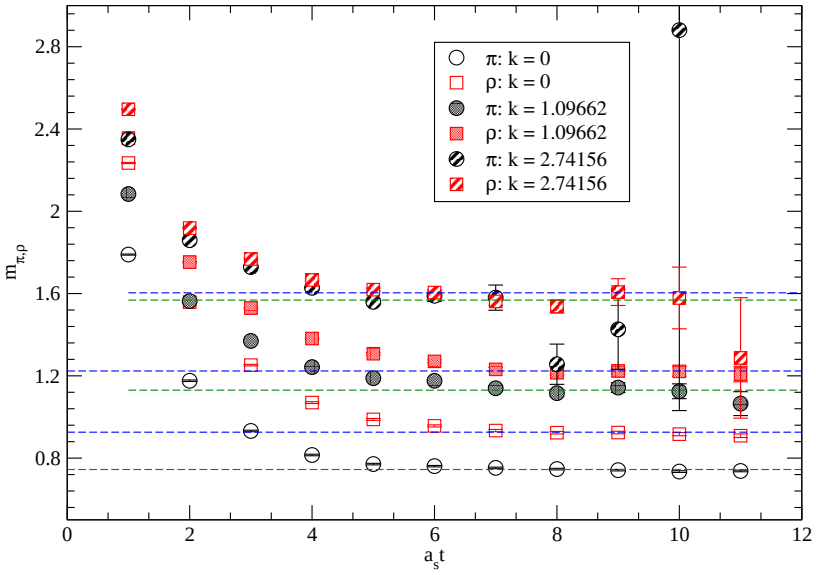

Figure 3.5: Mass plots for set 1 used in dispersion relation.

Shown in figure (3.5) is an example of a few points used in set 1. At higher momenta the plateau becomes shorter and harder to distinguish. The results using the naive continuum dispersion relation are shown in table 3.5. Updated results using the lattice dispersion relation are given in table 3.6.

set	$\xi_{q(\pi)}$	χ^2/dof	$\xi_{q(\rho)}$	χ^2/dof	$\Delta\xi_+$	$\Delta\xi_-$
0	$1.002\,^{+7}_{-10}$	2.339	$1.002\,^{+7}_{-10}$	3.342	–	–
1	$0.880\,^{+6}_{-6}$	15.850	$0.933\,^{+5}_{-5}$	19.986	−0.183	−0.061
2	$1.273\,^{+21}_{-21}$	1.088	$1.175\,^{+5}_{-6}$	46.602	0.326	0.056
3	$0.875\,^{+24}_{-35}$	1.068	$1.057\,^{+18}_{-18}$	6.063	−0.087	0.040
4	$1.517\,^{+15}_{-12}$	2.164	$1.607\,^{+17}_{-14}$	1.409	0.280	−0.235
5	$1.049\,^{+22}_{-20}$	2.716	$1.119\,^{+17}_{-15}$	4.397	0.037	−0.011
6	$1.014\,^{+35}_{-37}$	0.332	$1.088\,^{+32}_{-33}$	0.777	0.006	−0.006
7	$0.986\,^{+14}_{-20}$	0.232	$1.043\,^{+14}_{-11}$	4.785	−0.005	0.011
8	$1.003\,^{+23}_{-47}$	2.375	$1.100\,^{+16}_{-19}$	2.412	−0.001	−0.002
9	$0.992\,^{+6}_{-7}$	4.904	$1.041\,^{+6}_{-10}$	6.361	−0.027	−0.017

Table 3.5: Original quark anisotropy ξ_q where we use the pion dispersion results in the determination. Listed is both $\Delta\xi_+$and $\Delta\xi_-$as the quark anisotropy is combined with the gauge anisotropy.

set	$\xi_{q(\pi)}$	χ^2/dof	$\xi_{q(\rho)}$	χ^2/dof	$\Delta\xi_+$	$\Delta\xi_-$
0	1.002^{+7}_{-10}	4.389	1.083^{+12}_{-15}	1.992	–	–
1	0.852^{+6}_{-6}	11.832	0.897^{+5}_{-4}	23.689	−0.197	−0.047
2	1.247^{+20}_{-20}	2.091	1.141^{+4}_{-7}	66.663	0.314	0.069
3	0.845^{+23}_{-33}	0.870	1.013^{+17}_{-18}	4.613	−0.102	0.055
4	1.458^{+14}_{-12}	1.231	1.544^{+16}_{-14}	0.733	0.251	−0.206
5	1.022^{+21}_{-20}	1.490	1.079^{+17}_{-15}	2.027	0.023	0.003
6	1.000^{+34}_{-36}	0.345	1.061^{+33}_{-32}	0.333	−0.002	0.001
7	0.958^{+14}_{-19}	0.568	1.002^{+13}_{-11}	3.346	−0.019	0.025
8	0.980^{+23}_{-46}	1.726	1.060^{+16}_{-19}	1.114	−0.013	0.009
9	0.959^{+6}_{-7}	3.208	1.004^{+6}_{-9}	3.748	−0.043	−0.001

Table 3.6: Improved quark anisotropy ξ_q where we use the pion dispersion results in the determination. The anisotropic sets naturally dominate the delta values. Listed is both $\Delta\xi_+$and $\Delta\xi_-$as the quark anisotropy is combined with the gauge anisotropy.

The quark anisotropy ξ_q determination is more dependent on finite volume due to reliance on momenta. Sets 7 and 8 differ from 1 although they are both isotropic. There is a noticeable discrepancy between the pion and rho meson anisotropy calculations. Different operators respond to the anisotropy differently, and we use the pion dispersion relation to determine the anisotropy. Switching to the lattice version of the meson dispersion does bring about a slight reduction in the error bars of both the quark anisotropy ξ_q and the Karsch coefficients, although the effect is mostly at larger momenta which is already noisy. Visually upon inspection there appears to be more linear behaviour than the unimproved fits. Points which differed due to rotational symmetry although they had equivalent momenta are almost equivalent, but this is more so at higher momenta where we would not expect to fit.

3.7 The Karsch coefficients

At this stage four measurements have been carried out on each of the determination sets with a summary given below of the original calculations in table (3.7) and the subsequent "improved" calculations in table (3.8) for comparison.

set	ξ_g	ξ_q	$\frac{m_\pi}{m_\rho}$	a_s (fm)
0	0.968^{+2}_{-2}	1.035^{+8}_{-10}	0.798^{+4}_{-9}	0.178^{+4}_{-6}
1	0.721^{+2}_{-2}	0.999^{+8}_{-9}	0.807^{+3}_{-3}	0.177^{+4}_{-3}
2	1.321^{+6}_{-5}	1.278^{+21}_{-3}	0.633^{+9}_{-12}	0.125^{+3}_{-5}
3	0.747^{+4}_{-4}	0.875^{+24}_{-34}	0.711^{+19}_{-14}	0.107^{+2}_{-5}
4	1.146^{+4}_{-4}	1.513^{+15}_{-12}	0.946^{+1}_{-1}	0.229^{+7}_{-12}
5	0.989^{+4}_{-3}	1.028^{+16}_{-14}	0.770^{+5}_{-6}	0.177^{+5}_{-7}
6	0.945^{+5}_{-5}	1.020^{+9}_{-11}	0.759^{+11}_{-13}	0.153^{+7}_{-18}
7	0.921^{+4}_{-5}	0.992^{+10}_{-9}	0.819^{+7}_{-6}	0.166^{+1}_{-2}
8	0.881^{+5}_{-5}	1.008^{+9}_{-6}	0.756^{+13}_{-7}	0.148^{+1}_{-1}
9	–	–	–	–

Table 3.7: Measurements as used in [87]. Set 9 was discarded at this stage as it didn't appear to be well defined. Here we used the string tension and the continuum dispersion relation.

set	ξ_g	ξ_q	$\frac{m_\pi}{m_\rho}$	a_s (fm)
0	1.002^{+2}_{-2}	1.002^{+7}_{-10}	0.794^{+4}_{-7}	0.178^{+3}_{-4}
1	0.759^{+8}_{-14}	0.852^{+6}_{-6}	0.804^{+3}_{-4}	0.201^{+2}_{-3}
2	1.384^{+17}_{-18}	1.247^{+20}_{-20}	0.630^{+7}_{-7}	0.121^{+2}_{-2}
3	0.955^{+18}_{-15}	0.845^{+23}_{-33}	0.715^{+19}_{-12}	0.099^{+2}_{-4}
4	1.047^{+3}_{-3}	1.458^{+14}_{-12}	0.946^{+1}_{-1}	0.241^{+5}_{-8}
5	1.028^{+20}_{-21}	1.022^{+21}_{-20}	0.770^{+5}_{-7}	0.188^{+5}_{-6}
6	1.001^{+2}_{-2}	1.000^{+34}_{-36}	0.759^{+12}_{-13}	0.174^{+3}_{-4}
7	1.008^{+7}_{-8}	0.958^{+14}_{-19}	0.819^{+8}_{-7}	0.151^{+2}_{-4}
8	0.999^{+2}_{-2}	0.980^{+23}_{-46}	0.756^{+1}_{-7}	0.135^{+2}_{-3}
9	0.958^{+2}_{-2}	0.959^{+6}_{-7}	0.931^{+2}_{-1}	0.256^{+4}_{-5}

Table 3.8: Improved measurements using the Sommer scale for the lattice spacing, the lattice definition for the dispersion relation, and new fits for all measurements.

Combining the measurements and bootstrap values for ξ_g and ξ_q gives us values for ξ_+ and ξ_-. Subtracting the central set values then gives the required delta values. Using these measurements and equations 3.2 - 3.5, we performed a four dimensional linear fit with respect to a_i, b_i, c_i, d_i, (to give central values) with $nboot = 100$ bootstrap fits to give error bars. Repeating this for each observable gives the results shown below in table (3.9).

	i	$a_i\,(\beta)$	$b_i\,(\gamma_g)$	$c_i\,(\gamma_q)$	$d_i\,(\kappa)$	$\frac{\chi^2}{N_{df}}$
a	1	$-4.830\,^{+159}_{-194}$	$-0.611\,^{+34}_{-27}$	$-2.270\,^{+122}_{-133}$	$-55.198\,^{+1.81}_{-1.58}$	4.52
ξ_+	2	$-0.688\,^{+68}_{-98}$	$0.792\,^{+24}_{-21}$	$0.218\,^{+25}_{-29}$	$-8.554\,^{+592}_{-651}$	11.93
M	3	$-1.086\,^{+62}_{-70}$	$-0.296\,^{+14}_{-14}$	$-0.845\,^{+25}_{-39}$	$-21.259\,^{+561}_{-860}$	16.219
ξ_-	4	$0.700\,^{+93}_{-58}$	$0.170\,^{+19}_{-17}$	$-0.002\,^{+24}_{-23}$	$9.424\,^{+674}_{-511}$	4.189

Table 3.9: These are the results from the linear fits to equations (3.2) - (3.5).

The high chi squared values of all four fits are due to a combination of measurement errors and possibly non-linearities which will be discussed later. The relatively low error values for the fit coefficients which depend on the anisotropy might be attributed to having only two non-zero sample points for $\Delta\gamma_g$ and three non-zero sample points for $\Delta\gamma_q$. This does suggest that parameter choice may skew the source of the errors. Inverting the four-dimensional matrix in table (3.9), we recover the Karsch coefficients shown below in table (3.10).

c_i	$\frac{a}{c_i^0}\frac{\partial c_i}{\partial a}$	$\frac{1}{c_i^0}\frac{\partial c_i}{\partial \xi_+}$	$\frac{M}{c_i^0}\frac{\partial c_i}{\partial M}$	$\frac{1}{c_i^0}\frac{\partial c_i}{\partial \xi_-}$
β	$-0.254\,^{+29}_{-29}$	$0.039\,^{+17}_{-32}$	$0.694\,^{+87}_{-100}$	$0.110\,^{+69}_{-74}$
γ_g	$0.037\,^{+49}_{-41}$	$1.027\,^{+41}_{-41}$	$0.163\,^{+110}_{-130}$	$1.515\,^{+55}_{-84}$
γ_q	$-0.278\,^{+69}_{-99}$	$0.149\,^{+59}_{-58}$	$-0.393\,^{+273}_{-218}$	$-2.378\,^{+174}_{-124}$
κ	$0.209\,^{+29}_{-25}$	$-0.143\,^{+97}_{-83}$	$-0.601\,^{+96}_{-113}$	$0.373\,^{+63}_{-69}$

Table 3.10: The Karsch coefficients. The dependence of β and γ_q on the lattice spacing is present. The input gauge anisotropy responds strongly with the measured anisotropy as expected. β also strongly depends on the mass. In this table we have divided by a factor of c_i^0 where c_i refers to the relevant parameters β, γ_g, γ_q, κ and the zero superscript denotes the central set. In this way the difference in size of input parameter is taken into account, mainly κ which is an order of magnitude smaller than the others as $\beta^0 = 1.9, \gamma_g^0 = 1.0, \gamma_q^0 = 1.0, \kappa^0 = 0.168$.

These results use the improved measurements, while the previous publication [68] used unimproved measurements and contained some errors with regards to the sideways potential. In a previous study by our group [64] they estimated two of the Karsch coefficients to be $a\frac{\partial\beta}{\partial a} = -0.85\,(17)$ and $a\frac{\partial\kappa}{\partial a} = 0.042\,(9)$ which although have the correct sign, differ from our determined values of $a\frac{\partial\beta}{\partial a} = -0.4826$ and $a\frac{\partial\kappa}{\partial a} = 0.0351$, (where I have removed the factor of $\frac{1}{\beta}$ and $\frac{1}{\kappa}$ that appear in table 3.7). As the determination is centred on an isotropic set, there are a number of relationships that should hold. The derivatives of the input anisotropies with respect

to the measured anisotropy should be around one. We get $\frac{\partial \gamma_g}{\partial \xi_+} = 1.027^{+41}_{-41}$ which is correct within errors and $\frac{\partial \gamma_q}{\partial \xi_+} = 0.146^{+58}_{-56}$ which is surprisingly low. For an isotropic central set, the derivatives of anisotropy with respect to the lattice spacing should be zero. We get $a\frac{\partial \gamma_g}{\partial a} = 0.037^{+49}_{-41}$ which is correct within errors and $a\frac{\partial \gamma_q}{\partial a} = -0.278^{+69}_{-99}$ which is incorrect. The signs of $\frac{\partial \beta}{\partial a}$, $\frac{\partial \beta}{\partial M}$, $\frac{\partial \kappa}{\partial a}$ and $\frac{\partial \kappa}{\partial M}$ are all as expected.

There also exists a relation between the derivative with respect to the anisotropy and the derivative with respect to the lattice spacing. These are valid in the isotropic limit and given by:

$$\left.\frac{\partial \beta}{\partial \xi_+}\right|_{\xi_+=1} = -\frac{a}{4}\frac{\partial \beta}{\partial a}, \qquad \left.\frac{\partial \kappa}{\partial \xi_+}\right|_{\xi_+=1} = -\frac{a}{4}\frac{\partial \kappa}{\partial a}. \tag{3.25}$$

These were given in our paper [68], but mistakenly without the factor of 4. These equations can be derived by:

$$\left.\frac{\partial f}{\partial \xi}\right|_{a_s,M} = \left.\frac{\partial f}{\partial a_\tau}\right|_{a_s,M} \left.\frac{\partial a_\tau}{\partial \xi}\right|_{a_s,M} = \frac{-a_s}{\xi^2}\left.\frac{\partial f}{\partial a_\tau}\right|_{a_s,M}, \tag{3.26}$$

In the isotropic limit, $\xi = 1$ and $a_x = a_y = a_z = a_\tau$, which implies that the function f must be symmetric in a_x, a_y, a_z and a_τ. The derivative of f with respect to the temporal lattice spacing along this isotropic line is then a quarter of the derivative with respect to a. These relations don't hold true for the values given in the table above although they are within 2 sigma, as: $\frac{\partial \beta}{\partial \xi_+} = 0.074^{+32}_{-61}$ while $\frac{-a}{4}\frac{\partial \beta}{\partial a} = 0.121^{+13}_{-13}$. For κ: $\frac{\partial \kappa}{\partial \xi_+} = -0.024^{+14}_{-16}$ and $\frac{-a}{4}\frac{\partial \kappa}{\partial a} = -0.0088^{+12}_{-10}$. As we invert the matrix to obtain the Karsch coefficients, these cannot be used to freeze or isolate terms easily. And it could be argued that if constraints were added in this manner that there is no guarantee that it would give the correct values for all sixteen matrix values.

This raises a question about the initial setup of the determination of Karsch coefficients. In this project we effectively Taylor expanded around an isotropic central set. We can because of the choice of parameters look at a subset of the configuration sets, namely the isotropic sets. The central set could in theory be an anisotropic set, except we would lose this consistency check. The isotropic fit is given below in table 3.11.

c_i	$\frac{a}{c_i^0}\frac{\partial c_i}{\partial a}$	$\frac{M}{c_i^0}\frac{\partial c_i}{\partial M}$
β	$-0.259\,^{+71}_{-82}$	$1.094\,^{+571}_{-251}$
κ	$0.014\,^{+12}_{-9}$	$-0.173\,^{+27}_{-77}$

Table 3.11: Determination carried out on just the isotropic sets. The fits with respect to β have three sample points while the κ fits have four. The dependence of β on the lattice spacing is virtually identical to that of the full determination which is encouraging. The others are almost the same within errors. We again normalise by a factor of the central set parameters.

3.8 Linearity and accuracy of determination

The method we have used to calculate the Karsch coefficients assumed that we were in a linear regime. In principle we could extend this to include higher order terms, but this would require a larger number of sets. Although the Karsch coefficients are determined with what look like respectable error bars, the quality of the determination is a little harder to calculate.

Consider the rather simple example shown below in figure (3.6) of a function $y = f(x)$ with one output parameter y, which depends on one input parameter x, shown as a black line, and the discrete measurement of that function $y_i = f(x_i) + e_m$, where y_i is represented by the blue points and e_m is the sum of various errors from carrying out the measurement shown as error bars. The lines passing through the measured points and the central point are shown in green while the final linear fit is shown in red. The difference between the final fit (red squares) and input measurements (blue circles) gives the severity of the non-linearities. It is also possible to look at the inverse of this relationship between x and y using a function $x = g(y)$.

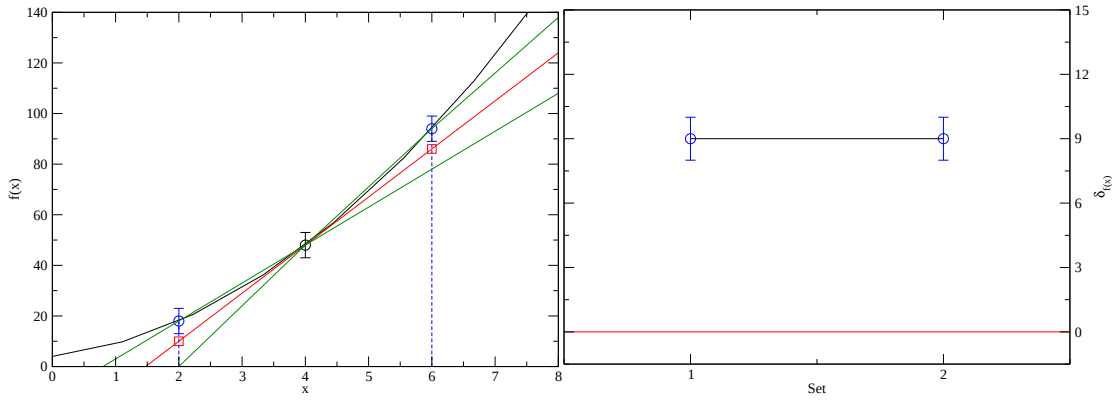

Figure 3.6: Quadratic example. If the curve $f(x)$ is sampled at 3 points and a linear fit is applied (red), although this doesn't fully describe the curve, it does give the correct slope if $f(x)$ is symmetric which is shown by equal values for $\delta_{f(x)}$. The lines shown in green can be thought as being the bounds of the linear fit. The error bars shown are purely for show, in reality they will distort the results.

One immediate observation is that although curvature distorts the fit, the effects may cancel out if the measurements of the surrounding points are symmetric with respect to the linear fit, but higher dimensions and more complicated fitting procedures makes this less clear. If the curvature can be estimated, it may prove useful in the selection of parameters for which curvature effects cancel. The influence of curvature also depends on the distance between the central set and the measured point. On the other hand this would suggest that the plots below do not show the error caused by curvature, rather a bound on the error caused by curvature. This bound is given by the worst case scenario of fitting which can be defined by looking at the simple example above. In that case the derivative at the central point is equal to the slope of the red line $h(x)$ giving:

$$\left.\frac{df}{dx}\right|_{x=4} = \frac{h(6) - h(4)}{6 - 4} \tag{3.27}$$

The slope of $f(x)$ at $x = 6$ is given by:

$$\left.\frac{df}{dx}\right|_{x=6} = \frac{f(6) - f(4)}{6 - 4} = \frac{\delta_f}{6 - 4} + \frac{h(6) - h(4)}{6 - 4} \tag{3.28}$$

which can be generalised to:

$$\frac{\partial f}{\partial x} = \left.\frac{\partial f}{\partial x}\right|_{central} + \frac{\delta}{\eta} \tag{3.29}$$

where δ is defined below as mismatch parameter and η is the distance from the central set. In our case we can use a variant of the Taylor expansion given by equations

(3.2) - (3.5) to measure the curvature of sets used. This allows us to define δ_{input}, and $\delta_{measure}$ in analogy to $y = f(x)$ and $x = g(y)$ for all four input/measurement parameters. Although the Karsch and fit coefficients are defined at the central set, they should give reasonable results for the other sets if the parameters are near enough to the central set, and the coefficient determination is accurate which in turn depends on the accuracy of the initial measurements.

For the following discussion we assume that the measurements are centred on the true value, while in reality the actual value might not even be bounded by the error bars given. In an extreme case the measurements could be incorrect but linear or symmetric which would look correct for the analysis below. These discrepancy functions are defined below in equations (3.30) and (3.33) and are zero for the central set or an ideal linear fit, while it is non-zero for an ideal symmetric non-linear fit and should have the same magnitude and sign. In reality measurement and statistical errors will distort this. The error bars on the following four plots follow the same principle. The error bar with the same colour as the point in question is the best input/measurement value with varying Karsch determination bootstrap values. The second off colour error bar is a combination of varying input/measurement bootstrap values with the best Karsch determination value. The difference between the input parameters and the reconstructed values is defined by δ_{input} below for β:

$$\delta_{input}(\beta) = \frac{a_s^0}{\beta_0}\frac{\partial\beta}{\partial a_s}\frac{\Delta a_s}{a_s^0} + \frac{1}{\beta_0}\frac{\partial\beta}{\partial\xi_+}\Delta\xi_+ + \frac{M_0}{\beta_0}\frac{\partial\beta}{\partial M}\frac{\Delta M}{M_0} + \frac{1}{\beta_0}\frac{\partial\beta}{\partial\xi_-}\Delta\xi_- - \frac{\Delta\beta}{\beta_0}, \quad (3.30)$$

where Δ is the parameter minus the central value, and the zero labels the central set. In figure (3.7), this discrepency is plotted which gives β, γ_g, γ_q, and κ as functions of a_s, ξ_+, m and ξ_-.

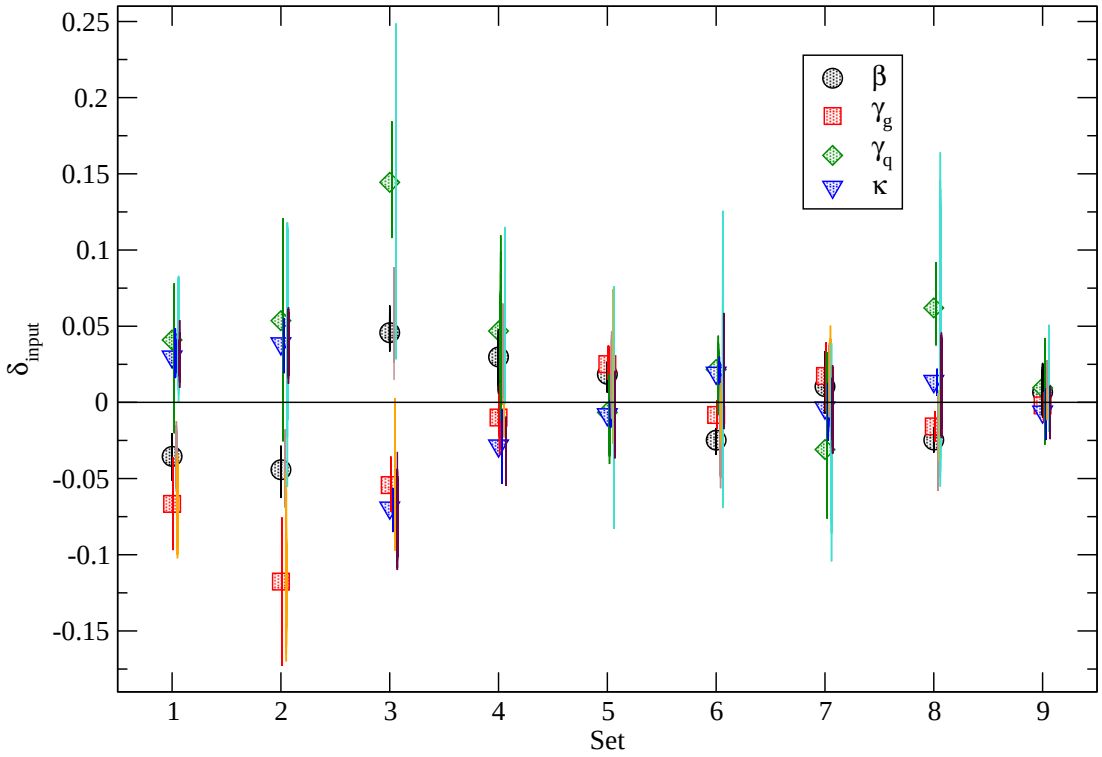

Figure 3.7: Discrepancies δ_{input} of input parameters as functions of measured output.

The error bars suggest that the errors coming from the determination are for the most of similar size to those of the individual measurements. Sets 3 and 8 appear to have larger uncertainties coming from measurements which might be due to the larger error bars on their respective meson dispersion results for M and ξ_q. The largest departures from a perfect match appears to be the anisotropic sets, however the overall effect also depends on the distance to the central set which we define in equation (3.31) below. We plot the discrepency with the following normalisation in figure (3.8).

$$\eta_m = \sqrt{\left(\frac{a_s - a_s^0}{a_s^0}\right)^2 + (\xi_+ - \xi_+^0)^2 + \left(\frac{M - M_0}{M_0}\right)^2 + (\xi_- - \xi_-^0)^2}. \tag{3.31}$$

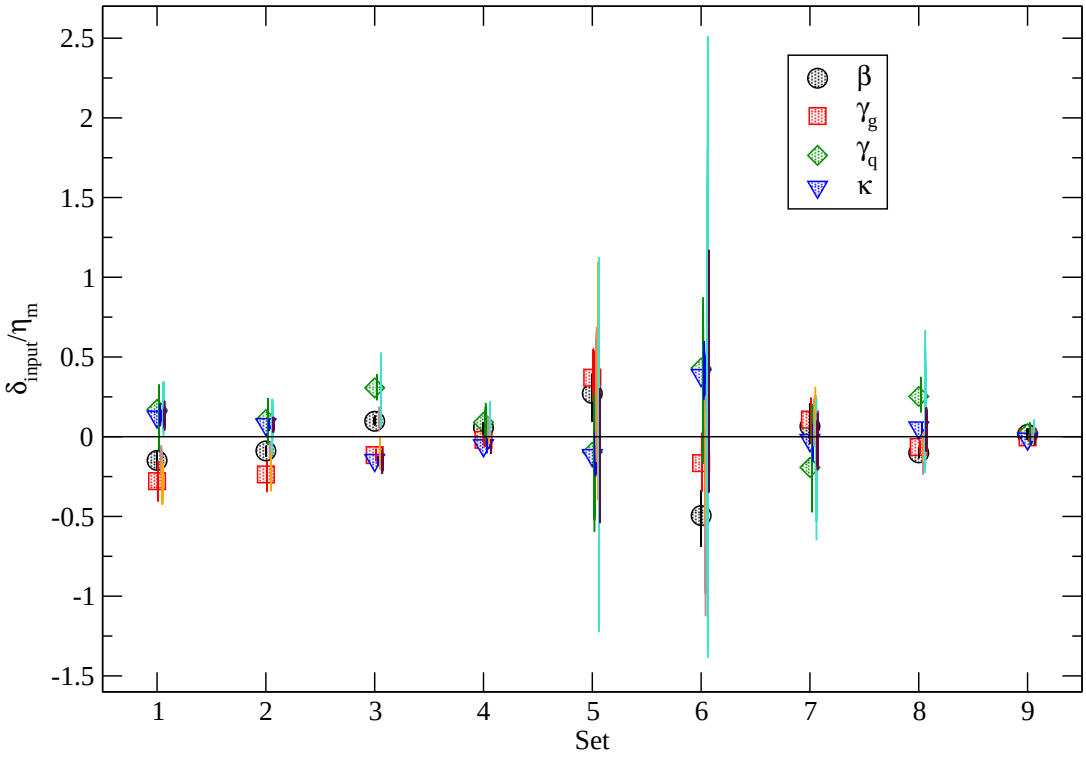

Figure 3.8: Discrepancies in input parameter sets normalised by distance to the central set. This gives a worst case scenario adjustment to the Karsch coefficients from non-linearity and measurement errors.

This is a function of the Karsch coefficients and the measurements of a_s, ξ_+, m and ξ_-. We would expect a reasonable set of data to have a spread of points either side of zero which is the case. After normalisation by η_m given below in table 3.14, the discrepancies for the isotropic sets become larger which point to an unbalanced fit around the anisotropic sets. The normalised discrepancy is an approximation of the change in the the Karsch coefficient. The closer it is to zero, the smaller the total error is. The approximation of the error is given below for $\frac{\partial\beta}{\partial a_s}$.

$$\frac{a_s}{\beta}\left.\frac{\partial\beta}{\partial a_s}\right|_{total} = \frac{a_s}{\beta}\left.\frac{\partial\beta}{\partial a_s}\right|_{fit} + \frac{a_s}{\beta}\frac{\delta\beta}{\eta_m}. \tag{3.32}$$

Below in table (3.12) the Karsch coefficients are given again, this time with the associated curvature/measurement error described above.

c_i	$\frac{a}{c_i^0}\frac{\partial c_i}{\partial a}$	$\frac{1}{c_i^0}\frac{\partial c_i}{\partial \xi_+}$	$\frac{M}{c_i^0}\frac{\partial c_i}{\partial M}$	$\frac{1}{c_i^0}\frac{\partial c_i}{\partial \xi_-}$	Sets $(-,+)$
β	$-0.254\,^{+29(25)}_{-29(46)}$	$0.039\,^{+17(143)}_{-32(260)}$	$0.694\,^{+87(113)}_{-100(207)}$	$0.110\,^{+69(143)}_{-74(260)}$	$6,5$
γ_g	$0.037\,^{+49(66)}_{-41(49)}$	$1.027\,^{+41(370)}_{-41(279)}$	$0.163\,^{+110(294)}_{-130(221)}$	$1.515\,^{+55(370)}_{-84(279)}$	$1,5$
γ_q	$-0.278\,^{+69(77)}_{-99(34)}$	$0.149\,^{+59(431)}_{-58(192)}$	$-0.393\,^{+273(342)}_{-218(153)}$	$-2.378\,^{+174(431)}_{-124(192)}$	$7,6$
κ	$0.209\,^{+29(0.409)}_{-25(0.156)}$	$-0.143\,^{+97(2.295)}_{-83(0.875)}$	$-0.601\,^{+96(1.823)}_{-113(0.695)}$	$0.373\,^{+63(2.295)}_{-69(0.875)}$	$3,6$

Table 3.12: Karsch coefficients with the worst case curvature/measurement error estimate shown in brackets which originate from the sets listed.

The coefficients in the first two columns are used in the thermodynamic calculations. The possible curvature effects are bounded by the values given in brackets. In reality the effect is smaller due to cancellation as shown in figure (3.6), and the effect would be averaged instead of the worst case scenario. The largest error estimates come from fits come from the quark anisotropy data, which points to a need for higher accuracy needed for the meson dispersion. The largest error bars are seen on sets 5 and 6 which may be due to the size of η_m which we list in table 3.14 below. The small size of η_m for those sets suggests they have little effect on the determination which is what we see when we exclude those sets. This is another example of the difficulty in pinpointing the source of errors.

It is also possible to look at the measurements as functions of the inputs. This gives us a reconstruction which directly depends on the fit values, where there is no inversion. After the inversion, errors coming from measurements spread to each coefficient. In figure (3.9) we plot a_s, ξ_+, m and ξ_- as functions of β, γ_g, γ_q, and κ, ie for a_s:

$$\delta_{measure}\left(a_s\right) = a_1\frac{\Delta\beta}{\beta_0} + b_1\Delta\gamma_g + c_1\Delta\gamma_q + d_1\frac{\Delta\kappa}{\kappa_0} - \frac{a_s - a_s^0}{a_s^0}, \tag{3.33}$$

where a_1, b_1, c_1 and d_1 are as defined in the determination.

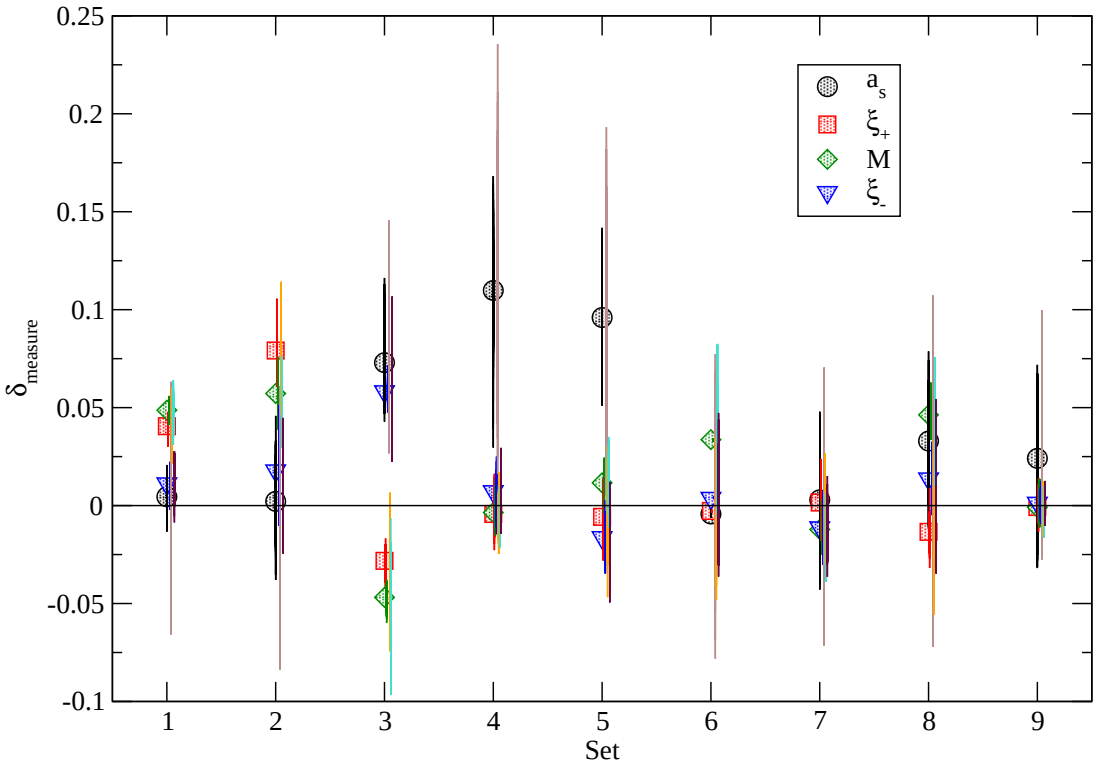

Figure 3.9: Discrepancies $\delta_{measure}$ gives output as functions of input parameters.

This suggests a strong sensitivity of the lattice spacing a_s to the input parameters which agrees with the analysis of the linear fits. Due to the choice of parameters, the fits depend on sets differently. In figure (3.9), point 6 depends only on κ and point 9 only depends on γ_q. All other points depend on two parameters and their respective coefficients. The noisiest sets are 3 and 4 which both depend on a combination of κ and γ_q and set 5 which depends on β and κ.

The overall effect can be determined by dividing by the distance from the central set, in this case for the input parameters:

$$\eta_i = \sqrt{\left(\frac{\beta-\beta_0}{\beta_0}\right)^2 + \left(\gamma_g-\gamma_g^0\right)^2 + \left(\gamma_q-\gamma_q^0\right)^2 + \left(\frac{\kappa-\kappa_0}{\kappa_0}\right)^2}. \tag{3.34}$$

This then gives the error associated with each fit point, for example:

$$\frac{\beta}{a_s}\frac{\partial a_s}{\partial\beta}\bigg|_{total} = \frac{\beta}{a_s}\frac{\partial a_s}{\partial\beta}\bigg|_{fit} + \frac{\beta}{a_s}\frac{\delta a_s}{\eta_i}. \tag{3.35}$$

This is shown below in figure (3.10).

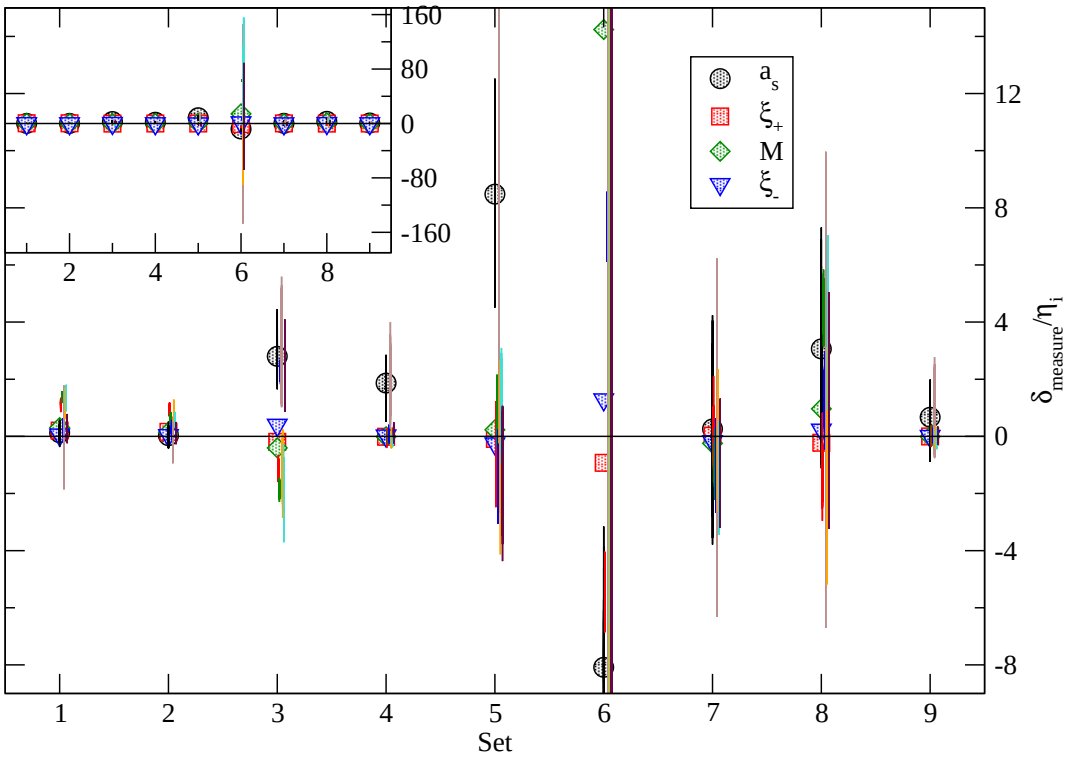

Figure 3.10: This plot demonstrates the dependence on the input parameters. Inset shows the scale of the anomaly at set 6.

Fits are generally better around dominant points resulting in a discrepancy close to zero. Figure (3.10) shows clearly that set 6 has little influence on the fit due to the size of η_i at that point. This also demonstrates the difficulty in identifying the culprit behind a poor fit, whether non-linearities, measurement errors or choice of parameters of a given set.

c_i	$\frac{\beta}{a(M)}a_i\,(\beta)$	$\frac{1}{a(M)}b_i\,(\gamma_g)$	$\frac{1}{a(M)}c_i\,(\gamma_q)$	$\frac{\kappa}{a(M)}d_i\,(\kappa)$	$(-,+)$
a	$-4.830\,^{+159(90.47)}_{-194(86.27)}$	$-0.611\,^{+34(47.61)}_{-27(45.40)}$	$-2.270\,^{+122(47.61)}_{-133(45.40)}$	$-55.198\,^{+1.81(7.99)}_{-1.58(7.63)}$	$6,5$
ξ_+	$-0.688\,^{+68(0.386)}_{-98(1.760)}$	$0.792\,^{+24(0.203)}_{-21(0.927)}$	$0.218\,^{+25(0.203)}_{-29(0.927)}$	$-8.554\,^{+592(0.034)}_{-651(0.1556)}$	$6,1$
M	$-1.086\,^{+62(34.06)}_{-70(0.964)}$	$-0.296\,^{+14(17.93)}_{-14(0.507)}$	$-0.845\,^{+25(17.93)}_{-39(0.507)}$	$-21.259\,^{+561(3.01)}_{-860(0.085)}$	$3,6$
ξ_-	$0.700\,^{+93(2.445)}_{-58(0.486)}$	$0.170\,^{+19(1.287)}_{-17(0.256)}$	$-0.002\,^{+24(1.287)}_{-23(0.256)}$	$9.424\,^{+674(0.216)}_{-511(0.043)}$	$5,6$

Table 3.13: These are the results from the linear fits to equations (3.2) - (3.5), with curvature/measurement error approximations.

Set	η_i	η_m
1	0.199	0.127
2	0.498	0.379
3	0.146	0.456
4	0.331	0.403
5	0.064	0.064
6	0.003	0.050
7	0.064	0.158
8	0.060	0.245
9	0.202	0.468

Table 3.14: Distances η to the central set for input parameters and measurements.

As we have control over the input parameters, it makes sense to have η_i, the distance to the central set, the same. In equations (3.2) - (3.5), the distance is multiplied, meaning that sets further away have more influence which is seen as the low set of errors around sets 1,2,4 and 9. In equations (3.32) and (3.35) the distance is divided giving a large correction from set 6 as it is too close to the central set. In terms of the analysis of possible errors this is clearly the case in figure (3.10). The distance between the measured values and the central set is harder to control. For η_m, the results for the isotropic sets 5 and 6 are an order of magnitude smaller than for the anisotropic sets. Having similar values of η_m would be beneficial, however attaining this requires tuning the input parameters which may unsettle η_i.

The number of sets or data points may also be a factor. With the chosen parameters there are only two linear fits which rely on γ_g and three which depend on γ_q. This is in comparison with five depending on β and six on κ. An increase in the number sets used will also allow for an extension to quadratic terms and more data points which should reduce the influence of troublesome fits and rule out or show any nonlinear behaviour. Omitting one set at a time allows us to determine both the stability of the full determination and the sensitivity to each set. The result of this is shown below in figure (3.11).

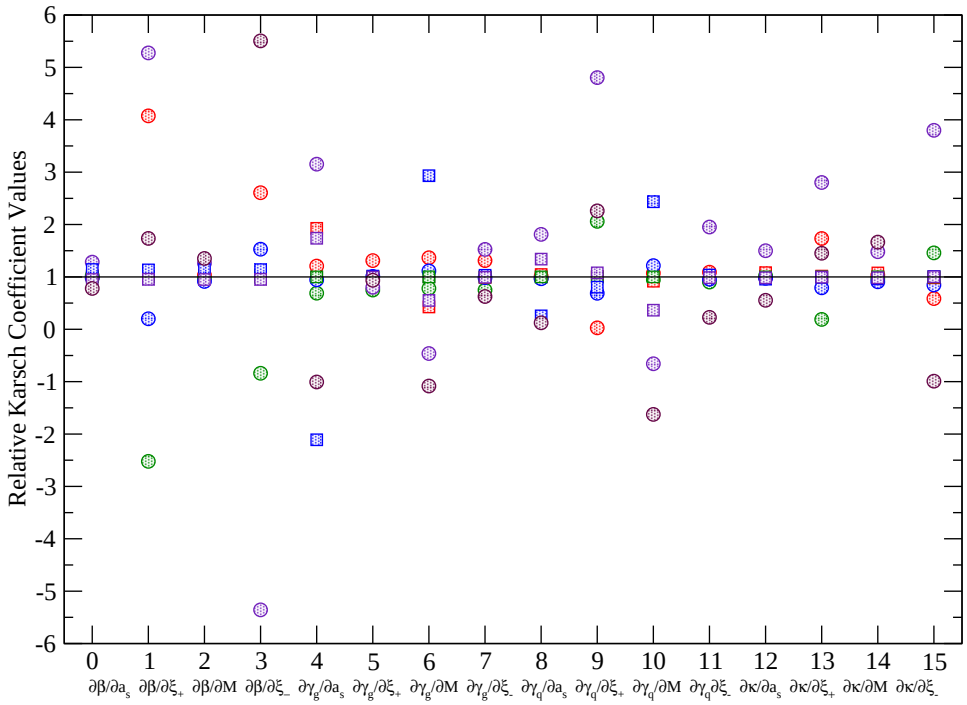

Figure 3.11: Stability of full Karsch coefficients determination is given by comparing the relative difference of the fits omitting each determination set at a time. The Karsch coefficients are normalised as shown in equation (3.6). The results from omitting anisotropic sets are shown as circles while those from the isotropic sets are shown as squares.

We can see that although the lattice spacing appears to be the noisiest measurement, the associated Karsch coefficient is surprisingly stable. The derivatives with respect to the anisotropies ξ_+ and ξ_- appear the least stable which would agree with the opinion that they are the least accurate measurements. The dependence on anisotropic sets is clearly greater than the isotropic sets. An increase in the number of anisotropic sets used and a greater parameter distance between the central set and the isotropic sets would lessen this effect.

3.8.1 Sources of error

The dependence on both the input anisotropy and the measured anisotropy requires more detailed study. An increase in the number of anisotropic sets and an improvement in the measurement of the anisotropy would improve accuracy. For future studies, a more advanced method of selecting simulation parameters which determine the central set and the position of the surrounding sets might become very useful in reducing errors as volume sizes and statistics are increased. There should exist an optimal selection and number of points given a central set of interest.

Choosing parameters such that there is an equal number of sample points for each fit may help distinguish the source of error. Sensitivity to measurement errors

would decrease with increasing distance from the central set, while non-linear effects might increase. However determining these parameters without detailed analysis may prove difficult. In this study the configurations were already generated. In future studies having a method in place to give information during configuration generation may improve selection.

Due to the combination of various steps before the determination, it is hard to pinpoint the largest source of error. The reconstructed values in the previous section gives a non-zero discrepancy, but no clear sign of non-linearity. Reducing any non-linear effect by including higher order terms in the Taylor expansion may prove costly as there would be a need for a larger number of sets, and there is no guarantee that the nonlinear effects are quadratic which would then require terms of even higher order. An increase in the number of sets used is advised.

Increasing the volume will most likely result in better results, reducing systematic effects. The momenta from the meson dispersion rely on the volume, and fitting meson masses at zero and non-zero momenta becomes easier with increased volume as plateaus are easier to identify. Statistical errors are reasonable except for the sideways potential but as mentioned earlier, smearing should improve the signal to noise ratio. Discretisation errors can be seen at increasing distance, but at finer lattice spacing these should lessen. Human errors in putting this system into place and carrying out fits can be reduced by automating the process somewhat by using more advanced measurements. In the case of the lattice spacing and the gauge anisotropy, the Wilson flow as developed by Borsanyi and others [88] removes the visual setting of fit ranges which had up til that point been done by eye which led to errors. With larger and larger data sets moving towards fully automated fitting is a worthwhile objective.

Reducing measurement errors by using more sophisticated techniques such as optimised smearing on larger volumes should greatly improve the accuracy of the determination. A study of the dependence of measured quantities on the input parameters may also reduce determination errors.

4 Physics Results

In this chapter I will cover results for the renormalised energy density, pressure and trace anomaly in two colour QCD. This is done using the derivative method and the Karsch coefficients from the previous chapter. The pressure calculation shown in our published results [68] used the integral method and this allows for some comparison of the methods. I will also briefly look at thermodynamic results at zero chemical potential in SU (3) and analysis of other project work using the SU (2) actions given in chapter 3. I will end with a brief outlook on future work.

4.1 The Equation of State

Using the derivative method, the thermodynamic calculations can be broken into four parts. The first two parts are the derivatives of the gauge action with respect to the anisotropy and the lattice spacing and are given below for the anisotropic Wilson gauge action given in the previous chapter.

$$\left\langle \xi_+ \left.\frac{\partial S_g}{\partial \xi_+}\right|_{a_s,\mu} \right\rangle = -\frac{3}{N_c}\left[\frac{\beta}{\gamma_g}\left\{\frac{1}{\beta}\frac{\partial\beta}{\partial\xi_+} - \frac{1}{\gamma_g}\frac{\partial\gamma_g}{\partial\xi_+}\right\}\langle \mathrm{ReTr}U_{ij}\rangle \right. \tag{4.1}$$
$$\left. +\beta\gamma_g\left\{\frac{1}{\beta}\frac{\partial\beta}{\partial\xi_+} + \frac{1}{\gamma_g}\frac{\partial\gamma_g}{\partial\xi_+}\right\}\langle \mathrm{ReTr}U_{i0}\rangle\right]$$
$$\left\langle a_s \left.\frac{\partial S_g}{\partial a_s}\right|_{\xi_+,\mu} \right\rangle = -\frac{3}{N_c}\left[\frac{\beta}{\gamma_g}\left\{\frac{a_s}{\beta}\frac{\partial\beta}{\partial a_s} - \frac{a_s}{\gamma_g}\frac{\partial\gamma_g}{\partial a_s}\right\}\langle \mathrm{ReTr}U_{ij}\rangle \right. \tag{4.2}$$
$$\left. +\beta\gamma_g\left\{\frac{a_s}{\beta}\frac{\partial\beta}{\partial a_s} + \frac{a_s}{\gamma_g}\frac{\partial\gamma_g}{\partial a_s}\right\}\langle \mathrm{ReTr}U_{i0}\rangle\right]$$

The remaining two parts are the derivatives of the quark action with respect to the anisotropy and the lattice spacing and is given by:

$$\left\langle \xi_+ \left.\frac{\partial S_q}{\partial \xi_+}\right|_{a_s,\mu} \right\rangle = \gamma_q\kappa \left\{ \frac{1}{\gamma_q}\frac{\partial \gamma_q}{\partial \xi_+} + \frac{1}{\kappa}\frac{\partial \kappa}{\partial \xi_+} \right\} \left\langle \bar{\psi} D_0 \psi \right\rangle + \kappa \left\{ \frac{1}{\kappa}\frac{\partial \kappa}{\partial \xi_+} \right\} \sum_i \left\langle \bar{\psi} D_i \psi \right\rangle$$
$$= \kappa \left\{ \frac{1}{\gamma_q}\frac{\partial \gamma_q}{\partial \xi_+} \right\} \left\langle \bar{\psi} D_0 \psi \right\rangle - \left\{ \frac{1}{\kappa}\frac{\partial \kappa}{\partial \xi_+} \right\} \left(\left\langle \bar{\psi}\psi \right\rangle + N_c N_f \right), \tag{4.3}$$

$$\left\langle a_s \left.\frac{\partial S_q}{\partial a_s}\right|_{\xi_+,\mu} \right\rangle = \gamma_q\kappa \left\{ \frac{a_s}{\gamma_q}\frac{\partial \gamma_q}{\partial a_s} + \frac{a_s}{\kappa}\frac{\partial \kappa}{\partial a_s} \right\} \left\langle \bar{\psi} D_0 \psi \right\rangle + \kappa \left(\frac{a_s}{\kappa}\frac{\partial \kappa}{\partial a_s} \right) \sum_i \left\langle \bar{\psi} D_i \psi \right\rangle$$
$$= \kappa \left\{ \frac{a_s}{\gamma_q}\frac{\partial \gamma_q}{\partial a_s} \right\} \left\langle \bar{\psi} D_0 \psi \right\rangle - \left(\frac{a_s}{\kappa}\frac{\partial \kappa}{\partial a_s} \right) \left(\left\langle \bar{\psi}\psi \right\rangle + N_c N_f \right), \tag{4.4}$$

where the following identity [68] was used in the fermion action derivatives to reduce the configuration inputs to $\left\langle \bar{\psi} D_0 \psi \right\rangle$ and $\left\langle \bar{\psi}\psi \right\rangle$, which sees a cancellation of terms when the anisotropy is set to one.

$$\kappa \sum_i \left\langle \bar{\psi} D_i \psi \right\rangle = -4 N_c N_f - \kappa \left\langle \bar{\psi} D_0 \psi \right\rangle - \left\langle \bar{\psi}\psi \right\rangle. \tag{4.5}$$

The gauge contribution to the energy density can now be written:

$$\begin{aligned} \varepsilon_g &= -\frac{\xi_+}{N_s^3 a_s^3 N_\tau a_\tau} \left\langle \frac{\partial S_g}{\partial \xi_+} \right\rangle \\ &= \frac{\xi_+}{N_s^3 a_s^3 N_\tau a_\tau} \frac{3}{N_c} \left[\frac{\beta}{\gamma_g} \left\{ \frac{1}{\beta}\frac{\partial \beta}{\partial \xi_+} - \frac{1}{\gamma_g}\frac{\partial \gamma_g}{\partial \xi_+} \right\} \langle \mathrm{ReTr} U_{ij} \rangle \right. \\ &\qquad \left. + \beta\gamma_g \left\{ \frac{1}{\beta}\frac{\partial \beta}{\partial \xi_+} + \frac{1}{\gamma_g}\frac{\partial \gamma_g}{\partial \xi_+} \right\} \langle \mathrm{ReTr} U_{i0} \rangle \right], \end{aligned} \tag{4.6}$$

where the sums over the spatial and temporal plaquettes are given by the U_{ij} ,U_{i0} terms respectively. The quark contribution to the energy density is given by:

$$\begin{aligned} \varepsilon_q &= -\frac{\xi_+}{N_s^3 a_s^3 N_\tau a_\tau} \left\langle \frac{\partial S_q}{\partial \xi_+} \right\rangle \\ &= \frac{\xi_+}{N_s^3 a_s^3 N_\tau a_\tau} \left[\gamma_q\kappa \left\{ \frac{1}{\gamma_q}\frac{\partial \gamma_q}{\partial \xi_+} \right\} \left\langle \bar{\psi} D_0 \psi \right\rangle - \kappa \left(\frac{1}{\kappa}\frac{\partial \kappa}{\partial \xi_+} \right) \left(\left\langle \bar{\psi}\psi \right\rangle + N_c N_f \right) \right]. \end{aligned} \tag{4.7}$$

The pressure contribution from the gauge sector is given by:

$$
\begin{aligned}
p_g &= \frac{-1}{3N_s^3 a_s^3 N_\tau a_\tau}\left(\xi_+\left\langle\frac{\partial S_g}{\partial \xi_+}\right\rangle + a_s\left\langle\frac{\partial S_g}{\partial a_s}\right\rangle\right) \qquad (4.8)\\
&= \frac{1}{3N_s^3 a_s^3 N_\tau a_\tau}\frac{3}{N_c}\left[\frac{\beta}{\gamma_g}\left\{\frac{a_s}{\beta}\frac{\partial\beta}{\partial a_s}+\frac{1}{\beta}\frac{\partial\beta}{\partial\xi_+}-\frac{a_s}{\gamma_g}\frac{\partial\gamma_g}{\partial a_s}-\frac{1}{\gamma_g}\frac{\partial\gamma_g}{\partial\xi_+}\right\}\langle \mathrm{ReTr}U_{ij}\rangle\right.\\
&\qquad\left.+\beta\gamma_g\left\{\frac{a_s}{\beta}\frac{\partial\beta}{\partial a_s}+\frac{1}{\beta}\frac{\partial\beta}{\partial\xi_+}+\frac{a_s}{\gamma_g}\frac{\partial\gamma_g}{\partial a_s}+\frac{1}{\gamma_g}\frac{\partial\gamma_g}{\partial\xi_+}\right\}\langle \mathrm{ReTr}U_{i0}\rangle\right],
\end{aligned}
$$

and the quark sector by:

$$
\begin{aligned}
p_q &= \frac{-1}{3N_s^3 a_s^3 N_\tau a_\tau}\left(\xi_+\left\langle\frac{\partial S_q}{\partial \xi_+}\right\rangle + a_s\left\langle\frac{\partial S_q}{\partial a_s}\right\rangle\right) \qquad (4.9)\\
&= \frac{1}{3N_s^3 a_s^3 N_\tau a_\tau}\left[\gamma_q\kappa\left\{\frac{1}{\gamma_q}\frac{\partial\gamma_q}{\partial\xi_+}+\frac{a_s}{\gamma_q}\frac{\partial\gamma_q}{\partial a_s}\right\}\left\langle\bar\psi D_0\psi\right\rangle\right.\\
&\qquad\left.-\kappa\left\{\frac{1}{\kappa}\frac{\partial\kappa}{\partial\xi_+}+\frac{a_s}{\kappa}\frac{\partial\kappa}{\partial a_s}\right\}\left(\left\langle\bar\psi\psi\right\rangle+N_cN_f\right)\right].
\end{aligned}
$$

The trace anomaly is given below:

$$
\begin{aligned}
\varepsilon - 3p &= \frac{T}{V}\left\langle a_s\left.\frac{\partial S_q}{\partial a_s}\right|_{\xi_+,\mu}\right\rangle \qquad (4.10)\\
&= \frac{1}{N_s^3 a_s^3 N_\tau a_\tau}\left[-\frac{3}{N_c}\left(\frac{\beta}{\gamma_g}\left\{\frac{a_s}{\beta}\frac{\partial\beta}{\partial a_s}-\frac{a_s}{\gamma_g}\frac{\partial\gamma_g}{\partial a_s}\right\}\langle \mathrm{ReTr}U_{ij}\rangle\right.\right.\\
&\qquad\left.\left.+\beta\gamma_g\left\{\frac{a_s}{\beta}\frac{\partial\beta}{\partial a_s}+\frac{a_s}{\gamma_g}\frac{\partial\gamma_g}{\partial a_s}\right\}\langle \mathrm{ReTr}U_{i0}\rangle\right)\right.\\
&\qquad\left.+\gamma_q\kappa\left\{\frac{a_s}{\gamma_q}\frac{\partial\gamma_q}{\partial a_s}\right\}\left\langle\bar\psi D_0\psi\right\rangle-\kappa\left(\frac{a_s}{\kappa}\frac{\partial\kappa}{\partial a_s}\right)\left(\left\langle\bar\psi\psi\right\rangle+N_cN_f\right)\right].
\end{aligned}
$$

Strictly speaking the energy density, pressure and trace anomaly simplify when the anisotropy is set to one and $\frac{\partial\gamma_g}{\partial a_s}$ and $\frac{\partial\gamma_q}{\partial a_s}$ vanish. However in the determination $\frac{\partial\gamma_q}{\partial a_s}$ does not vanish and its exclusion may or may not counterbalance any change in $\frac{\partial\beta}{\partial a_s}$ or $\frac{\partial\gamma_q}{\partial\xi}$ that would occur if $\frac{\partial\gamma_q}{\partial a_s}$ was zero in the determination. Because of this the full determination below uses the values of the determination as they occur. In any case $\frac{\partial\gamma_q}{\partial a_s}$ comes with a prefactor of κ meaning it does not have a dominant role in the final result. In this particular study the ensembles used for the thermodynamic calculations all have $\kappa = 0.168$.

4.2 Results

Calculating U_{ij}, U_{i0}, $\left\langle \bar{\psi}\psi \right\rangle$ and n_q for each configuration, substituting these values along with the Karsch coefficients determined earlier into the equations for energy density, pressure and trace anomaly and extrapolating to vanishing diquark source $j = 0$, gives us the following plots. The diquark source j controls the diquark action S_J which was introduced earlier in section 3.3. These quantities given above are calculated on configurations with $N_t = 24$, 16, 12, 8 which correspond to temperatures $T = 47$, 70, 94, 141MeV. All of these extrapolation configurations are simulated with the same parameters as the central set given in the previous chapter, $\beta = 1.9$, $\kappa = 0.168$. One practical downside is that as μ increases, especially for values greater than the onset chemical potential $\mu_o \approx \frac{m_\pi}{2} \approx 0.33 a_s^{-1}$, more iterations are needed for the matrix inversion. This is due to a growing density of small eigenvalues of M in the neighbourhood of the origin. The simulation behaviour due to diquark charge j is discussed in [68].

The extrapolation of the total pressure gives a negative value for $\mu < 0.6$ as seen in the top graph of figure 4.1. The value for $a\frac{\partial\beta}{\partial a}$ in the full determination 3.10 is very close to the value in the isotropic subset 3.11. This would suggest that it is a relatively stable value. Even if we set the anisotropy Karsch coefficients equal to the lattice spacing derivatives using the relations 3.25 mentioned in section 3.7:

$$\left.\frac{\partial\beta}{\partial\xi_+}\right|_{\xi_+=1} = -\frac{a}{4}\frac{\partial\beta}{\partial a}, \qquad \left.\frac{\partial\kappa}{\partial\xi_+}\right|_{\xi_+=1} = -\frac{a}{4}\frac{\partial\kappa}{\partial a}. \tag{4.11}$$

we still get negative pressure.

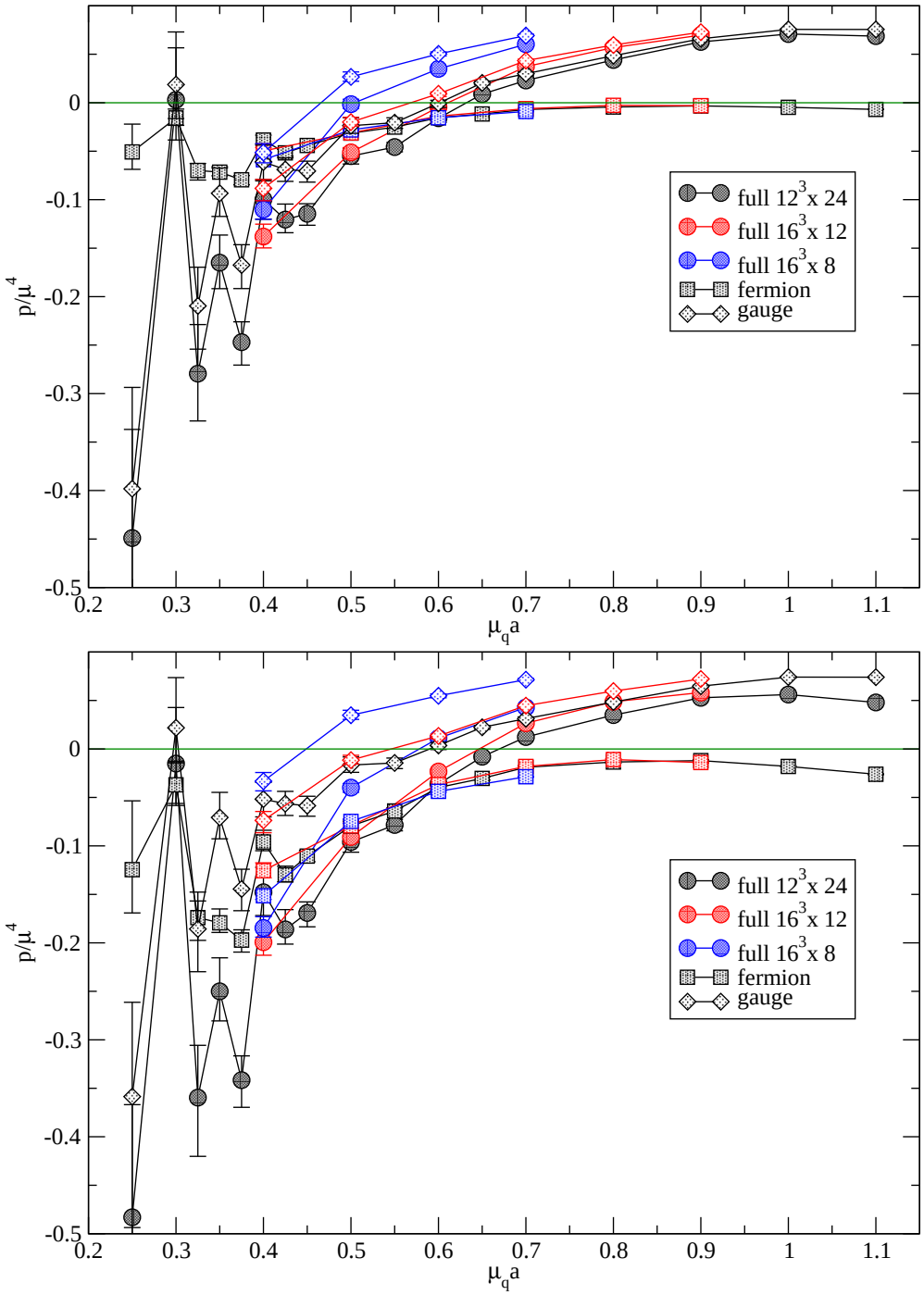

Figure 4.1: Pressure normalised by μ^4 for full determination (top) and using constrained coefficients (bottom). The is little change between the regimes. With dynamical fermions the distinction between the fermion and gauge contributions is no longer clear.

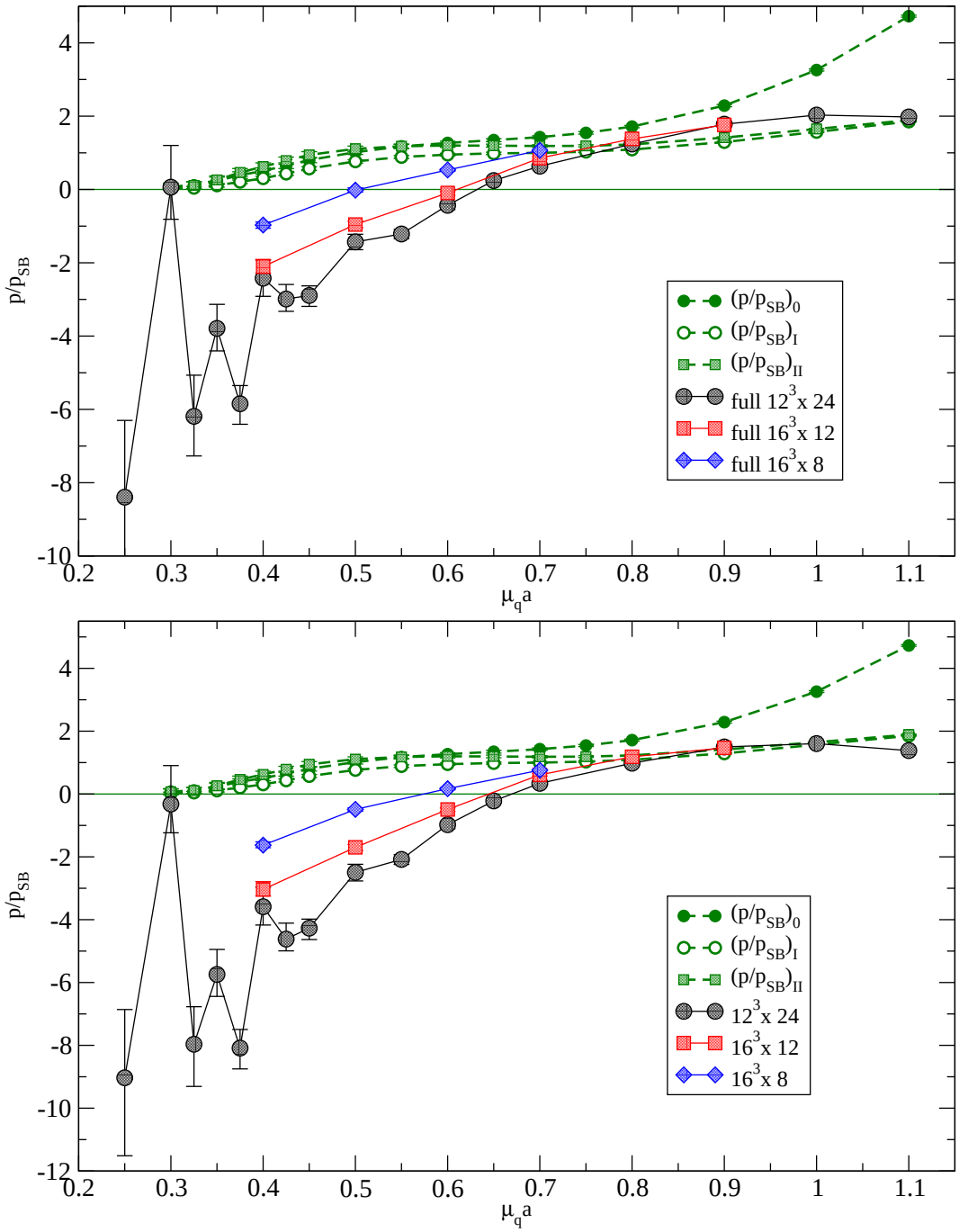

Figure 4.2: Pressure normalised by the continuum Stefan-Boltzmann pressure for a free gas of quarks. Results coming from the integral method calculation are compared with results from derivative method using the full determination (top) and constrained fit (bottom).

It is noticeable that the direct fermion contribution to the pressure is very small for the constrained coefficients, however in all other plots the contribution of the fermion action is roughly equivalent to that of the gauge action. In reality using dynamical fermions means there is no longer a clear distinction in behaviour due to the fermion interaction with the gauge fields.

The three results from the integral method use different means to handle discretisa-

tion effects and are covered in the published paper [68]. $(p/p_{sb})_0$ uses the continuum definition for the Stefan-Boltzmann pressure, $(p/p_{sb})_I$ uses the lattice definition and $(p/p_{sb})_{II}$ uses a combination of the two. To compare the results from the derivative method with the results from the integral method in the paper, we normalise our results by the same lattice definition for the Stefan-Boltzmann pressure used which is given below:

$$p_{SB}^{lattice} = \frac{N_f N_c}{12\pi^2}\left(\mu^4 + 2\pi^2\mu^2 T^2 + \frac{7\pi^4}{15}T^4\right). \tag{4.12}$$

At high values of μ both the full determination and the constrained fit both approach the value given by $(p/p_{sb})_I$ and $(p/p_{sb})_{II}$. The constrained fit is in reasonable agreement for these for most values of μ.

The energy density changes also as a result of the use of constrained coefficients. In the full determination the fermion contribution lessens with increasing μ faster than the gauge contribution crossing each other at $\mu \sim 0.6$. With the constrained coefficients the fermion and gauge contributions are roughly equivalent for most μ. The continuum Stefan-Boltzmann value for the energy density is given as three times the Stefan-Boltzmann pressure defined above in equation 4.12. Using this we get for small T:

$$\frac{\epsilon_{SB}^{cont}}{\mu^4} = \frac{3p_{SB}^{cont}}{\mu^4} \approx 0.1. \tag{4.13}$$

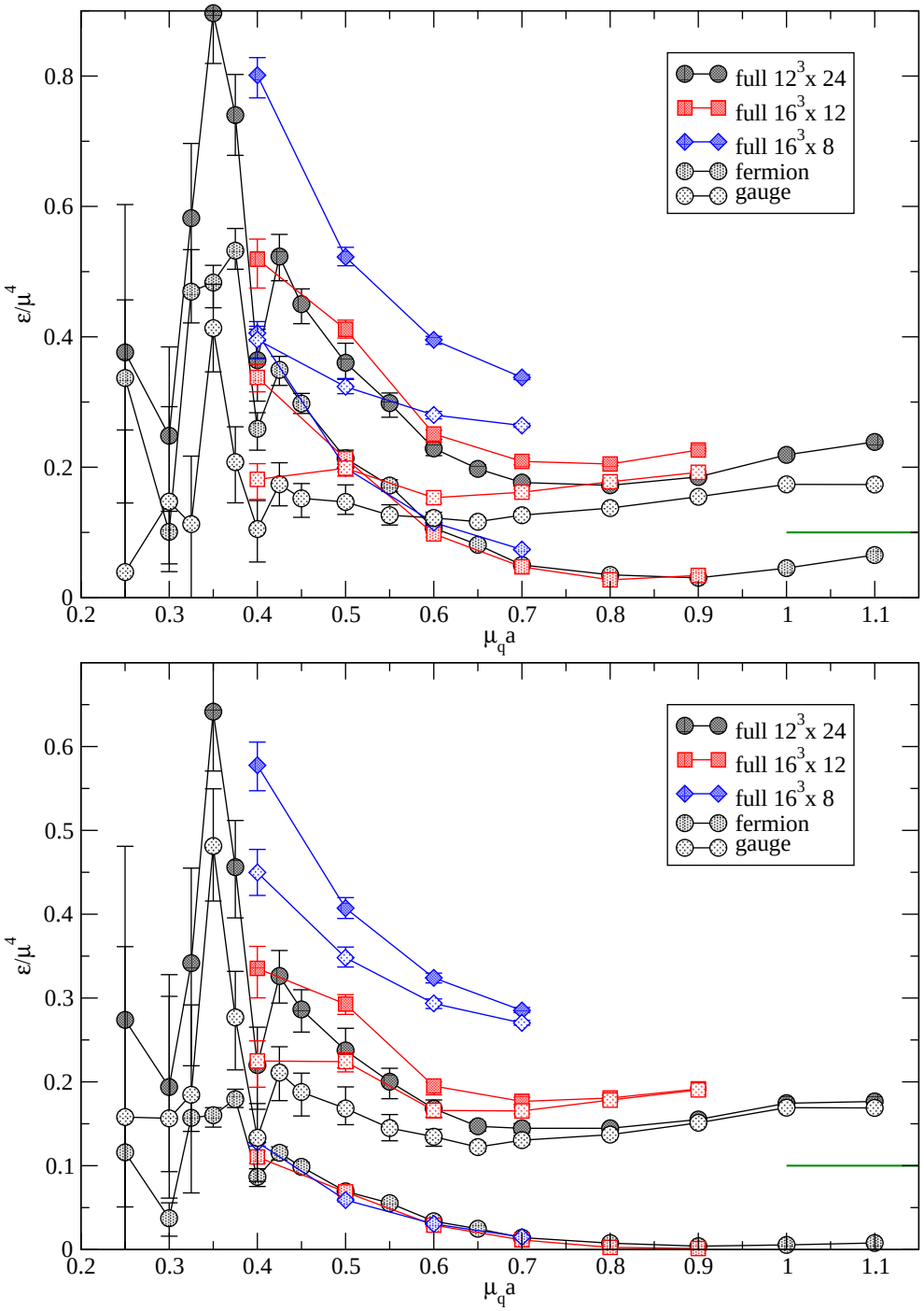

Figure 4.3: Energy density normalised by μ^4 for full determination (top) and using constrained coefficients (bottom). The change in behaviour is a larger spike in the energy density at small μ for the constrained coefficients. At large μ both calculations approach 0.2. The continuum Stefan-Boltzmann value for the energy density normalised by μ^4 is estimated to be 0.1 and is shown in green in bottom right corners.

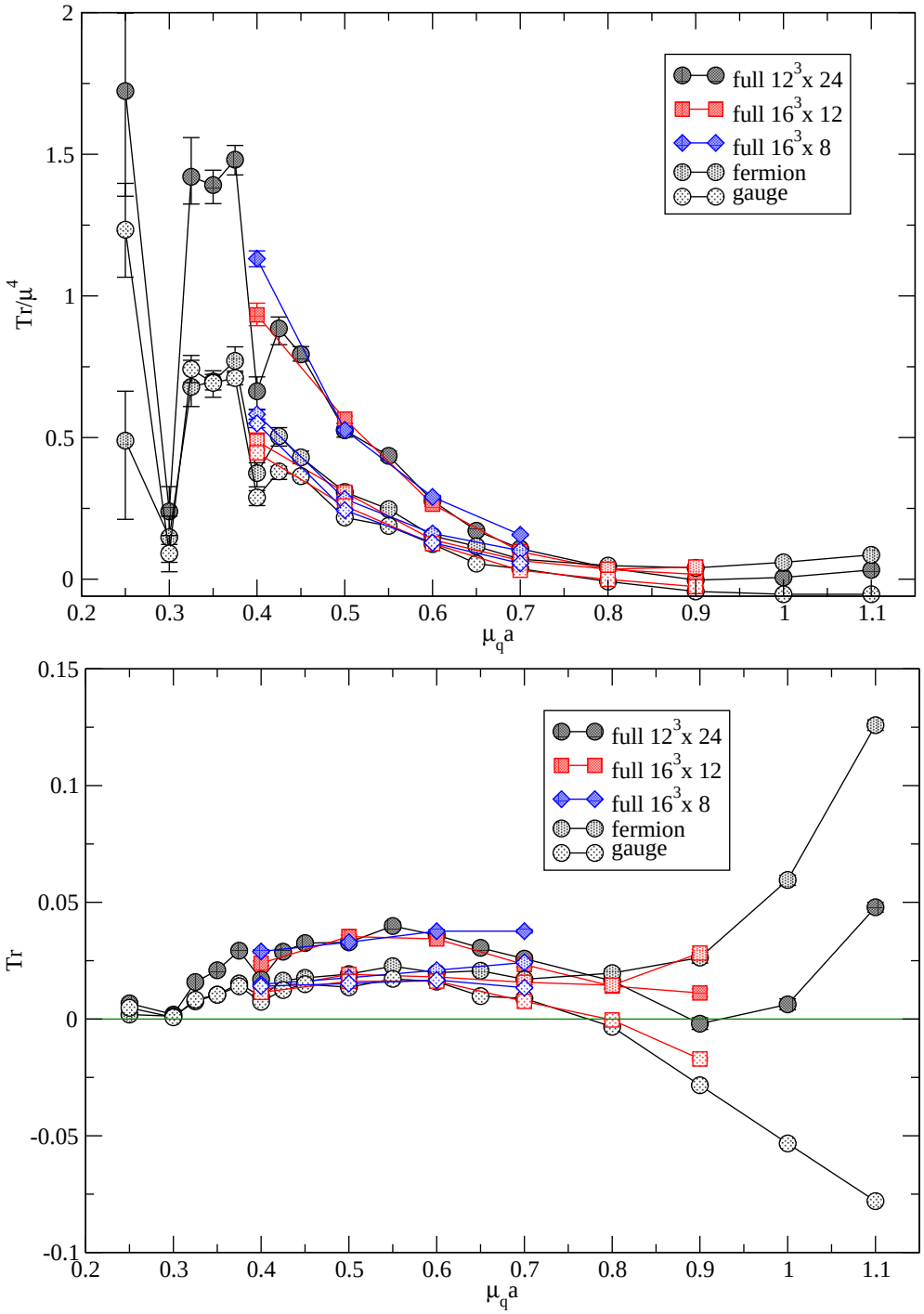

Figure 4.4: Full trace anomaly (bottom) and normalised by μ^4 (top).

The trace anomaly doesn't use any of the constrained coefficients and is shown above moving close to zero for increasing μ for all volumes, which suggests that the SU (2) theory for QCD approaches a conformal theory at large densities. The unrenormalised trace anomaly shown above agrees very well with results from a previous study by the group [64].

4.3 Static quark potential

The static quark potential was used earlier to calculate the lattice spacing a_s in section 3.4. It can also be used to study the behaviour of the string tension for increasing chemical potential and non-zero diquark source. If the distance between a static quark-antiquark pair is increased, we expect at increased distances that the system will produce a new quark-antiquark pair, as it would cost less energy. In the quenched approximation the potential continues to rise linearly at increased distances as there are no dynamical quarks to form a new pair. With dynamical fermions included the potential would in theory reach a plateau instead, which is a sign of the string breaking and screening. At high temperature or high chemical potential the medium may screen or anti-screen colour charge resulting in a change in the string tension.

The configuration sets used to extrapolate the energy density and pressure in section (4.2) are analysed using the static potential code we used in chapter (3) and using an alternative program developed by Alexander Rothkopf [89] [90] [91]. This allows us to compare results and look at diquark and chemical potential dependence of the Wilson loops and Wilson lines. First we model this using our static potential program analysing Wilson loops in two ways, the Cornell potential and a screened Cornell potential

$$V(r) = C(\mu, j) + \sigma(\mu, j)\, r + \frac{\alpha(\mu, j)}{r}. \tag{4.14}$$

$$V(r) = C(\mu, j) + \frac{\sigma(\mu, j)\, r}{B(\mu, j)} e^{-Br} + \frac{\alpha(\mu, j)}{r} e^{-Br}. \tag{4.15}$$

where C is not physically relevant. Figure (4.6) shows results for various values of μ. The exponential term we introduced appears to not be a function of the chemical potential and is non-zero at $\mu = 0$ which would suggest that it is not a mass term.

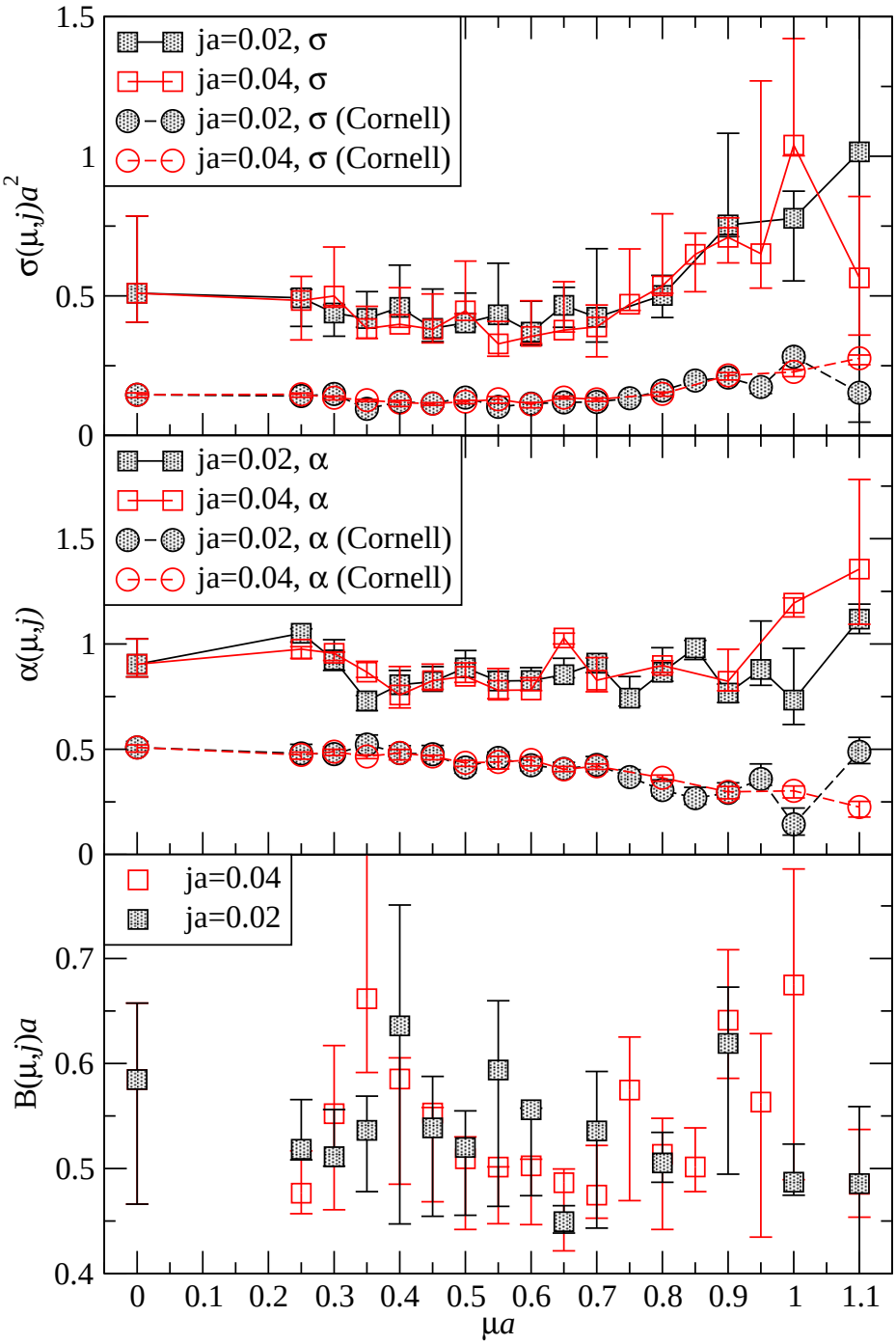

Figure 4.5: Static potential coefficients comparison of the Cornell potential and the screened Cornell potential as a function of chemical potential. The exponential introduced to map screening appears to have no chemical potential dependence.

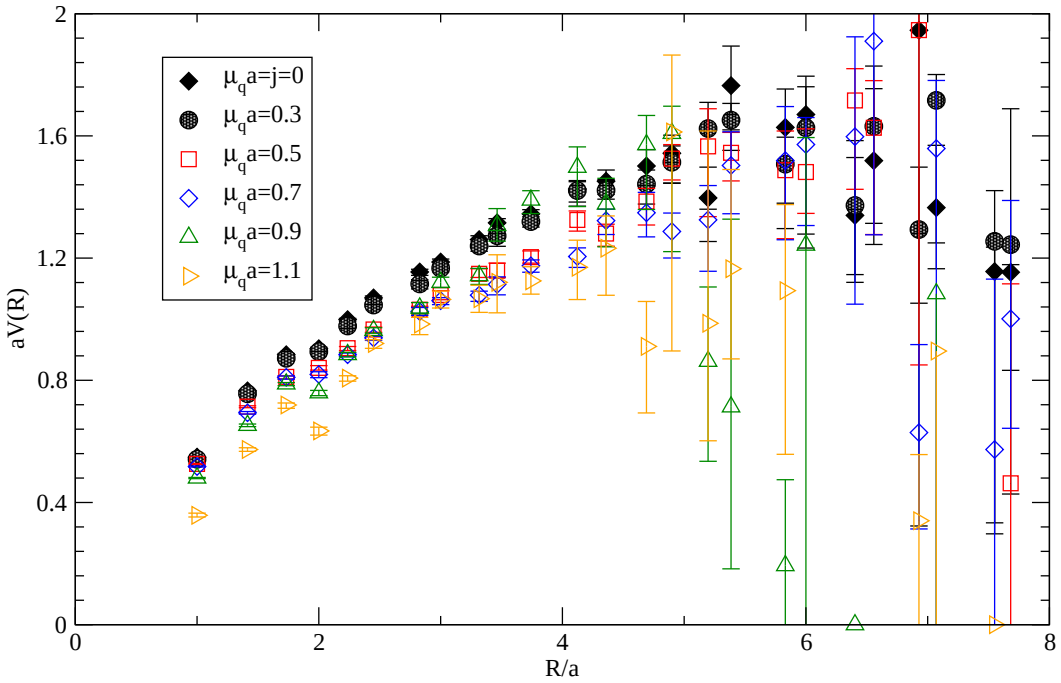

Figure 4.6: Static potential for various chemical potential values at $ja = 0.04$ for 12^3x24 volume.

As the chemical potential rises there is a slight flattening at large distance but no clear sign of string breaking. According to our research from using the Polyakov loop [68], data at $\mu a = 0.9$ should be in the deconfined phase. This work was part of a study on phase transitions [92].

We now look at the results using the same configurations but with software developed by our collaborator Alexander Rothkopf [89]. There are two alternative methods to determine the potential. The first is as mentioned earlier in section 3.4, using a Wilson loop which is gauge invariant. The second is using the Wilson line which is achieved by using Coulomb gauge fixing as it is not gauge invariant. Firstly we can analyse the output of Wilson loops in the same way we did above in figure 4.5. The results are shown below in figure 4.7. In this analysis the exponential term seems nearly constant and is given by $B(\mu, j) \sim 0.46$ while α and σ both rise from around $\mu \sim 0.6$.

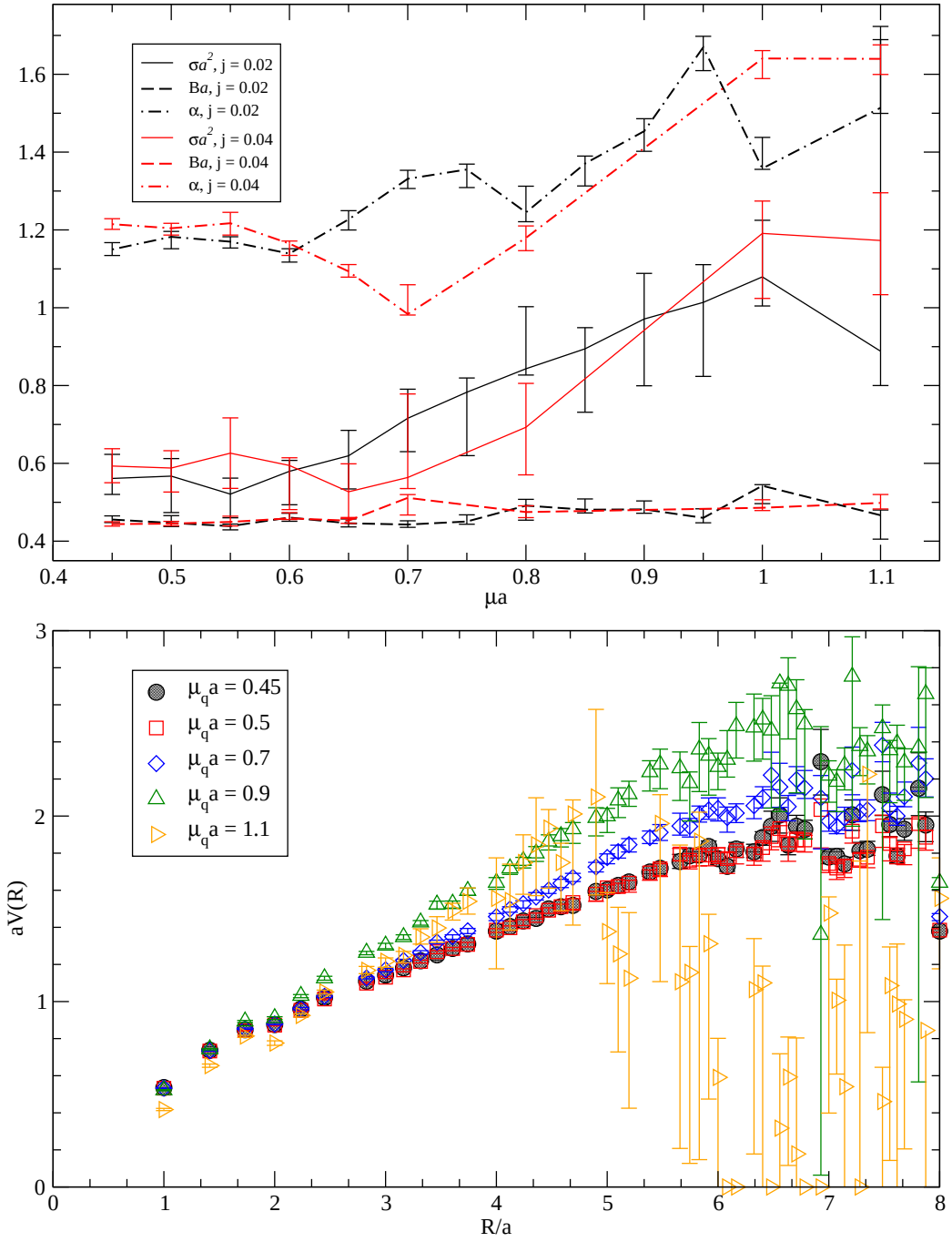

Figure 4.7: Static potential analysis of the 12^3x24 configurations using a program developed by Alexander Rothkopf to calculate Wilson loops, and our existing static potential program to analyse the results. They match up reasonably well will results shown in figures 4.5 and 4.6.

In SU (3), Alexander Rothkopf previously studied the Wilson loop and Wilson line for a range of temperatures. As the Wilson loop or line increases in size the noise increases but at large distances the signal remains and becomes clearer with increasing temperature. In theory this behaviour would also happen for increasing chemical potential but the study is restricted in SU (3) due to the sign problem. In SU (2), we are able to look at these objects and used his program to look for this behaviour on our configurations. At present there are indications of such behaviour, although the

statistical noise is overwhelming. There are plans underway to increase the statistics by generating more configurations and look at other volumes.

Shown below in figures are preliminary raw data from the Wilson loop and Wilson line calculations. Normally the signal at large distances decays into noise and is discarded but a tick shape can be clearly identified for scans at high chemical potential. A decrease in noise is also seen at large distances which is hoped to provide extra information about the behaviour of the potential at non-zero chemical potential. The goal of this project is to analyse both the real and imaginary parts of the potential and examine the spectral functions in line with Alexander Rothkopf's work with Yannis Burnier [93] [94]. The results below are prelimanary but do suggest that the behaviour seen with increasing temperature is also seen with increasing chemical potential and warrants further investigation.

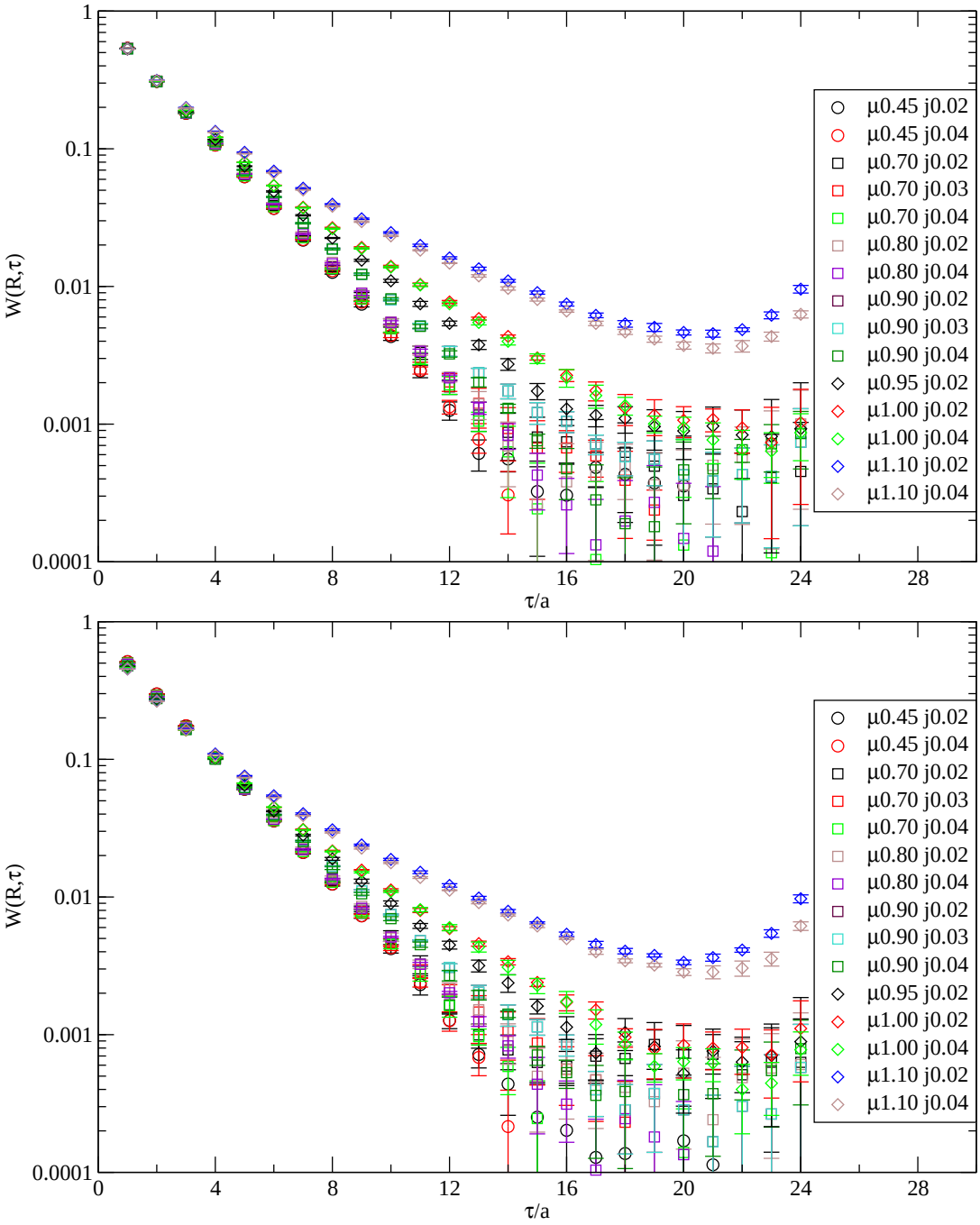

Figure 4.8: Plots for 12^3x24 volume with Wilson loop (top) and Wilson line (bottom) for spatial separation $R = 1$ as a function of the temporal seperation τ.

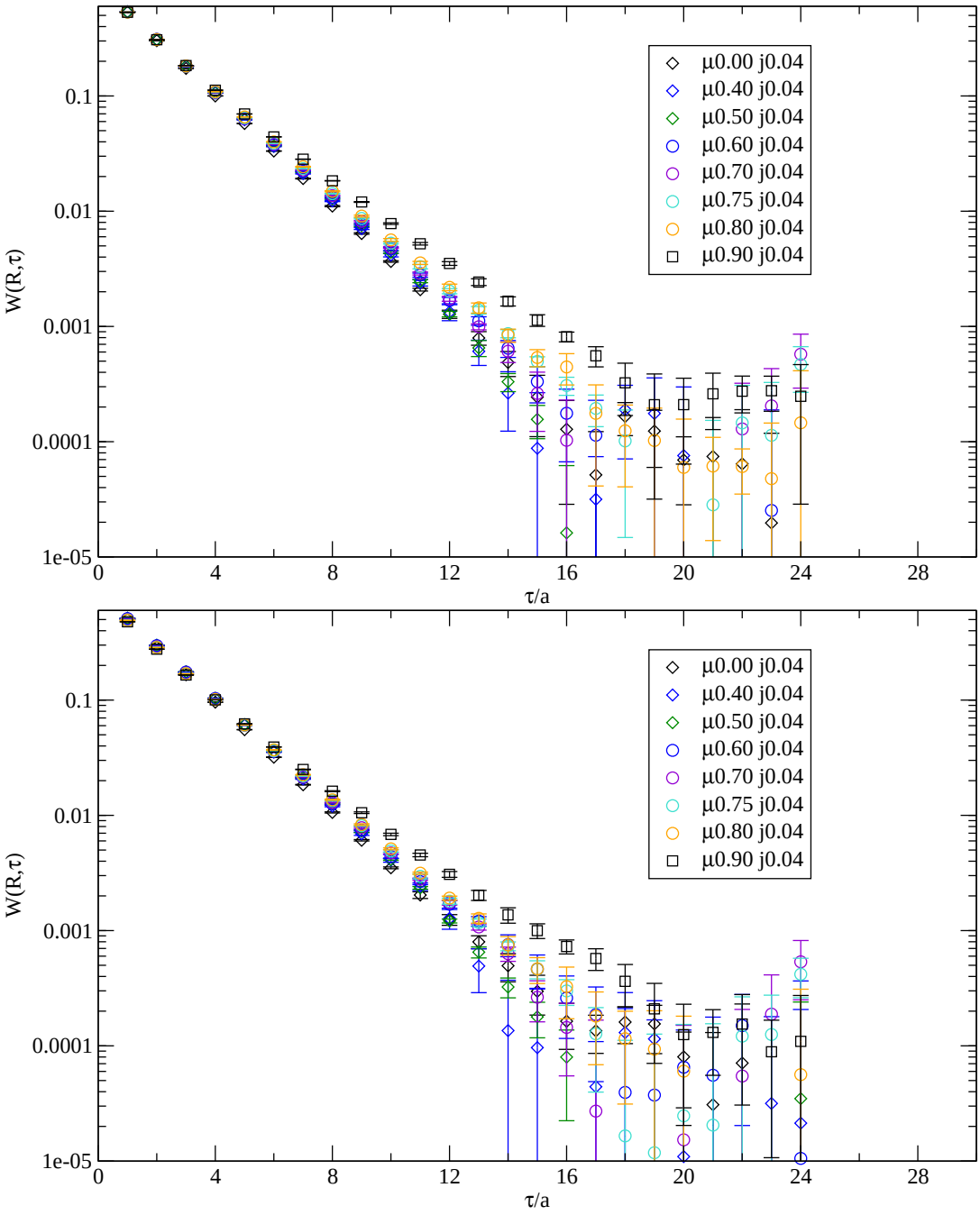

Figure 4.9: Plots for 16^3x24 volume with Wilson loop (top) and Wilson line (bottom) for separation $R = 1$ as a function of the temporal seperation τ.

4.4 SU(3) thermodynamics on anisotropic lattices

In this section we discuss briefly a project on the application of Karsch coefficients in SU(3). This project was carried out before the main determination of the thesis and was a useful introduction to lattice thermodynamics. We used the generated configurations, code and the Karsch coefficients of a previous project by the TrinLat group, namely Richie Morrin, Michael Peardon, Sinead Ryan, Alan O Cais and Jonivar Skullerud [77] [75]. In addition to the configurations already created, we

generated some high temperature configurations to give a more complete picture of the thermodynamics properties of the system.

This project's goal was to use the Karsch coefficients to give results for the equation of state (EoS) for a set of configurations. In this study, a Two-plaquette Symanzik improved (TSI) action was used for the gauge action and it is based in SU (3) which limits the EoS study to zero chemical potential. For these sets of configurations the input anisotropy was tuned to get the appropriate target anisotropy [77]. This is done to ensure that the anisotropy is felt equally in the fermion and gauge sectors, $\xi = \xi_g = \xi_q$, which is necessary to maintain the correct physics. As dynamical quarks are used, this tuning is rather costly as it must simultaneously adjust the values of both ξ_g^0 and ξ_q^0.

The gauge and quark actions used in this project are good examples of the various improvements possible, in this case they are geared towards calculating glueballs. In the gauge action there is now five plaquette terms instead of the one term in the basic isotropic action. The gauge action is given by:

$$\begin{aligned} S_G = \frac{\beta}{\xi_g^0}\left\{\frac{5\left(1+\omega\right)}{3u_s^4}\Omega_s - \frac{5\omega}{3u_s^8}\Omega_s^{(2t)} - \frac{1}{12u_s^6}\Omega_s^{(R)}\right\} \\ + \beta\xi_g^0\left\{\frac{4}{3u_s^2u_t^2}\Omega_t - \frac{1}{12u_s^2u_t^2}\Omega_t^{(R)}\right\}, \end{aligned} \tag{4.16}$$

where Ω_s and Ω_t are spatial and temporal plaquettes. $\Omega_s^{(R)}$ and $\Omega_t^{(R)}$ are 2×1 rectangles in the (i, j) and (i, t) planes. $\Omega_s^{(2t)}$ is a combination of two plaquettes separated by a single temporal link. The parameters are $\beta = 1.508$, $\xi_g^0 = 8.42$ and $\omega = 3$. The mean field value for the spatial directions was determined to be $u_s = 0.32$ while the temporal direction mean field value u_t is set by convention to 1. It has leading order discretisation errors of $O\left(a_s^3, a_t, \alpha_s a_s\right)$. This equation can be rewritten as a function of the parameters that the Karsch coefficients act on. This gives

$$S_g = A_g\Omega_s - B_g\Omega_s^{(2t)} - C_g\Omega_s^{(R)} - D_g\Omega_t^{(R)} + E_g\Omega_t. \tag{4.17}$$

The quark action used is the ARIA action (Anisotropic Rotated Improved Action) [95] which is $O\left(a_s^3, a_t\right)$ improved and designed for highly anisotropic lattices $\xi > 5$. A

rotation term is applied to the temporal direction, while irrelevant terms are added to the spatial directions to remove the doublers and avoid a $O\left(a_s m_q\right)$ error. The quark action can be written as $S_q = \bar{\psi} M \psi$ where

$$\begin{aligned} M\psi\left(x\right) =& \frac{1}{a_t}\left(m_0 a_t + r + \frac{18s}{\xi_q^0}\right)\psi\left(x\right) \\ &+ \frac{1}{a_t}\frac{1}{2u_t}\left[\left(\gamma_0 - r\right)U_t(x)\psi\left(x+\hat{t}\right) - \left(\gamma_0 + r\right)U_t^{\dagger}\left(x-\hat{t}\right)\psi\left(x-\hat{t}\right)\right] \\ &+ \frac{1}{a_t}\frac{1}{\xi_q^0}\frac{1}{u_s}\sum_i\left[\left(\frac{2}{3}\gamma_i - 4s\right)U_i\left(x\right)\psi\left(x+\hat{i}\right)\right. \\ &\qquad\left. - \left(\frac{2}{3}\gamma_i + 4s\right)U_i^{\dagger}\left(x-\hat{i}\right)\psi\left(x-\hat{i}\right)\right] \\ &- \frac{1}{a_t}\frac{1}{\xi_q^0}\frac{1}{u_s^2}\sum_i\left[\left(\frac{1}{12}\gamma_i - s\right)U_i\left(x\right)U_i\left(x+\hat{i}\right)\psi\left(x+2\hat{i}\right)\right. \\ &\qquad\left. - \left(\frac{1}{12}\gamma_i + s\right)U_i^{\dagger}\left(x-\hat{i}\right)U_i^{\dagger}\left(x-2\hat{i}\right)\psi\left(x-2\hat{i}\right)\right], \end{aligned} \tag{4.18}$$

which as far as the derivative method and the Karsch coefficients are concerned looks like this where A_q, B_q and C_q are used to show the added Karsch coefficient dependence of this action:

$$\begin{aligned} M\psi\left(x\right) =& \frac{1}{a_t}\left\{m_0 a_t \psi\left(x\right) + r\psi\left(x\right) + \frac{18s}{\xi_q^0}\psi\left(x\right)\right. \\ &\left. + \frac{1}{2u_t}A_q + \frac{1}{\xi_q^0}\frac{1}{u_s}B_q - \frac{1}{\xi_q^0}\frac{1}{u_s^2}C_q\right\}. \end{aligned} \tag{4.19}$$

where the Wilson parameter $r = 1$ gets rid of temporal doubler terms and the Hamber-Wu [96] parameter $s = \frac{1}{8}$ gets rid of spatial doubler terms. The derivative of this function with respect to the measured quantities ξ_+, ξ_-, a_s, M and u_s, can be written as a multiplicative renormalisation of the original equation by the Karsch coefficients. The partial derivative of the gauge action $S_g\left(\beta, \xi_g^0, u_s\right)$ with respect to a dependent variable denoted by x is:

$$
\begin{aligned}
\frac{\partial S_g}{\partial x} &= \frac{\beta}{\xi_g^0}\frac{5\left(1+\omega\right)}{3u_s^4}\left\{\frac{1}{\beta}\frac{\partial\beta}{\partial x}-\frac{1}{\xi_g^0}\frac{\partial\xi_g^0}{\partial x}-\frac{4}{u_s}\frac{\partial u_s}{\partial x}\right\}\Omega_s \\
&\quad -\frac{\beta}{\xi_g^0}\frac{5\omega}{3u_s^8}\left\{\frac{1}{\beta}\frac{\partial\beta}{\partial x}-\frac{1}{\xi_g^0}\frac{\partial\xi_g^0}{\partial x}-\frac{8}{u_s}\frac{\partial u_s}{\partial x}\right\}\Omega_s^{(2t)} \\
&\quad -\frac{\beta}{\xi_g^0}\frac{1}{12u_s^6}\left\{\frac{1}{\beta}\frac{\partial\beta}{\partial x}-\frac{1}{\xi_g^0}\frac{\partial\xi_g^0}{\partial x}-\frac{6}{u_s}\frac{\partial u_s}{\partial x}\right\}\Omega_s^{(R)} \\
&\quad -\beta\xi_g^0\frac{1}{12u_s^4u_t^2}\left\{\frac{1}{\beta}\frac{\partial\beta}{\partial x}+\frac{1}{\xi_g^0}\frac{\partial\xi_g^0}{\partial x}-\frac{2}{u_s}\frac{\partial u_s}{\partial x}\right\}\Omega_t^{(R)} \\
&\quad +\beta\xi_g^0\frac{4}{3u_s^2u_t^2}\left\{\frac{1}{\beta}\frac{\partial\beta}{\partial x}+\frac{1}{\xi_g^0}\frac{\partial\xi_g^0}{\partial x}-\frac{4}{u_s}\frac{\partial u_s}{\partial x}\right\}\Omega_t.
\end{aligned}
\tag{4.20}
$$

The bracketed terms are the Karsch coefficients, which in this case were calculated by the Trinlat group in [75]. The derivative of any action can be written in terms of the original prefactors. In this case the derivative of the gauge action is written as the original prefactors multiplied by a function of the Karsch coefficients multiplied by the respective plaquette sums Ω.

$$
\begin{aligned}
\frac{\partial S_g}{\partial x} &= A_g\left\{...\right\}\Omega_s - B_g\left\{...\right\}\Omega_s^{(2t)} - C_g\left\{...\right\}\Omega_s^{(R)} \\
&\quad - D_g\left\{...\right\}\Omega_t^{(R)} + E_g\left\{...\right\}\Omega_t.
\end{aligned}
\tag{4.21}
$$

The constants A_g,B_g,C_g,D_g and E_g are known from the gauge action parameters and the Ω terms were calculated configuration by configuration. For the quark action, the partial derivative with respect to the dependent variable x becomes

$$
\begin{aligned}
\frac{\partial\left(a_tM\psi\left(x\right)\right)}{\partial x} &= \left\{\frac{1}{m_0}\frac{\partial m_0}{\partial x}+\frac{1}{a_t}\frac{\partial a_t}{\partial x}\right\}\left(m_0a_t\right)\psi\left(x\right) \\
&\quad +\left\{-\frac{1}{\xi_q^0}\frac{\partial\xi_q^0}{\partial x}\right\}\left(\frac{18s}{\xi_q^0}\right)\psi\left(x\right) \\
&\quad +\left\{-\frac{1}{\xi_q^0}\frac{\partial\xi_q^0}{\partial x}-\frac{1}{u_s}\frac{\partial u_s}{\partial x}\right\}\frac{1}{\xi_q^0}\frac{1}{u_s}B_q \\
&\quad -\left\{-\frac{1}{\xi_q^0}\frac{\partial\xi_q^0}{\partial x}-\frac{1}{u_s}\frac{\partial u_s}{\partial x}\right\}\frac{1}{\xi_q^0}\frac{1}{u_s^2}C_q.
\end{aligned}
\tag{4.22}
$$

In a similar fashion to the gauge action, terms with a parameter variable pick up a multiplicative renormalisation. As there is no factor of ξ_g^0 or u_s dependence in the temporal bracket A_q, it vanishes in the derivative.

The TrinLat group compared the setup we used in equations 3.2 - 3.5, and the setup used by Levkova [74]. For that method they compared fixing u_s and β alternatively as they are dependent on each other. This is an example of the additional measurements and additional work needed to determine the Karsch coefficients when using improved actions.

We carried out the fits shown below in figure 4.10 using their configuration data and the values for the Karsch coefficients given in Richie Morrin's thesis [75]. The fits have an upper bound and lower bound coming from the error bars listed in that thesis. For a full picture the original bootstrapped values of the Karsch coefficient determination are needed. As this was deemed a minor project we were satisfied to use the values quoted. A similar approach is possible for the quark sector as explained above, but was not carried out due to time constraints. As these simulations used dynamical quarks, the fermion sector results are needed to make any meaningful comparisons.

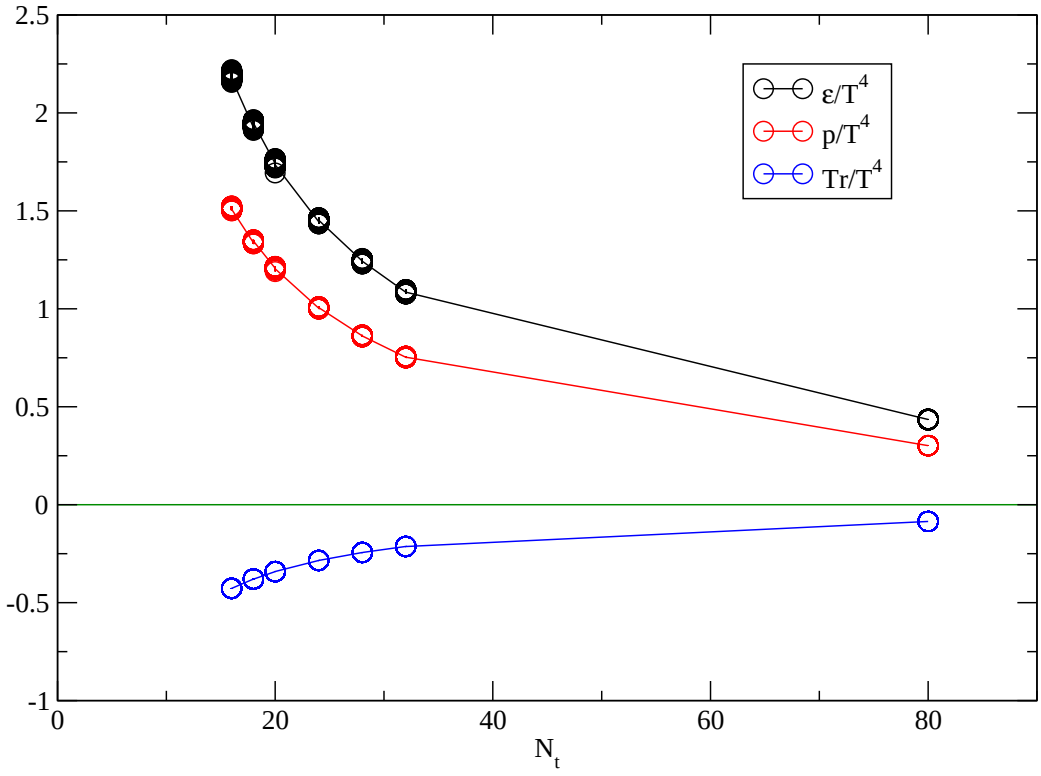

Figure 4.10: Pressure, energy density and trace anomaly contributions from the gauge sector.

4.5 Summary and Outlook

The derivative method with non-perturbatively determined Karsch coefficients is an alternative solution to calculating thermodynamical quantities on the lattice but a number of issues remain. In particular, the negative pressure seen in figures 4.1 and 4.2 for low μ suggests that the Karsch coefficients have not yet been determined with sufficient accuracy. Errors in measuring lattice properties are an issue but I have argued that lattice volume, lattice spacing, parameter choice and the number of determination sets all play a role. On larger volumes with smaller lattice spacings the cost will increase, but so will the accuracy. It may be the case that for certain parameters, volumes and lattice scales the derivative method would be a more appropriate choice than the integral method. If the accuracy is improved the ability to perform a Karsch coefficient determination at zero chemical potential on a cold lattice would give enough information to perform any number of temperature and density scans.

The fits rely on statistics at a handful of points to determine coefficients $a_1, ..., a_4, b_1, ..., d_4$ in equations (3.2) - (3.5). A study on how best to initially determine these points may increase effectiveness and reduce errors. Obviously increasing the number of these points will give a better fit. The choice of quark and gauge action also plays a role. As pointed out in section 5.1 the added number of parameters increases the complexity of the determination which would further increase the number of data points needed. In theory the increase in accuracy will outstrip the increased computational cost. For anisotropic lattices, the derivative method is better suited and on state of the art lattices $a < 0.1$fm, we would expect better results.

The overall setup of this project relies on a central set and several neighbouring sets which allow us to determine the value of the derivatives for the parameters of the central set. Improving the selection process of these parameters to optimise results with limited number of neighbouring determination sets should also reduce errors. Replicating results for a subset of coefficients on a group of isotropic ensembles should also be seen as a test of reduced errors.

During the course of the determination of the Karsch coefficients, a number of projects were sidelined due to problems with the code or time constraints. These included improving the sideways potential implementation by adding more complex loops and smearing. An alternative to this was to consider the w_0 scale from the Wilson flow, which is based on work by Luscher [97] and has been implemented successfully in SU (3) by Borsanyi et al [80], to calculate the lattice spacing a_s and

the gauge anisotropy ξ_g. Adapting the code to run on SU (2) configurations would in principle replace the current static quark potential and sideways potential codes in terms of speed and accuracy.

We have planned a determination of Karsch coefficients in SU (3)and measurements are already under way. These new data sets will provide a temperature scan at zero chemical potential and will be used by other members of the group on future projects. The analysis of non-linearities and parameter setup of these new data sets will hopefully give information about the source of errors.

Acknowledgments

I would like to thank first and foremost my supervisor Jon-Ivar Skullerud, for his patience, help, knowledge and giving me this opportunity. Secondly my parents, Angela and Senan who have always supported me throughout my education, and my brothers Brendan and Eamonn for all their encouragement. Next I would like to thank everyone in the Mathematical Physics department, past and present, Dhagash, Glen, Aoife, Anne, Robert, Jørgen, Tamer, Sepanda, Niall, Ahmed, Billy, Paul, Brian, Charles, Jiri, Joost, Danny, Monica, Tigran.

I would also like to thank staff at Trinity College Dublin, especially Mike and Sinead. I would also like to thank our collaborators Simon, Seyong and Pietro.

Finally I would like to thank all the friends I have made over the years who supported me including Darren, Colin, Rory, Connor, Phil, Tracy, Tom, John, Brendan, Gabh and Enda.

5 Appendix

5.1 Computation specifications

Vendor	Intel
CPU Speed	2992.48MHz
Architecture	i686
Number of cores	2
L1d cache	16K
L2 cache	1024K
RAM	978Mb

Table 5.1: Workstation Specifications

Bibliography

[1] Kenneth G. Wilson. Confinement of Quarks. *Phys.Rev.*, D10:2445–2459, 1974.

[2] Michael Creutz. Confinement, chiral symmetry, and the lattice. *Acta Phys.Slov.*, 61:1–127, 2011.

[3] Kazuyuki Kanaya. An Introduction to finite temperature quantum chromodynamics on the lattice. *Prog.Theor.Phys.Suppl.*, 131:73–105, 1998.

[4] Uwe-Jens Wiese. An introduction to lattice field theory. *Online notes: http://www.itp.uni-hannover.de/saalburg/Lectures/wiese.pdf*, 2009.

[5] Holger Bech Nielsen and M. Ninomiya. No Go Theorem for Regularizing Chiral Fermions. *Phys.Lett.*, B105:219, 1981.

[6] John Kogut and Leonard Susskind. Hamiltonian formulation of wilson's lattice gauge theories. *Physical Review D*, 11(2):395–408, jan 1975.

[7] Michael Creutz. Chiral anomalies and rooted staggered fermions. *Phys.Lett.B*, 649:230-234,2007, Phys.Lett.B649:230-234,2007.

[8] Paul H. Ginsparg and Kenneth G. Wilson. A remnant of chiral symmetry on the lattice. *Physical Review D*, 25(10):2649–2657, may 1982.

[9] David B. Kaplan. A method for simulating chiral fermions on the lattice. *Physics Letters B*, 288(3-4):342–347, aug 1992.

[10] Rajamani Narayanan and Herbert Neuberger. Chiral Determinant as an Overlap of Two Vacua. *Nucl.Phys. B*, 412:574–606, 1994.

[11] Roberto Frezzotti, Pietro Antonio Grassi, Stefan Sint, and Peter Weisz. Lattice QCD with a chirally twisted mass term. *JHEP*, 0108:058,2001, JHEP 0108:058,2001.

[12] G. Burgers, F. Karsch, A. Nakamura, and I.O. Stamatescu. QCD on anisotropic lattices. *Nucl.Phys.*, B304:587, 1988.

[13] Rajan Gupta. Introduction to lattice QCD: Course. In *Probing the standard model of particle interactions. Proceedings, Summer School in Theoretical Physics, NATO Advanced Study Institute, 68th session, Les Houches, France, July 28-September 5, 1997. Pt. 1, 2*, pages 83–219, 1997.

[14] K. Symanzik. Continuum limit and improved action in lattice theories. *Nuclear Physics B*, 226(1):187–204, sep 1983.

[15] B. Sheikholeslami and R. Wohlert. Improved continuum limit lattice action for QCD with wilson fermions. *Nuclear Physics B*, 259(4):572–596, sep 1985.

[16] Owe Philipsen. The QCD equation of state from the lattice. *Prog.Part.Nucl.Phys.*, 70:55–107, 2013.

[17] G. Peter Lepage and Paul B. Mackenzie. Viability of lattice perturbation theory. *Physical Review D*, 48(5):2250–2264, sep 1993.

[18] V. Lubicz. Quark masses on the lattice: Light and heavy. *Nucl. Phys. Proc. Suppl.*, 94:116–129, 2001. [,116(2000)].

[19] Z. Fodor, C. Hoelbling, S. Krieg, L. Lellouch, Th. Lippert, A. Portelli, A. Sastre, K. K. Szabo, and L. Varnhorst. Up and down quark masses and corrections to Dashen's theorem from lattice QCD and quenched QED. 2016.

[20] N. & others Carrasco. Up, down, strange and charm quark masses with nf = 2+1+1 twisted mass lattice qcd. *Nuclear Physics B*, 887:19–68, oct 2014.

[21] Massimo Di Pierro. From Monte Carlo integration to lattice quantum chromodynamics: An Introduction. In *GSA Summer School on Physics on the Frontier and in the Future Batavia, Illinois, July 31-August 7, 2000*, 2000.

[22] N. Metropolis, A. W. Rosenbluth, M. N. Rosenbluth, A. H. Teller, and E. Teller. Equation of state calculations by fast computing machines. *J. Chem. Phys.*, 21:1087–1092, 1953.

[23] S. Duane, A. D. Kennedy, B. J. Pendleton, and D. Roweth. Hybrid Monte Carlo. *Phys. Lett.*, B195:216–222, 1987.

[24] Konstantinos Anagnostopoulos. *Computational Physics, Vol II*. Lulu.com, 2014.

[25] F. Karsch. SU(N) Gauge Theory Couplings on Asymmetric Lattices. *Nucl.Phys.*, B205:285–300, 1982.

[26] Mark Alford. Cool quarks. *Physics*, 3, May 2010.

[27] Simon Hands. The Phase diagram of QCD. *Contemp.Phys.*, 42:209–225, 2001.

[28] C.R. Allton, S. Ejiri, S.J. Hands, O. Kaczmarek, F. Karsch, et al. QCD at nonzero chemical potential and temperature from the lattice. 2002.

[29] John B. Kogut and Mikhail A. Stephanov. *The Phases of Quantum Chromodynamics: From Confinement to Extreme Environments (Cambridge Monographs on Particle Physics, Nuclear Physics and Cosmology)*. Cambridge University Press, 2004.

[30] M. A. Stephanov. QCD phase diagram: an overview. *PoS LAT*, 2006:024,2006, PoS LAT2006:024,2006.

[31] Leonard Susskind. Lattice Models of Quark Confinement at High Temperature. *Phys.Rev.*, D20:2610–2618, 1979.

[32] Henning Heiselberg and Morten Hjorth-Jensen. Phases of dense matter in neutron stars. *Phys.Rept.*, 328:237–327, 2000.

[33] Aleksi Kurkela, Paul Romatschke, and Aleksi Vuorinen. Cold Quark Matter. *Phys.Rev.D*, 81:105021,2010, December 2009.

[34] J. R. Oppenheimer and G. M. Volkoff. On massive neutron cores. *Phys. Rev.*, 55(4):374–381, feb 1939.

[35] N. Chamel, P. Haensel, J. L. Zdunik, and A. F. Fantina. On the maximum mass of neutron stars. *Int. J. Mod. Phys. E*, 22(07):1330018, jul 2013.

[36] Istvan Montvay and Gernot Münster. *Quantum Fields on a Lattice (Cambridge Monographs on Mathematical Physics)*. Cambridge University Press, 1994.

[37] P. Hasenfratz and F. Karsch. Chemical Potential on the Lattice. *Phys.Lett.*, B125:308, 1983.

[38] Philippe de Forcrand and Owe Philipsen. The QCD phase diagram for small densities from imaginary chemical potential. *Nucl.Phys.*, B642:290–306, 2002.

[39] Massimo D'Elia and Maria-Paola Lombardo. Finite density QCD via imaginary chemical potential. *Phys.Rev.*, D67:014505, 2003.

[40] Vicente Azcoiti, Giuseppe Di Carlo, Angelo Galante, and Victor Laliena. Phase diagram of QCD with four quark flavors at finite temperature and baryon density. *Nucl.Phys.*, B723:77–90, 2005.

[41] C.R. Allton, S. Ejiri, S.J. Hands, O. Kaczmarek, F. Karsch, et al. The QCD thermal phase transition in the presence of a small chemical potential. *Phys.Rev.*, D66:074507, 2002.

[42] Z. Fodor and S.D. Katz. A New method to study lattice QCD at finite temperature and chemical potential. *Phys.Lett.*, B534:87–92, 2002.

[43] Shinji Ejiri. On the existence of the critical point in finite density lattice QCD. *Phys.Rev.*, D77:014508, 2008.

[44] Zoltan Fodor, Sandor D. Katz, and Christian Schmidt. The Density of states method at non-zero chemical potential. *JHEP*, 0703:121, 2007.

[45] Shinji Ejiri. Lattice QCD at finite temperature and density. *Prog.Theor.Phys.Suppl.*, 186:510-515,2010, September 2010.

[46] Kurt Langfeld, Biagio Lucini, and Antonio Rago. The density of states in gauge theories. *Phys.Rev.Lett.*, 109:111601, April 2012.

[47] Keitaro Nagata, Shinji Motoki, Yoshiyuki Nakagawa, Atsushi Nakamura, and Takuya Saito. Towards extremely dense matter on the lattice. *PTEP*, 2012:01A103, 2012.

[48] Julia Danzer and Christof Gattringer. Properties of canonical determinants and a test of fugacity expansion for finite density lattice QCD with Wilson fermions. *Phys.Rev.*, D86:014502, 2012.

[49] Rajiv V. Gavai and Sourendu Gupta. Pressure and nonlinear susceptibilities in QCD at finite chemical potentials. *Phys.Rev.*, D68:034506, 2003.

[50] Marco Cristoforetti, Francesco Di Renzo, and Luigi Scorzato. New approach to the sign problem in quantum field theories: High density QCD on a Lefschetz thimble. *Phys.Rev.*, D86:074506, 2012.

[51] Shailesh Chandrasekharan. The Fermion bag approach to lattice field theories. *Phys.Rev.*, D82:025007, 2010.

[52] Gert Aarts and Ion-Olimpiu Stamatescu. Stochastic quantization at finite chemical potential. *JHEP*, 0809:018, 2008.

[53] Gert Aarts. Complex Langevin dynamics at finite chemical potential: Mean field analysis in the relativistic Bose gas. *JHEP*, 0905:052, 2009.

[54] Masanori Hanada, Yoshinori Matsuo, and Naoki Yamamoto. Sign problem and phase quenching in finite-density QCD: models, holography, and lattice. *Phys.Rev.*, D86:074510, 2012.

[55] Owe Philipsen. Lattice QCD at non-zero temperature and baryon density. September 2010.

[56] J. B. Kogut and D. K. Sinclair. Lattice QCD at finite temperature and density in the phase-quenched approximation. *Phys. Rev.*, D77:114503, 2008.

[57] J. B. Kogut, M. A. Stephanov, D. Toublan, J. J. M. Verbaarschot, and A. Zhitnitsky. QCD-like Theories at Finite Baryon Density. *Nucl.Phys. B*, 582:477–513, 2000.

[58] Simon Hands, Seyong Kim, and Jon-Ivar Skullerud. Deconfinement in dense 2-color QCD. *Eur.Phys.J.*, C48:193, 2006. [hep-lat/0604004].

[59] Simon Hands, Peter Sitch, and Jon-Ivar Skullerud. Hadron Spectrum in a Two-Colour Baryon-Rich Medium. *Phys.Lett.B*, 662:405,2008, October 2007.

[60] S. Hands, I. Montvay, S. Morrison, M. Oevers, L. Scorzato, and J. Skullerud. Numerical Study of Dense Adjoint Matter in Two Color QCD. *Eur.Phys.J.C*, 17:285-302,2000, Eur.Phys.J.C17:285-302,2000.

[61] Axel Maas, Lorenz von Smekal, Bjorn Wellegehausen, and Andreas Wipf. The phase diagram of a gauge theory with fermionic baryons. *Phys.Rev.*, D86:111901, 2012.

[62] Axel Maas and Bjorn H. Wellegehausen. G_2 gauge theories. *PoS*, LATTICE2012:080, 2012.

[63] J. B. Kogut, D. K. Sinclair, S. J. Hands, and S. E. Morrison. Two color QCD at nonzero quark number density. *Phys. Rev.*, D64:094505, 2001.

[64] Simon Hands, Seyong Kim, and Jon-Ivar Skullerud. A Quarkyonic Phase in Dense Two Color Matter? *Phys.Rev.*, D81:091502, 2010.

[65] Benjamin Svetitsky and Francesco Fucito. Latent Heat of the SU(3) Gauge Theory. *Phys. Lett.*, B131:165, 1983.

[66] C. DeTar and U.M. Heller. QCD Thermodynamics from the Lattice. *Eur.Phys.J.*, A41:405–437, 2009.

[67] T. Umeda, S. Ejiri, S. Aoki, T. Hatsuda, K. Kanaya, et al. Fixed Scale Approach to Equation of State in Lattice QCD. *Phys.Rev.*, D79:051501, 2009.

[68] Seamus Cotter, Pietro Giudice, Simon Hands, and Jon-Ivar Skullerud. Towards the phase diagram of dense two-color matter. *Phys.Rev.*, D87(3):034507, 2013. [arXiv:1210.4496].

[69] J. Engels, F. Karsch, and T. Scheideler. Determination of anisotropy coefficients for SU(3) gauge actions from the integral and matching methods. *Nucl.Phys.*, B564:303–324, 2000.

[70] Francesco Sannino. Aspects of the quantum chromodynamics phase diagram. In *Workshop on Quark Gluon Plasma and Relativistic Heavy Ions Frascati, Italy, January 14-18, 2002*, 2002.

[71] E. Laermann and O. Philipsen. The Status of Lattice QCD at Finite Temperature. *Ann.Rev.Nucl.Part.Sci.*, 53:163–198, 2003.

[72] Claudio Bonati, Philippe de Forcrand, Massimo D'Elia, Owe Philipsen, and Francesco Sanfilippo. Constraints on the two-flavor QCD phase diagram from imaginary chemical potential. *PoS*, LATTICE2011:189, 2011.

[73] Owe Philipsen. The QCD equation of state from the lattice. July 2012.

[74] Ludmila Levkova, Thomas Manke, and Robert Mawhinney. Two-flavor QCD thermodynamics using anisotropic lattices. *Phys.Rev.*, D73:074504, 2006. [hep-lat/0603031].

[75] Richie Morrin. *A non-perturbative study of the renormalisation of action parameters in anisotropic lattice QCD with applications to finite temperature QCD.* PhD thesis, University of Dublin, Trinity College, 2009.

[76] Richie Morrin, Mike Peardon, and Sinead M. Ryan. Tuning anisotropies for dynamical gauge configurations. *PoS*, LAT2005:236, 2006.

[77] Richie Morrin, Alan O Cais, Mike Peardon, Sinead M. Ryan, and Jon-Ivar Skullerud. Dynamical QCD simulations on anisotropic lattices. *Phys.Rev.*, D74:014505, 2006.

[78] Simon Hands, Seyong Kim, and Jon-Ivar Skullerud. Two color QCD beyond the BEC regime. *PoS*, LAT2005:149, 2006.

[79] E. Eichten, K. Gottfried, T. Kinoshita, K. D. Lane, and T. M. Yan. Charmonium: The model. *Physical Review D*, 17(11):3090–3117, jun 1978.

[80] Szabolcs Borsányi, Stephan Dürr, Zoltán Fodor, Christian Hoelbling, Sándor D. Katz, et al. High-precision scale setting in lattice QCD. *JHEP*, 1209:010, 2012. [arXiv:1203.4469].

[81] R. Sommer. A New way to set the energy scale in lattice gauge theories and its applications to the static force and alpha-s in SU(2) Yang-Mills theory. *Nucl.Phys.*, B411:839–854, 1994.

[82] Wei Liu, Ying Chen, Ming Gong, Xin Li, Chuan Liu, and Guozhan Meng. Static Quark Potential and the Renormalized Anisotropy on Tadpole Improved Anisotropic Lattices. *Mod.Phys.Lett. A*, 21:2313–2322, 2006.

[83] K. Schilling and G.S. Bali. The Static quark - anti-quark potential: A 'Classical' experiment on the connection machine CM-2. *Int.J.Mod.Phys.*, C4:1167–1177, 1993.

[84] Timothy R. Klassen. The Anisotropic Wilson gauge action. *Nucl.Phys.*, B533:557–575, 1998. [hep-lat/9803010].

[85] Mushtaq Loan, Tim Byrnes, and Chris Hamer. Renormalization of anisotropy and glueball masses on tadpole improved lattice gauge action. *Eur.Phys.J.*, C31:397–402, 2003.

[86] Nikitas Stamatopoulos. Three Dimensional Lattice Dispersion Relations for Finite Difference Methods in Scalar Field Simulations. 2012. [arXiv:1210.3368].

[87] Seamus Cotter, Pietro Giudice, Simon Hands, and Jon-Ivar Skullerud. Determination of Karsch Coefficients for 2-colour QCD. *PoS*, LATTICE2013:192, 2014.

[88] Szabolcs Borsányi, Stephan Dürr, Zoltán Fodor, Sándor D. Katz, Stefan Krieg, et al. Anisotropy tuning with the Wilson flow. 2012.

[89] Yannis Burnier, Olaf Kaczmarek, and Alexander Rothkopf. Static quark-antiquark potential in the quark-gluon plasma from lattice QCD. *Phys. Rev. Lett.*, 114(8):082001, 2015.

[90] Yannis Burnier, Olaf Kaczmarek, and Alexander Rothkopf. Static quark-antiquark potential in the quark-gluon plasma from lattice QCD. *Phys. Rev. Lett.*, 114(8):082001, 2015.

[91] Yannis Burnier and Alexander Rothkopf. A gauge invariant Debye mass and the complex heavy-quark potential. *Phys. Lett.*, B753:232–236, 2016.

[92] Tamer Boz, Seamus Cotter, Leonard Fister, Dhagash Mehta, and Jon-Ivar Skullerud. Phase transitions and gluodynamics in 2-colour matter at high density. *Eur.Phys.J.*, A49:87, 2013.

[93] Yannis Burnier and Alexander Rothkopf. Disentangling the timescales behind the non-perturbative heavy quark potential. *Phys. Rev.*, D86:051503, 2012.

[94] Yannis Burnier and Alexander Rothkopf. Bayesian Approach to Spectral Function Reconstruction for Euclidean Quantum Field Theories. *Phys. Rev. Lett.*, 111:182003, 2013.

[95] Justin Foley, Alan O Cais, Mike Peardon, and Sinead M. Ryan. A non-perturbative study of the action parameters for anisotropic-lattice quarks. *Phys.Rev.D*, 73:014514,2006, Phys.Rev.D73:014514,2006.

[96] Herbert W. Hamber and Chi Min Wu. Some Predictions for an Improved Fermion Action on the Lattice. *Phys. Lett.*, B133:351–358, 1983.

[97] Martin Luscher. Properties and uses of the Wilson flow in lattice QCD. *JHEP*, 1008:071, 2010.